Interpretation of 3D Ground Penetrating Radar data in archaeology by applying seismic attributes

Synnøve Sørvåg Slåtsveen
Master in Earth Science

Department of Earth Science
University of Bergen
November 2023

Abstract

Ground Penetrating Radar (GPR) has emerged as a widely employed geophysical method in archaeological studies, with recent advancements leading to large-scale, high-resolution surveys. The processing techniques applied to GPR data bear significant correlation to those used in seismic analysis. In recent times, there has been a growing interest among archaeologists in employing seismic attributes for GPR interpretation. Seismic attributes have long been a staple in reservoir characterization within the field of seismic exploration. This study aims to encourage archaeologists to leverage these attributes for enhanced interpretation of archaeological structures using GPR data. To achieve this, the study delves into fundamental GPR principles, the process of data acquisition and processing, and an in-depth review of each attribute utilized in this thesis. Additionally, a systematic workflow is established to extract attributes and relevant information from GPR data, aiming to improve the interpretation of archaeological structures.

Furthermore, the integration of seismic attributes with GPR data for archaeological analysis has shown promising potential. Leveraging insights from seismic methodologies, the variance-coherence based attribute displayed promising outcomes across all three archaeological structures. Additionally, other attributes and methods have shown promising results. These findings may serve as a valuable resource for future studies aiming to interpret archaeological features through GPR data, potentially enhancing the visualization and understanding of other structures investigated in this thesis.

NOTE TO READER: All the attributes generated in this study are visualized for the large survey area at Løykja in a PowerPoint (Appendix A.1). This presentation allows readers to navigate through the various attributes, facilitating the comparison of changes between them.

Acknowledgements

First and foremost I would like to thank my supervisors for all the help and encouragement the past year. Isabelle Lecomte is thanked for valuable guidance and support. Arne Anderson Stamnes for generously providing valuable data and insightful perspectives in archaeology, and Leo Zijerveld for providing input on seismic attributes and assisting with licensing matters. I want to thank contributors from Geolunch for input and feedback on my thesis.

I express my gratitude to the Department of Earth Science, University of Bergen, for providing an exceptional learning environment and for the guidance and encouragement I received from several contributors at the department. I am forever grateful for all the knowledge I have gained. I thank Adobe, Kontur (Examiner), and SLB (Petrel) for granting me academic access to their respective software packages which have been much appreciated in this thesis.

I would like to thank all my fellow students for a good time at the university, and a special thanks to the gang in former Moho for the support. You have made my university experience delightful, even during challenging times such as stressful exam periods. Last but not least, I want to thank my family who have been supporting me throughout my academic journey and always being interested in what I have been studying, and to Fredrik for keeping up with me the past 10 months.

Contents

List of Figures

List of Tables

Acronyms

BGR Background removal. 32

EM Electromagnetic. 4, 7

GLCM Grey-Level Co-occurrence Matrix. 25

GNSS Global Navigation Satellite System. 16

GPR Ground Penetrating Radar. 4, 7, 13, 14, 16, 41

GSD Generalized Spectral Decomposition. 58

ISDFT Inverse Selective Discrete Fourier Transform. 32, 33

ns nano seconds. 31

PPS Pulse-Per-Second. 16

RDP Relative Dielectric Permittivity. vi, 13

RMS Root Mean Square. 22

RT Real-Time. 16

TWT Two-Way Travel-time. 31

Chapter 1

Introduction

This chapter aims to provide a brief overview of the motivations behind this study, outlining its objectives and aims. Additionally, it will present an outline of the thesis, offering a concise description of each chapter included in this thesis.

1.1 Motivation

Ground Penetrating Radar (GPR) is a geophysical method for mapping shallow subsurface features due to change in electromagnetic (EM) properties of materials (Davis and ANNAN, 1989). The method is widely used in archaeology due to its non-invasive and high-resolution nature (Annan, 2003; Conyers, 2007; Trinks et al., 2010; Forte et al., 2012), and over the past years, development within acquisition and processing has enhanced. Particularly concerning 3D GPR data, this acquisition method has gained popularity for conducting large-scale surveys, notably within Norwegian archaeology (Gustavsen et al., 2020). The data utilized in this study was collected using this method covering a field located at Løykja in Sunndal. This extensive dataset encompasses remnants such as post holes from longhouses, cooking pits, and burial mounds (Fredriksen and Stamnes, 2019).

However, with advance in GPR hardware and software, the development within data interpretation and feature recognition has not come as far, with the most used attribute being envelope (Trinks et al., 2018; Manataki et al., 2021). This leads to implementing attributes developed for seismic data analysis which may lead to better visualisation of archaeological structures, and can further become a standard within GPR data in archaeological prospective. By visualising archaeological structures in the best possible manner,

could potentially pave way for excavation and perhaps result in significant findings. Over the decades, seismic attributes have continued to develop, and new ones have been introduced, resulting in a vast landscape of seismic attributes. They are defined as quantitative measures derived from seismic data, and these attributes serve as an enhanced method for seismic interpretation and find widespread use in the field of seismic exploration (Chopra and Marfurt, 2005).

1.2 Aims and Objective

The aims of this thesis is to enhance the interpretation of archaeological structures commonly found at cultural sites in Norway by employing seismic attributes, allowing to improve imaging and facilitate interpretation. To achieve this, the study is structured around the following objectives:

1. Explore attributes commonly used in seismic data analysis and evaluate if these can be applied for GPR data analysis in archaeological prospective.
2. Analyse the effect of blending various attributes and spectral decomposition on archaeological structures to assess their potential for enhancing interpretation.
3. Testing machine learning to detecting structures, such as cooking pits.

1.3 Approach

The processed time-migrated data was used for extracting attributes in this study. The selection of attributes was influenced by prior knowledge in seismic interpretation, supplemented by literature on geological interpretation and reservoir characterization. The studied archaeological structures in this thesis had previously been interpreted prior to this study. Given the large-scale survey, the primary archaeological structures such as post holes, cooking pits, and burial mounds were extracted from the extensive area and studied up-close. Due to the different geological settings, the focus was primarily on homogeneous soil within the survey area, as it presented clear responses from the archaeological structures. This setting allowed for a more evident study of the main objectives. Overall, a total of 15 volume attributes were generated for each of the three archaeological structures, resulting in varied outcomes. In addition to this, a horizon was interpreted to cover the area where the post holes were located, allowing for the generation of four

surface attributes.

1.4 Thesis structure

Chapter 1: offers an introduction to the thesis topic, presenting its aims and objectives.

Chapter 2: introduces basic concepts of GPR principles, encompassing electromagnetic wave theory, properties, GPR acquisition, and processing.

Chapter 3: introduces essential knowledge of seismic attributes and their application in seismic data analysis.

Chapter 4: details the data and methodology employed in this study, encompassing the data acquisition, processing methodologies utilized, and the approach for extracting various attributes.

Chapter 5: presents the findings obtained in this study, showcasing images of the attributes generated in this thesis.

Chapter 6: provides a discussion on the outcomes and implications of the results obtained.

Chapter 7: concludes the main findings derived from this study and suggests further approaches for research and exploration.

Chapter 2

Theoretical background

This chapter, offer some background information of the archaeological history in Norway, and insight to the archaeological structures studied is provided. Additionally, I will also provide an insight into Electromagnetic (EM) wave theory, complemented by an overview of the fundamental principles of Ground Penetrating Radar (GPR). Finally, this chapter will explore seismic attributes and their established applications within the field of seismic exploration.

2.1 Archaeological targets

Norwegian archaeology encompasses a diverse range of periods and cultural contexts, providing valuable insights into the country's rich past. From the Stone Age to the Viking Age and beyond, archaeological investigations have yielded fascinating discoveries. Viking Age archaeology has revealed impressive ship burials like those at Oseberg and Gokstad. While attention-grabbing discoveries often dominate the headlines, Norwegian archaeology uncovers a multitude of more commonplace finds that provide significant insights. Among these are remnants of cooking pits, burial mounds, and post holes from earlier long houses. These less sensational but equally important discoveries contribute to our understanding of daily life, social practices, and architectural traditions throughout Norway's history.

During excavations, the primary targets are often not the smaller features mentioned earlier. In such cases, the use of Ground Penetrating Radar (GPR) becomes invaluable as it allows for the detection of these specific targets without the need for extensive

excavation. By employing GPR, archaeologists can efficiently identify and investigate these features, saving time and resources while still gaining valuable insights.

Post holes

Within archaeological datasets, the presence of post holes often signifies the existence of prehistoric longhouses dating back to the Iron Age. These post holes may contain either stones, used for reinforcing the posts, or alternative materials distinct from the surrounding soil. As explained by Stamnes (2016) in his research, the dimensions of a post hole typically range from 0.2 to 0.5 meters in diameter. As shown in figure 2.1 longhouses are built of timber logs with surrounding walls. This illustration shows how the post holes are arranged, and how the thickness of the timber logs vary.

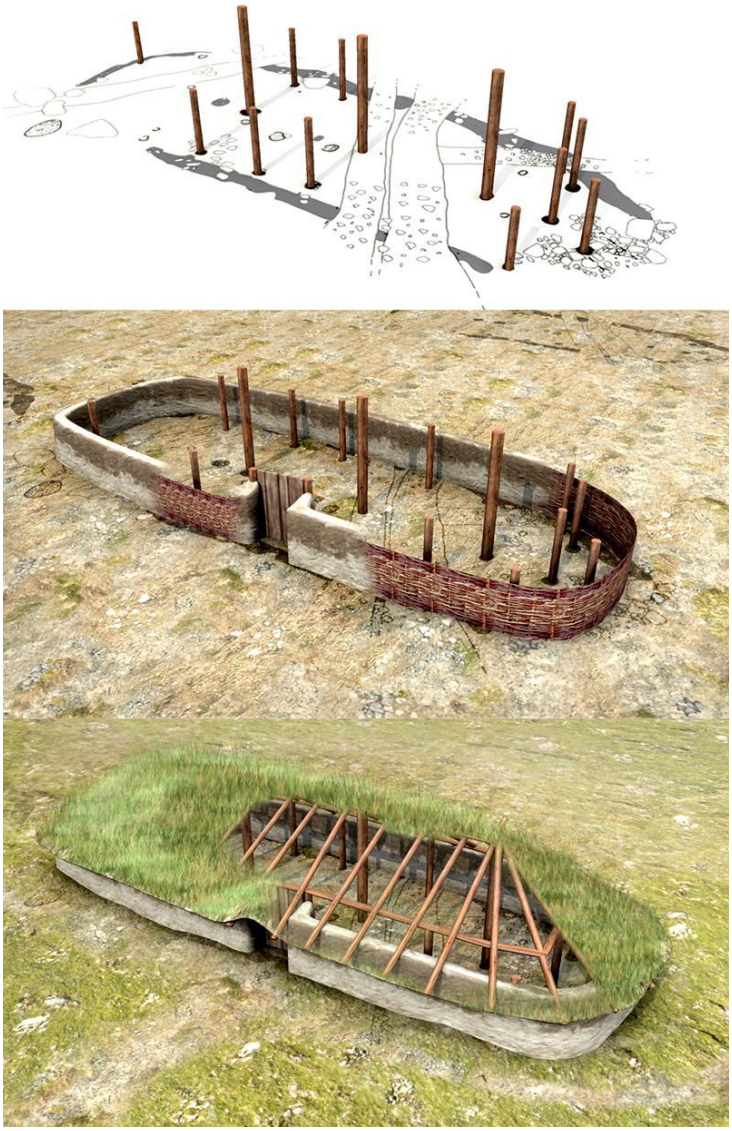

Figure 2.1: *Visualization of how the posts' are arranged to stabilize further construction, and the final result of a longhouse. Modified from (Myhre, 2002)*

Cooking pit

Within the purview of archaeology, cooking pits stand as compelling markers of civilization, intrinsically intertwined with the culinary arts. These artefacts constitute commonplace discoveries within Norwegian archaeological sites, often marginalized by investigators due to their seemingly unremarkable attributes. However, in regions where clusters of cooking pits have been unearthed, it is frequently postulated that these sites served as venues for significant communal gatherings, imbued with a sense of occasion and human congregation (Gustavsen et al., 2018; Fredriksen and Stamnes, 2019). Employing the methodology of radiocarbon dating, cooking pits discovered in Norway predominantly derive from the early Iron Age, spanning the temporal ambit between 500 BCE and 550 CE (Gustavsen et al., 2018). Distinguished by their circular to round-like structures, these culinary recesses feature ample stone fillings, shown in figure 2.2. These stones were subjected to heat, functioning as rudimentary stoves. The detection of organic remnants and charcoal deposits emerges as a pivotal criterion for ascertaining the culinary purpose of a given pit.

Figure 2.2: *Photo of a well-preserved a cooking pit in Østfold county. The photo to the left showing the cooking pit before excavation, and the photo to the right showing a cross section. Modified from (Gustavsen et al., 2018)*

Burial mound

Burial mounds represent a common discovery in Norwegian archaeological sites. These mounds, meticulously constructed from a mixture of clay, sand and stone, serve as repositories for one or multiple graves. They exhibit various morphological configurations, with circular or round-like shapes being the most frequently encountered. The practice of constructing burial monuments, which includes mounds, has in Norway its origins dating

back to the Young Stone Age (Engevik, 2018). However, most of the burial mounds found in Norway date to the Iron Age and can reach impressive dimensions, with some having a diameter of up to 177 meters (Engevik, 2018). The Figure 2.3 is taken from the study regarding the Gjellestad ship located outside of Oslo (Høgskolen i Østfold, 2020). This ship was hidden in a burial mound, and there were also located several burial mounds as shown in the figure. In this figure the burial mounds are visible above the ground, but throughout time, these mounds can be submerged.

Figure 2.3: *Illustration of the Gjellestad ship, where the white arrows are burial mounds surrounding the buried ship. Modified from (Høgskolen i Østfold, 2020)*

2.2 Ground Penetrating Radar - basic principles

Electromagnetic waves encompass a vast spectrum of frequencies, ranging from radio waves with extended wavelengths to high-energy gamma rays with incredibly short wavelengths. Within the domain of GPR systems, transmitted waves typically operate within the radio frequency segment of the electromagnetic spectrum. These EM waves are characterized as non-mechanical transverse waves and propagate at the speed of light when in vacuum. However, the velocity of EM waves are influenced by the permittivity and permeability of the medium they travel though. In a medium, the wave velocity is typically

lower than in free space, as illustrated in Table 2.1 (Weinstein, 1988).

2.2.1 Maxwell's equations

To understand the propagation characteristics of an EM wave, Maxwell's equations play a pivotal role. These equations, when combined with the constitutive relationship (Jol, 2008), mathematically describe the behavior of EM waves as they propagate through different media.

Maxwell's equations establish a fundamental connection between the velocity and attenuation of electromagnetic waves. Specifically, the velocity of an EM wave is intricately linked to the electromagnetic properties of the medium through which it propagates (Guéguen and Palciauskas, 1994).

$$\nabla \times \vec{E} = -\frac{\partial \vec{B}}{\partial t} \tag{2.1}$$

$$\nabla \times \vec{H} = \vec{J_T} + \frac{\partial \vec{D}}{\partial t} \tag{2.2}$$

$$\nabla \cdot \vec{D} = q \tag{2.3}$$

$$\nabla \cdot \vec{B} = 0 \tag{2.4}$$

Equation 2.1, known as Faraday's law, describes how a changing magnetic field induces an electric field. In this equation, the sum of electric field forces is equal to the negative rate of change of magnetic flux density over time (Jol, 2008). Ampère's law (Equation 2.2) states that a magnetic field can be generated by electric current or by changing electric fields (Guéguen and Palciauskas, 1994). The last term in this equation, the displacement current, was introduced by Maxwell and accounts for changing electric fields. This term is essential for explaining electromagnetic wave propagation. Equation 2.3 represents Gauss's law for electricity, indicating that electric charge generates an electric field. Gauss's law of magnetism (Equation 2.4) asserts that isolated magnetic monopoles do not exist (Annan, 2003).

2.2.2 Wave properties

Permittivity and electrical conductivity are fundamental properties that significantly impact the behavior of EM waves. These properties play a critical role in various aspects

of wave propagation, including attenuation, velocity, and impedance. When studying the propagation of EM waves, it is essential to consider how permittivity, electrical conductivity, and frequency collectively influence wave characteristics.

The wave equation of a plane wave in the time domain is given by

$$\nabla^2 E = \sigma\mu_0 \frac{\partial E}{\partial t} + \epsilon\mu_0 \frac{\partial^2 E}{\partial t^2} \tag{2.5}$$

The first term accounts for diffusion behavior, while the latter term represents propagation behavior. This propagation equation is derived from Maxwell's equations by taking the curl of Faraday's law and combining it with Ampère's law Guéguen and Palciauskas (1994). With the assumption of plane wave solution, the wave equation in the frequency domain is given by

$$\nabla^2 E = i\omega\sigma\mu_0 E - \omega^2\epsilon\mu_0 E \tag{2.6}$$

In a high frequency regime, such as for GPR, we can assume that ω approaches infinity. We are now left with the equation of propagation (in time domain)

$$\nabla^2 E = \epsilon\mu_0 \frac{\partial^2 E}{\partial t^2} \tag{2.7}$$

Furthermore, expressing the electromagnetic wave velocity as $\frac{1}{\sqrt{\epsilon\mu_0}}$, we can formulate the propagation equation as follows:

$$\nabla^2 E = \frac{1}{v^2} \frac{\partial^2 E}{\partial t^2} \tag{2.8}$$

In the high frequency regime, the velocity and attenuation become frequency-independent, which is also known as the GPR plateau. For a simple homogeneous media, all frequency components travel with the same velocity and suffers the same attenuation, as shown in Figure 2.4 (Jol, 2008).

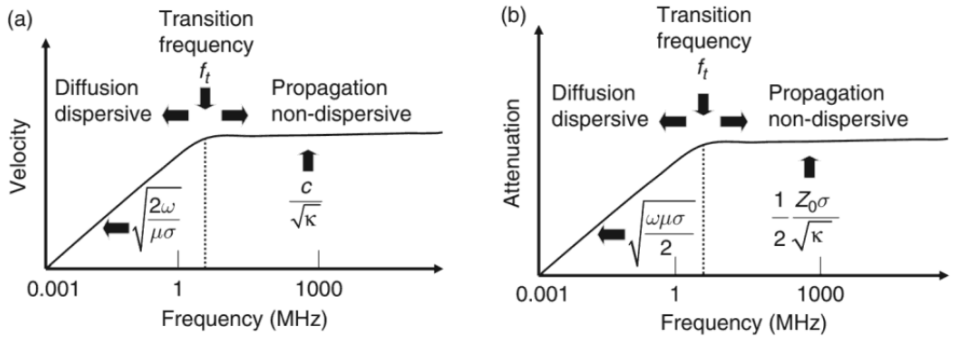

Figure 2.4: *Variation in velocity and attenuation at different frequency regimes. For a simple homogeneous media, when the frequency increases from the transition frequency the velocity and attenuation will be constant. Modified from (Jol, 2008)*

2.2.3 GPR principles

Ground Penetrating Radar is a well-established geophysical technique known for its non-invasive nature. Operating at high frequencies with high resolution, it finds application in diverse fields like geological studies, geotechnical engineering, sedimentology, and glaciology. In the realm of archaeology, GPR is extensively employed to map concealed artifacts and structures (Zhao et al., 2013). Given the high-frequency nature of this method, the waves have limited penetration and primarily travel within the shallow subsurface, reaching depths of a few meters, depending on the frequency band employed.

The essence of GPR lies in generating reflection data. Electromagnetic (EM) waves travel through the subsurface, and we record the two-way travel time for each reflection as these waves propagate. These EM waves are influenced by three core physical properties: relative permittivity, electrical conductivity, and magnetic permeability (Schneidhofer et al., 2022). These properties vary with subsurface materials, resulting in wave reflections. In GPR applications, variations in relative permittivity and electrical conductivity are of primary importance, while magnetic permeability is often disregarded (Jol, 2008). Nonetheless, a comprehensive understanding of these physical properties is essential for effectively interpreting GPR data.

In the context of GPR data interpretation, understanding wave properties is crucial. Key wave field attributes include velocity (v), attenuation (α), and electromagnetic impedance (Z) (Jol, 2008). In free space, EM waves travel at the speed of light (approximately $3 \cdot 10^8\ m/s$), with the frequency and wavelength being inverse proportional to each other. As EM waves pass through different media, their velocity changes due to variations in

physical properties. The EM wave velocity is a relation between the speed of light and the relative permittivity, as shown in Equation 2.9. The relative permittivity of a material is given as the relation between the permittivity of the material and the permittivity of vacuum.

$$v = \frac{c}{\sqrt{\epsilon}} \tag{2.9}$$

The relative permittivity ranges between 1 to 80, where water exhibits the highest value and air at the opposite end of the scale. As shown in Table 2.1 higher permittivity corresponds to lower velocity, increased conductivity, and amplified attenuation. The degree of water saturation within soil materials significantly influences the nature of the reflected signal. As demonstrated in Table 2.1, materials like clays, silt, and sand exhibit a notable range in permittivity, attributed to their varying water saturation levels. Among these, clays and silt, along with sea water, exert the most pronounced influence on reflected signals and penetration depth (Jol, 2008; Schneidhofer et al., 2022).

Permittivity measures a material's capacity to store electrical energy. In media characterized by high permittivity (ϵ_r), the stored energy content is substantial, leading to a correspondingly lower velocity of the EM signal. Conversely, when the permittivity is low, the stored energy is diminished, resulting in a higher signal velocity. Electrical conductivity (σ) governs the achievable penetration depth of EM waves; in other words, it measures a material's ability to conduct an electrical current (Schneidhofer et al., 2022). Materials with lower conductivity facilitate greater penetration depths compared to those with higher conductivity. This phenomenon arises from the interplay of electrical loss and wave attenuation (Jol, 2008). Magnetic permeability measures a material's capacity to create a magnetic field when an external field is present. This property is usually thought to have minimal impact on the propagation of EM waves, and as a result, it is often disregarded in the context of GPR (Conyers, 2007).

Table 2.1: *Different media with respectively electromagnetic properties. Modified from (Davis and ANNAN, 1989)*

Material	ϵ_r	σ **(mS/m)**	V **(m/ns)**	α **(dB/m)**
Air	1	0	0.3	0
Distilled water	80	0.01	0.033	2×10^{-3}
Fresh water	80	0.5	0.033	0.1
Sea water	80	3×10^4	0.01	10^3
Dry sand	3-5	0.01	0.15	0.01
Saturated sand	20-30	0.1-1.0	0.06	0.03-0.3
Limestone	4-8	0.5-2	0.12	0.4-1
Shales	5-15	1-100	0.09	1-100
Silt	5-30	1-100	0.07	1-100
Clays	5-40	2-1000	0.06	1-300
Granite	4-6	0.01-1	0.13	0.01-1
Dry salt	5-6	0.01	0.13	0.01-1
Ice	3-4	0.01	0.16	0.01

The three EM properties mentioned earlier serve as the basis for the reflections detected through GPR. Alterations in these properties between neighboring materials give rise to reflections and refractions of EM waves. The more significant the contrast is between two materials at an interface, the higher the amplitude of the reflected waves become. This, in turn, will produce a strong reflected signal (Conyers, 2007).

$$R = \frac{\sqrt{\epsilon_1} - \sqrt{\epsilon_2}}{\sqrt{\epsilon_1} + \sqrt{\epsilon_2}} = \frac{v_2 - v_1}{v_2 + v_1} \tag{2.10}$$

Contrasts in electromagnetic properties between adjacent materials in the subsurface impacts the reflected energy, as shown in Equation 2.10. The greater the contrast in electromagnetic properties between to materials at an interface the greater is the amplitude of the reflected waves, which in turn will produce a strong reflected signal (Conyers, 2007). Figure 2.5 show how a GPR signal is impacted by the water saturation in the two materials.

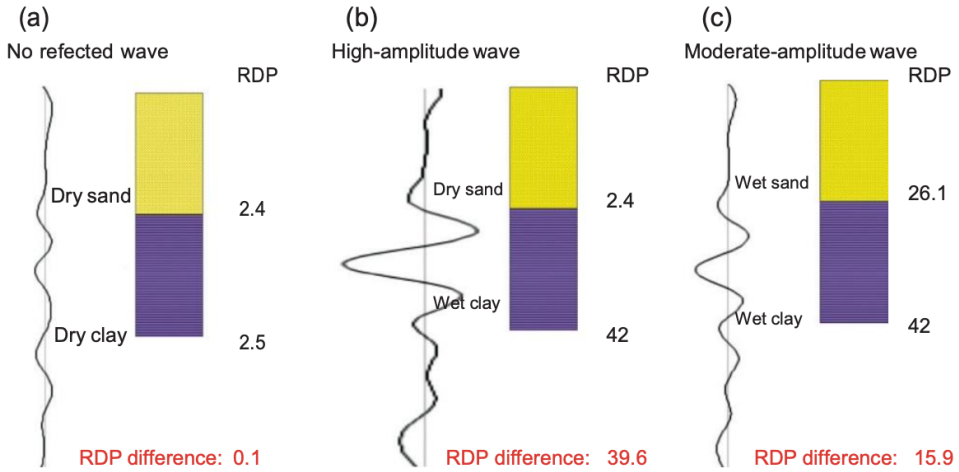

Figure 2.5: *Reflection models showing the impact of water saturation and different material properties. Where Relative Dielectric Permittivity (RDP) is noted as relative permittivity in this thesis. Modified from (Conyers, 2016)*

2.2.4 Environmental impact

In a GPR survey, several factors must be carefully considered, including the selection of the appropriate equipment and survey design. While these factors are crucial for obtaining high-quality data, there is another factor that often receives insufficient attention - environmental conditions such as precipitation rates and soil moisture (Schneidhofer et al., 2022). Notably, GPR research tends to overlook this factor, with only a limited number of studies addressing it (Boddice, 2015; Gabler et al., 2019). The absence of studies addressing the environmental impact prompted the initiation of the Borre Monitoring Project led by Schneidhofer et al. (2022). This project aims to investigate the environmental impact and its effects on the quality of GPR data.

The study encompassed 12 GPR surveys conducted from July 2016 to September 2017. The findings revealed that the highest data quality was achieved during dry conditions in the winter months, particularly with a frozen topsoil, while the datasets with the lowest quality were collected under wet conditions. Studies of this nature contribute to the optimization of GPR survey planning and, most importantly, enhance the likelihood of obtaining high-quality data (Schneidhofer et al., 2022).

2.2.5 Resolution

When dealing with GPR data or any other geophysical data, the question of system resolution consistently emerges. Resolution serves as a measurement of how precisely an object's position in the subsurface can be determined. The capability to discern features within the subsurface relies on resolution in both the lateral and vertical dimensions. Lateral resolution dictates the minimum distance that must exist between two adjacent reflectors at the same depth for the GPR to identify them as distinct occurrences (Rial et al., 2009). The concept of the Fresnel zone is frequently linked to lateral resolution, and any features smaller than the Fresnel zone will not register as separate events.

The resolution is a relation between velocity, frequency and wavelength, where the wavelength is given by

$$\lambda = \frac{v}{f} \tag{2.11}$$

When it comes to vertical resolution, the tuning thickness holds significance. As a rule of thumb, it is often considered to be one-quarter of the wavelength ($\lambda/4$) as suggested by (Widess, 1973). However, for GPR data, a more realistic estimate for vertical resolution is typically half of the wavelength ($\lambda/2$) as proposed by (Rial et al., 2009). Since GPR system uses high-frequency antennas, often the GPR data will have high resolution, which in turn allows us to detect small objects, but at the cost of penetration depth. The vertical and horizontal resolution is dependent of several factors. To obtain maximum resolution, there has to be high frequency and low velocity.

The method described above is a widely accepted standard in both GPR and seismic applications, and as demonstrated, it is contingent on the signal frequency. As indicated by Våland (2014), resolution is intricately linked to the signal bandwidth. The concept of bandwidth implies that a greater bandwidth will inherently yield higher resolution, as further emphasized by (Simm et al., 2014). This highlights the critical role that signal characteristics, particularly bandwidth, play in determining the resolution of geophysical data in both GPR and seismic studies.

2.3 GPR acquisition

Over the past decade, GPR systems have evolved significantly, transitioning from single-channel configurations to large-area, high-resolution multi-channel systems (Gustavsen et al., 2020).

In a single-channel setup, a cart is employed to carry both the transmitter and receiver antennas, and it is either pulled or pushed across the survey area as described by Trinks et al. (2018). This system is designed to capture two-dimensional vertical profile sections at a consistent profile spacing. These profiles are then interpolated to create three-dimensional data volumes, often referred to as "2.5D data" or "pseudo" 3D data.

A multi-channel GPR system comprises multiple transmitter and receiver antennas arranged in a linear array configuration. These antennas are strategically positioned in two overlapping rows, as illustrated in Figure 2.6. In this setup, the receiver antennas capture signals emitted by the two adjacent transmitter antennas. The outcome is a multi-channel system with a well-defined swath for each traverse, where the swath's length is determined by the cross-line trace spacing (Trinks et al., 2018).

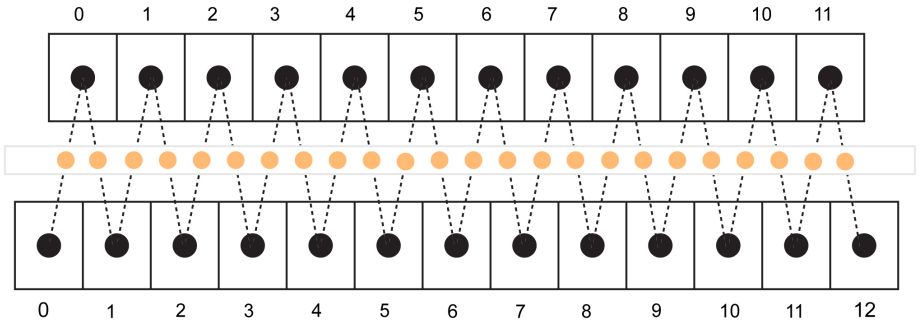

Figure 2.6: *Multi-channel antenna array, with 13 transmitters and 12 receivers. The orange dots represents the 24 channels.*

In contrast to the single-channel system, the increased size and weight of the multi-channel system require it being towed or pushed by a vehicle. This design enhancement leads to improved efficiency, as the GPR arrays enable smooth, rolling turns during data acquisition in large loops. It is also a common practice to overlap swaths to achieve complete coverage, as depicted in Figure 2.7 (Trinks et al., 2018).

Figure 2.7: *Illustration of how a GPR setup to the left, with the swath pattern to the right. Modified from (Trinks et al., 2018)*

In every GPR survey, precise data positioning is essential for accurate interpretation. For most GPR systems, both single-channel and multi-channel, an odometer is mounted on the survey cart. In single-channel surveys, the odometer is used to record the in-line distance and ensure evenly spaced intervals. However, for larger area surveys, an increase in the use of Real-Time (RT) Global Navigation Satellite System (GNSS) technology has been observed, providing more precise positioning. GNSS is typically mounted on top of the GPR antenna array and records Pulse-Per-Second (PPS) signals (Trinks et al., 2018).

Conventional GPR systems transmit pulses into the subsurface at a fixed center frequency. However, in the past two decades, there has been a growing development and utilization of step-frequency GPR. This system operates in the frequency domain and consists of a series of sine waves with progressively increasing frequencies.

The transmitted signal covers a specific frequency range with a defined frequency step, which can be visualized as a staircase function in a frequency-versus-time plot, shown in Figure 2.8. The width of the frequency step determines the trace resolution, as highlighted in a study by Leckebusch (2011); Eide et al. (2019).

The "dwell time" represents the duration that the system spends on a single frequency,

as discussed by Eide et al. (2019). Users have control over parameters such as dwell time, sampling distance and time window. With a long time window, the shorter each frequency step is, which results in higher resolution, but longer acquisition time.

The received signal records both amplitude and phase information in the frequency domain, which can subsequently be converted to the time domain by applying an inverse Fourier transform.

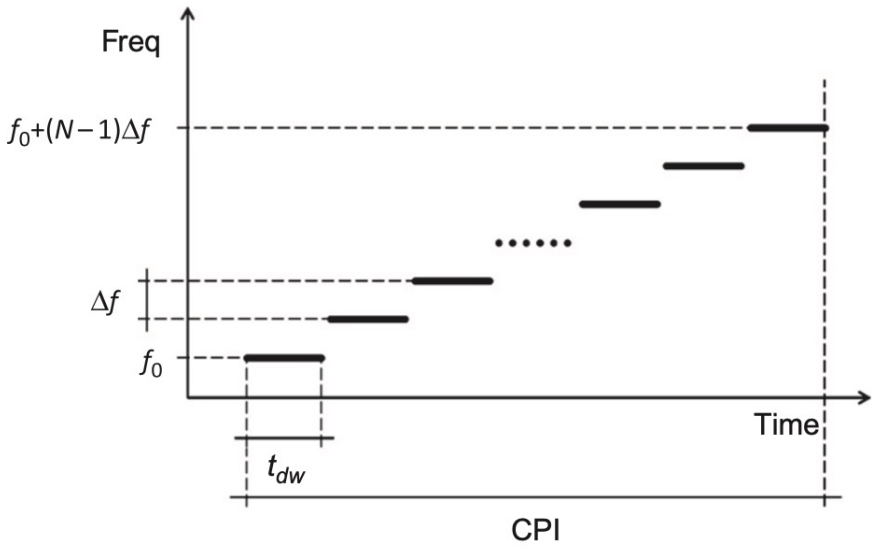

Figure 2.8: *Staircase plot as a function of frequency versus time.* t_{dw} *is the dwell time,* f_0 *is the minimum frequency,* Δf *is the frequency step, and* $f_0 + (N-1)\Delta f = f_n$ *is the frequency of* n*th sine wave. Modified from (Eide et al., 2019)*

2.3.1 Data processing

Processing GPR data is crucial for obtaining meaningful information from it. According to Jol (2008), there is a minimum of essential processing steps required to make GPR data comprehensible. These steps include de-wow filtering and time-zero correction. De-wow filtering is employed to eliminate very low frequencies, often referred to as "wow," from the data. These low frequencies can result from early arrivals or inductive effects and can cause the signal to deviate from the mean zero level.

Even though GPR transmitters are typically well-coupled to the ground, there is still an air gap between the transmitter and the solid ground. The signal from this air gap is the first to be received and needs correction. Adjusting the time-zero point, where the first strong reflection is observed, can significantly improve the depth imaging of subsurface structures (Jol, 2008). Additionally, other processing techniques that enhance imaging

include various filtering methods, such as frequency filters and background removal, gain functions, and migration.

Migration is a fundamental processing method essential for enhancing the interpretation of GPR data. The primary objective of this method is to mitigate diffractions and accurately position energy within the subsurface. The ultimate goal of migration is to optimize the imaging of geological and archaeological features (Neal, 2004). While migration was originally developed for seismic data processing, it has been established that it can be applied to a wide range of GPR datasets (Fisher et al., 1992).

Chapter 3

Seismic attributes

Seismic attributes were initially developed in the early 1970s when color printers were introduced, allowing for the display of colored reflection strength, a breakthrough for the purpose of 'bright spot' identification (Chopra and Marfurt, 2005). Initially, attributes encompassed instantaneous amplitude, phase, and frequency. However, since then, seismic attribute technology has evolved significantly, giving rise to surface-based and volume attributes (Zhao et al., 2013). Chopra and Marfurt (2007) defines seismic attributes as specific quantities derived from geometric, kinematic, dynamic, or statistical features extracted from the seismic data. Seismic attribute analysis has proven to be a powerful tool for interpreters as it visualizes features and patterns that may not be readily apparent in the original data (Zhao et al., 2013).

The current landscape of seismic attributes is extensive, presenting a challenge in selecting the most suitable attributes for a given dataset. In the past decade, researchers have made significant efforts to categorize seismic attributes, resulting in various classification schemes. A recent study by Dewett et al. (2021) reviews ten seismic attribute classifications proposed by different scientists and presents useful seismic attribute taxonomies. The authors have organized seismic attribute taxonomies into seven distinct conceptual domains, encompassing signal properties, mathematical formulations, interpretive value, and four combinations of these three. Each of these conceptual domains is depicted in four taxonomy charts. An example of one of the charts is illustrated in Appendix D.1. Furthermore, the study also provides a list of 37 seismic attributes, along with concise descriptions and references for each attribute (Dewett et al., 2021).

3.1 Seismic attributes and their use in seismic exploration

Attributes play a crucial role in seismic exploration and data analysis. Among the various attributes available, some are more commonly used than others in seismic exploration. For example, RMS amplitude and coherence are widely employed in this field, as noted by Chopra and Marfurt (2008). These, together with other attributes often used for reservoir characterization in seismic exploration, are described below (Dewett et al., 2021; Pigott et al., 2013).

3.1.1 Coherence

Coherence is a measure of the similarity between different traces in the data, and there are various algorithms for calculating coherence, with the most common ones being semblance, cross-correlation, and variance. Other coherence algorithms are, eigenstructure-based coherence, gradient structure tensor-based coherence and least-squares-based coherence (Chopra and Marfurt, 2007). When using the semblance method to calculate coherence, the first step is to estimate dip and azimuth. After that, one can compute the semblance between the target trace and its nearest neighbors (Chopra and Marfurt, 2007). The semblance, denoted as $c_s(t,p,q)$, is calculated using Equation 3.1:

$$c_s(t,p,q) = \frac{\sum_{k=-K}^{K}\left[\frac{1}{J}\sum_{j=1}^{J} u_j(t+k\Delta t - px_j - qy_j)\right]^2}{\sum_{k=-K}^{K}\frac{1}{J}\sum_{j=1}^{J}\left[u_j(t+k\Delta t - px_j - qy_j)\right]^2} \tag{3.1}$$

$c_s(t,p,q)$ is the Semblance with respect to time t, and apparent dips p and q. j is an index representing the jth trace within the analysis window. u_j denotes the signal from the jth trace. x_j and y_j correspond to the x and y distances of the jth trace from the master trace, shown in Figure 3.1a). K is a parameter that defines the extent of the analysis window (Chopra and Marfurt, 2007).

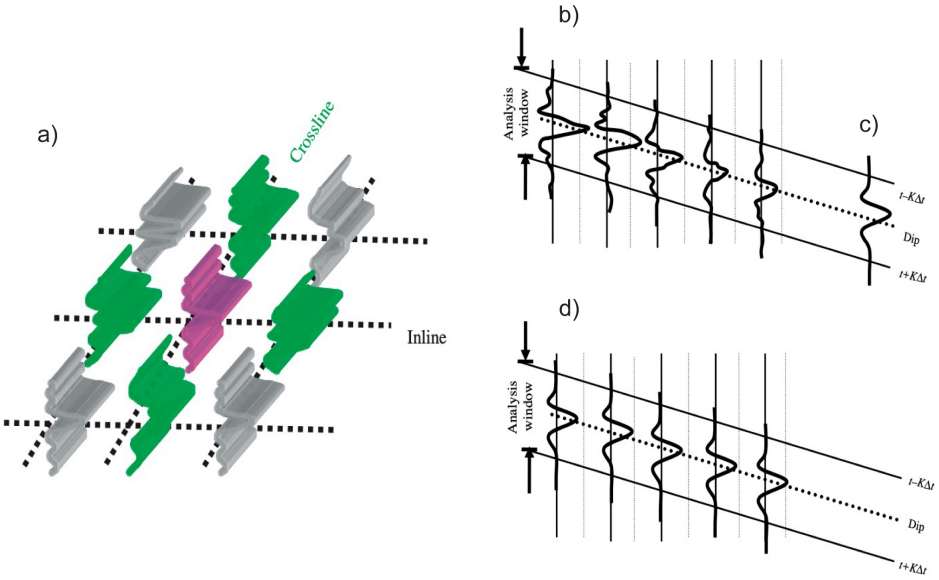

Figure 3.1: *a) The green traces correspond to the x_j and y_j traces, while the pink trace corresponds to the master trace. b) Calculate the energy of the five traces. c) Compute the average trace using the traces from part b). d) Replace each trace with the average trace. The semblance is defined as the ratio between the energy in (d) and the energy in (b). If each trace in b) is identical in waveform and amplitude, the semblance is equal to 1; otherwise, it will be less than 1. Modified from (Chopra and Marfurt, 2007)*

The variance attribute is closely related to semblance, and mathematically, it is identical to one minus the semblance, and the relationship is shown in Equation 3.2

$$c_v(t,p,q) = 1 - c_s(t,p,q) \tag{3.2}$$

According to Pigott et al. (2013), the variance attribute is sharper and more computationally efficient, and in the field of seismic data analysis, the variance attribute holds significant popularity for visualizing subsurface features, particularly faults. The effectiveness of the variance attribute in enhancing fault imaging is demonstrated in Figure 3.2, which is drawn from a fault study conducted by (Aqrawi and Boe, 2011). When compared to the original data, the variance attribute significantly improves the visibility of fault zones and other abrupt changes in amplitude, such as channel edges.

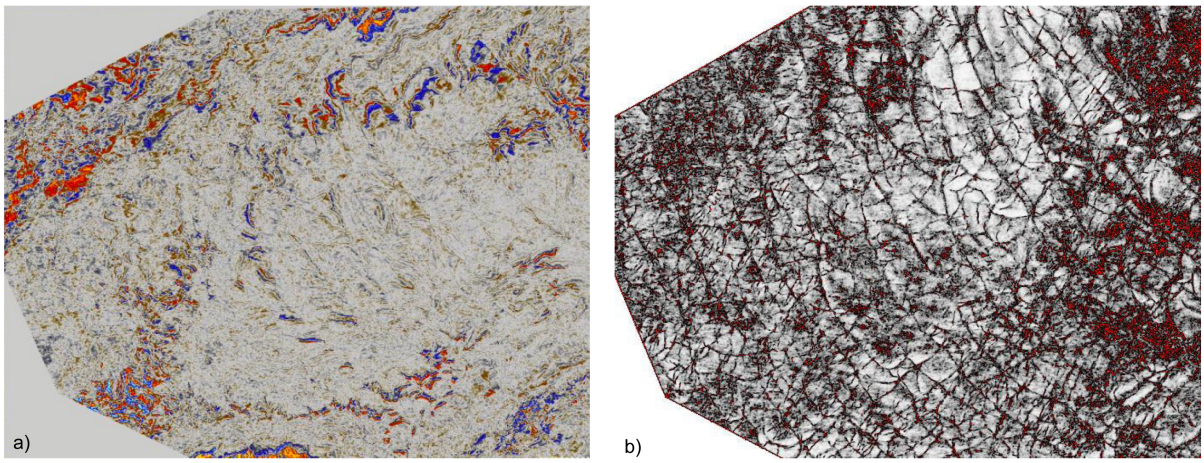

Figure 3.2: *a) Time slice of the original seismic. b) Time slice with Variance attribute. Modified from (Aqrawi and Boe, 2011)*

3.1.2 Root Mean Square amplitude

The Root Mean Square (RMS) amplitude attribute is computed by squaring each amplitude of a trace over a vertical time-window, whether it is a peak or a trough, and then calculating the average of these squared values. Finally, the square root of this average is taken, as shown in Equation 3.3. Because this method considers both positive and negative values, it effectively represents the reflection strength of the signal (Chopra and Marfurt, 2008).

$$A_{rms} = \sqrt{\frac{1}{n}\sum_{i=1}^{n} x(t_i)^2} \tag{3.3}$$

n represents the number of samples within a time window, and x(t) represents the amplitude of a trace at time t.

A study conducted by (Hossain, 2020) focusing on fluvial geomorphology and using seismic attributes is a relevant example of RMS amplitude attribute application. In their research, they employed the RMS amplitude attribute to detect sand and shale within the subsurface. The results of this analysis are depicted in Figure 3.3.

To generate the RMS amplitude map, the researchers extracted data from an interpreted horizon within a time window spanning from 5 to 20 milliseconds. In the map, regions with high amplitudes (indicated in green) are associated with sand deposits, and this correlation is substantiated by well-log data from well MB-15. Conversely, areas with low amplitudes (indicated in blue) correspond to shale formations.

This application of the RMS amplitude attribute demonstrates its utility in distinguishing different subsurface lithologies, which is a valuable capability for various geological and geophysical studies.

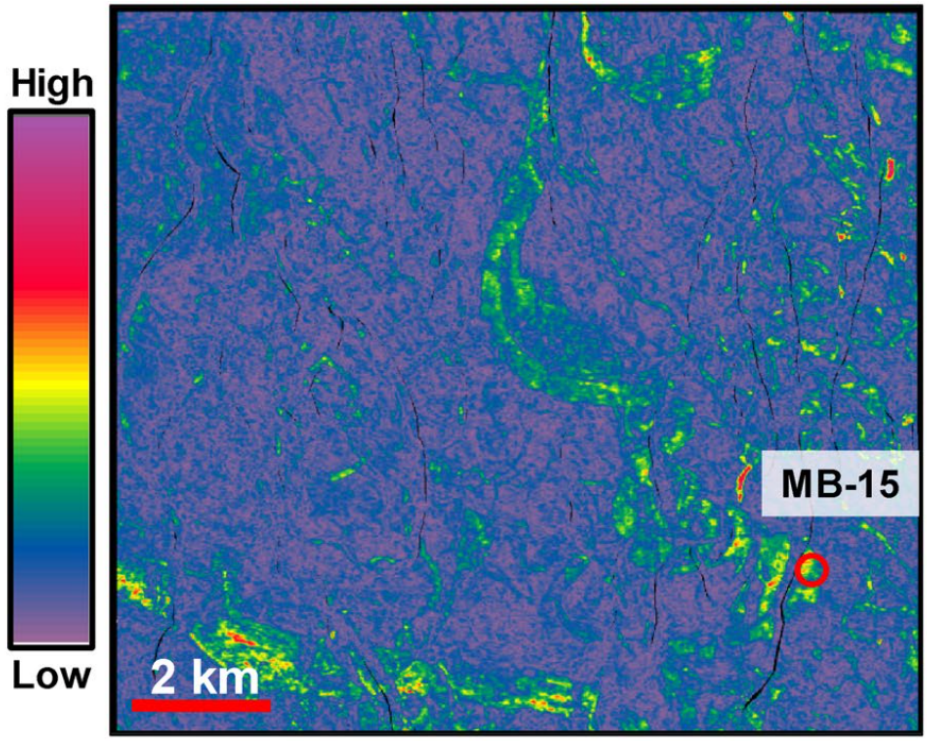

Figure 3.3: *RMS amplitude map showing high amplitude areas in green and low amplitude areas in blue. Modified from (Hossain, 2020)*

3.1.3 Dip illumination

The term "dip" in seismic data analysis refers to a vector consisting of dip magnitude and dip azimuth, as described by (Chopra and Marfurt, 2007). The dip illumination attribute is used to illuminate structures from different azimuths on time slices, and is computed by a cross correlation dip estimation. When viewing this attribute on a cross section, it may not provide much information about the structure itself (Barnes, 2003). To simplify, azimuth illuminates structures and enhances their image when the illumination is perpendicular to the structure. For example, in Figure 3.4, the fault is best illuminated with an azimuth of 0 degrees, which is perpendicular to the fault. Conversely, when the illumination is parallel, with an azimuth of 90 degrees, to the fault, the fault is not clearly visible. In seismic data analysis, dip illumination is often used for imaging features like faults and salt domes.

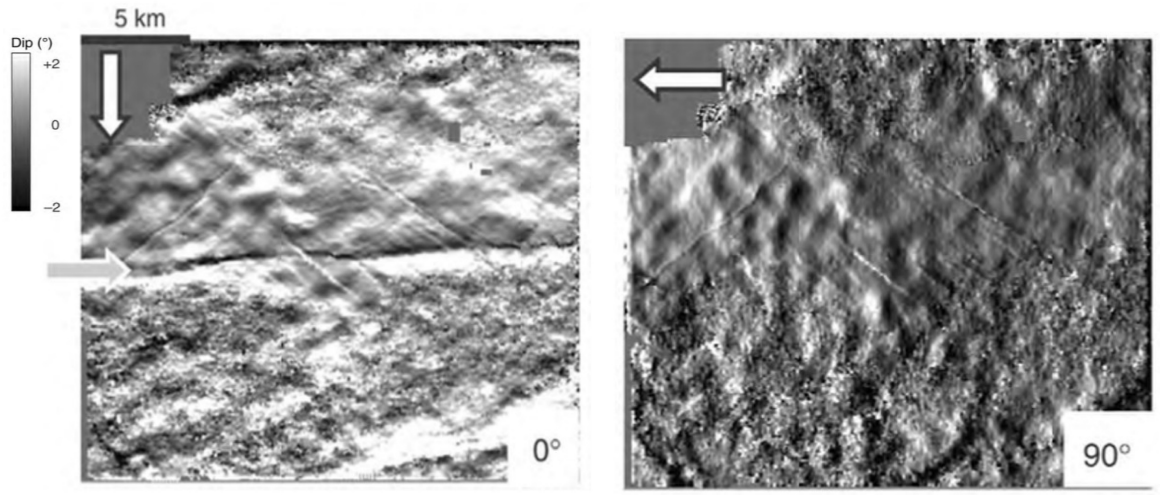

Figure 3.4: *An example from a seismic cube with dip illumination, where the light grey arrow points on the fault.The white arrows represent the illumination angle. Modified from (Chopra and Marfurt, 2007)*

3.1.4 Instantaneous attributes

Instantaneous attributes, which encompass envelope (also known as reflection strength or instantaneous amplitude), instantaneous frequency, instantaneous phase, and cosine of phase, are derived by applying the Hilbert transformation to the input seismic trace, as described by Barnes (2007).

The envelope attribute, much like RMS amplitude, represents the reflection strength of a signal. It is computed by summing the squared real components with the imaginary components, followed by taking the square root. In this context, the real part corresponds to the amplitudes of the trace, while the imaginary part is obtained through the Hilbert transform of the real part, as proposed by Chopra and Marfurt (2007). This results in only positive reflection strength and is primarily amplitude-dependent, as highlighted by Forte et al. (2012). Both the envelope and RMS amplitude attributes are extensively utilized in seismic data analysis for various purposes, including bright spot detection and lithology characterization. The envelope is mathematically computed by Equation 3.4:

$$a(t) = \sqrt{x^2(t) + y^2(t)} \tag{3.4}$$

where x(t) represents the seismic trace and y(t) is the Hilbert transformed trace, also referred to the complex trace (Barnes, 2007). Derivation of the envelope (Equation 3.4)

and Hilbert transform can be found in Barnes (2007).

Instantaneous frequency, a concept in geophysics, is defined as the time derivative of the instantaneous phase, expressed as $\frac{\Delta\phi}{\Delta t}$, as elucidated by Li and Zhao (2014). The instantaneous phase signifies the phase angle along a trace and serves to enhance the visibility of weak reflectors, as described by Li and Zhao (2014). The outcomes of these calculations are typically expressed in degrees. Therefore, a color bar representing cycles ($\phi - 180° = \phi + 180°$) is essential for accurate visualization.

Moreover, it is noteworthy that the cosine of the phase can be derived from the instantaneous phase, and, in this case, the color bar represents fixed values ranging from -1 to 1, as proposed by Li and Zhao (2014).Instantaneous frequency f_{inst} is calculated by:

$$F_{inst} = \frac{1}{360°}\frac{\Delta\phi}{\Delta t} \tag{3.5}$$

where $\Delta\phi$ is the number of cycles, and Δt is the time.

When generating the instantaneous attributes, one must define a size window. A larger window will result in a smoother result.

3.1.5 Grey-Level Co-occurrence Matrix (GLCM)

The Grey-Level Co-occurrence Matrix (GLCM) algorithm is a texture attribute often used in seismic. According to Chopra and Marfurt (2007), a texture attribute is used to analyse the spatial pattern, roughness/smoothness and variations within the seismic data. The GLCMs is defined by the number of grey levels and the spatial relationship.

The GLCMs themselves may not be optimal for direct interpretation. To enhance information extraction, it is common practice to derive additional parameters. These parameters often encompass various textural features such as contrast, energy, entropy, and homogeneity. These features serve the purpose of characterizing the texture and spatial patterns present in the data, making them valuable for image analysis and interpretation.

The contrast feature measures the local variations in intensity levels within an image. It quantifies how different adjacent pixel values are, indicating the degree of variation or texture in the image. The energy, also known as angular second moment, quantifies the orderliness or uniformity of pixel values. Higher energy values indicate more uniform and

less textured regions. The entropy is a measure of randomness or disorder in an image. High entropy values suggest greater complexity or irregularity, while low entropy values indicate more ordered or predictable patterns. The homogeneity measures the closeness of the distribution of elements in the GLCM to the GLCM diagonal. Higher homogeneity values indicate that the elements in the GLCM are closer to the diagonal, signifying smoother or more uniform textures.

3.1.6 RGB blending and spectral decomposition

RGB blending is a visualization technique which allows creating multi-attribute displays. The benefits of this technique is that it may show features more clearly and more detailed. Spectral decomposition is a common used method for RGB blending. This method separates the data into three frequency components, and where these frequency components are assigned a color (Chopra and Marfurt, 2007). Red often represents the low frequency component, green the intermediate component, and blue the high frequency component. In seismic exploration RGB blending together with spectral decomposition are used to enhance visualization of channels and faults. As shown in Figure 3.5, where spectral decomposition with RGB blending has been extracted from a seismic cube, the RGB blending highlights the channel (Othman et al., 2016). This shows that in areas where there is a strong signal for all the three frequencies, this is displayed with a whitish color. Furthermore, Chopra and Marfurt (2007) suggests a method where attributes displayed in shades of grey, such as coherence, can be combined with a color attribute, often RMS amplitude, to improve the imaging of geological structures and reservoir characterisation. This is achieved by adjusting the transparency of the color attribute, allowing for a more effective fusion of different information.

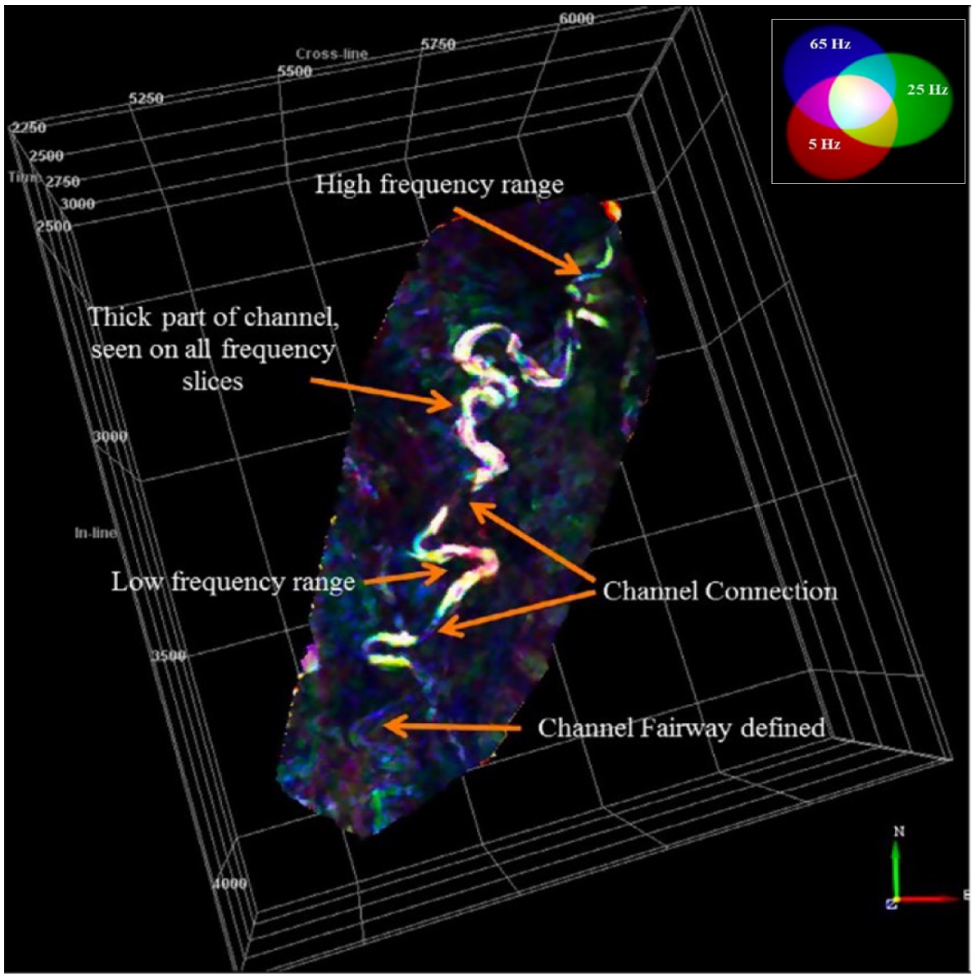

Figure 3.5: *RGB blending with spectral components of 5 Hz, 25 Hz, and 65 Hz. Modified from (Othman et al., 2016)*

3.1.7 Other seismic attributes

Table 3.1 provides an overview of several other commonly used attributes along with brief descriptions of each attribute's characteristics and applications.

Table 3.1: *Volume attributes used in this study with respective descriptions*

Attribute	**Description**
3D edge enhancement	A volume attribute filter, which is commonly used for edge detection, including faults and discontinuities.
Ant track	An algorithm that is based on ants following different paths. It is used to connect fault zones (Chopra and Marfurt, 2007).
Chaos	Illustrates the chaoticness in the data, which refers to differences in dip and azimuth. Commonly used for fault zone imaging (Pigott et al., 2013).
Dip deviation	Edge detecting method, used for fault and channel detection (Pigott et al., 2013)
Structural smoothing	Used to remove noise, enhance structural imaging, and improve the data for horizon interpretation.

In this chapter, I have introduced various seismic attributes along with their descriptions and applications in the field of seismic data analysis. These attributes will be further explored in the results section.

Chapter 4

Data and Methods

In the following chapter, I will go through the data used in this study, and describe GPR acquisition and processing methods used in this study. Furthermore, will the methods, regarding seismic attributes, be described. The chapter will be concluded with a suggested workflow.

4.1 Site description

In this study, I have analyzed data from Løykja, which was acquired by Arne Anderson Stamnes and his team in August 2018 (Fredriksen and Stamnes, 2019). Prior to the survey, significant archaeological findings were discovered in-situ by metal detecting. As reported in Fredriksen and Stamnes (2019), remarkable archaeological discoveries were made in Sunndalen near Løykja, including the largest burial ground in Møre og Romsdal and a sizable cooking pit area. The primary objective of the survey was to document these archaeological features for potential future excavation.

4.1.1 Løykja

Løykja is situated in Sunndal, Møre og Romsdal county, on the west coast of Norway. The survey area comprises cultivated land with high activity, as illustrated in Figure 4.1. Sunndal itself is characterized by a U-shaped valley, a geological feature dating back to the Ice Age in Norway. According to the Norwegian Geological Survey (NGU), the survey area consists of both glaciofluvial and fluvial deposits. The glaciofluvial deposits predominantly comprise varying grain sizes, ranging from fine-grained sand to stones and

blocks, while the fluvial deposits are primarily composed of sand and gravel (NGU, 2023). According to (NIBIO, 2023) the area consists of Cambisol soil type with silty to fine sand, with small volumes of gravel.

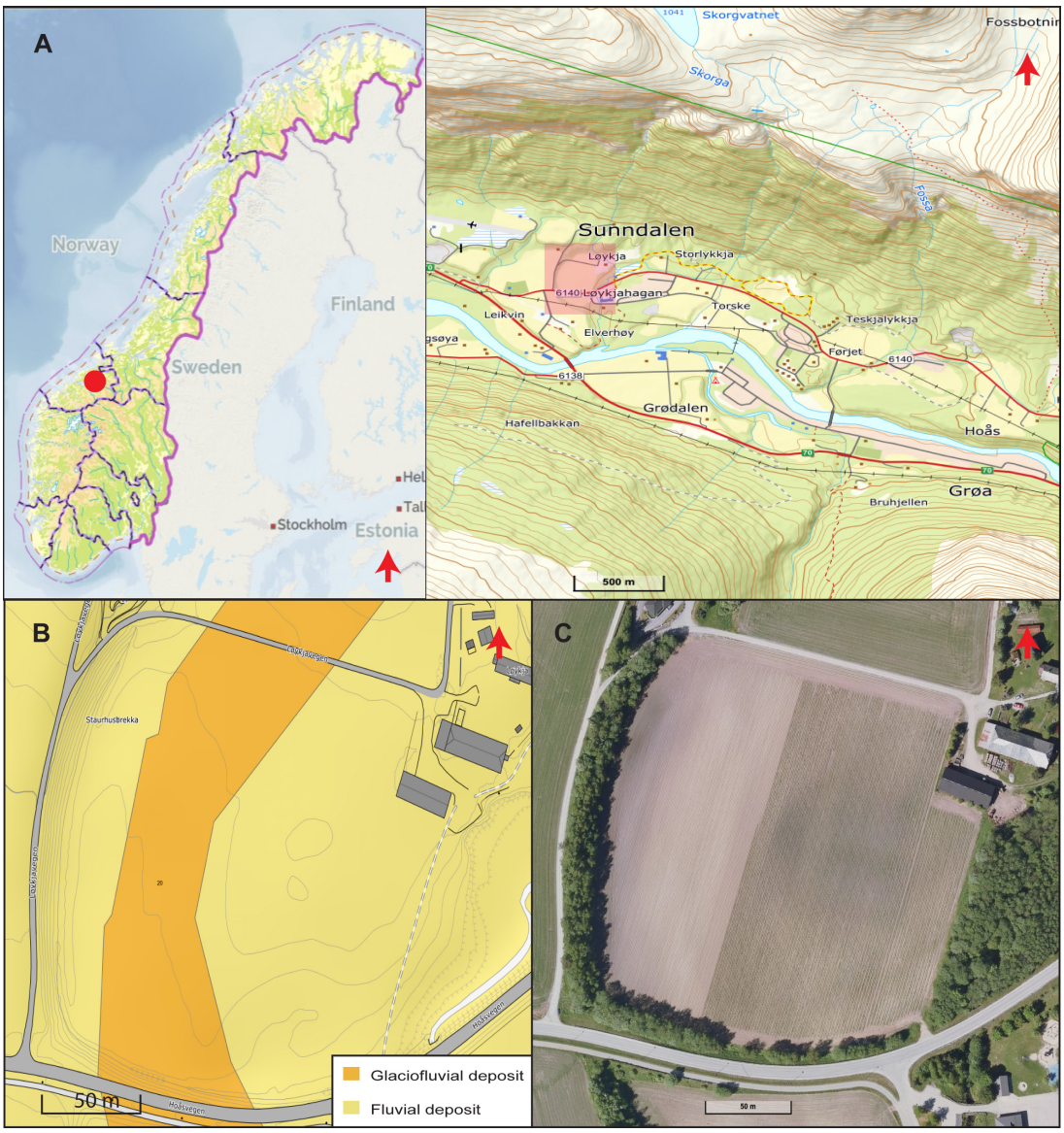

Figure 4.1: *Løykja is situated approximately 180 km south of Trondheim, within the Sunndal region. A: Løykja's location within Sunndal, marked with a red square. B: Quaternary deposition map. C: An aerial photograph showcasing the cultivated land*

4.2 Data

The archaeological structures located at Løykja, was carefully interpreted by Arne Anderson Stamnes and his team, and the interpreted results is shown in Figure 4.2. These interpretation have been a base for the further investigation to enhance imaging of the archaeological structures.

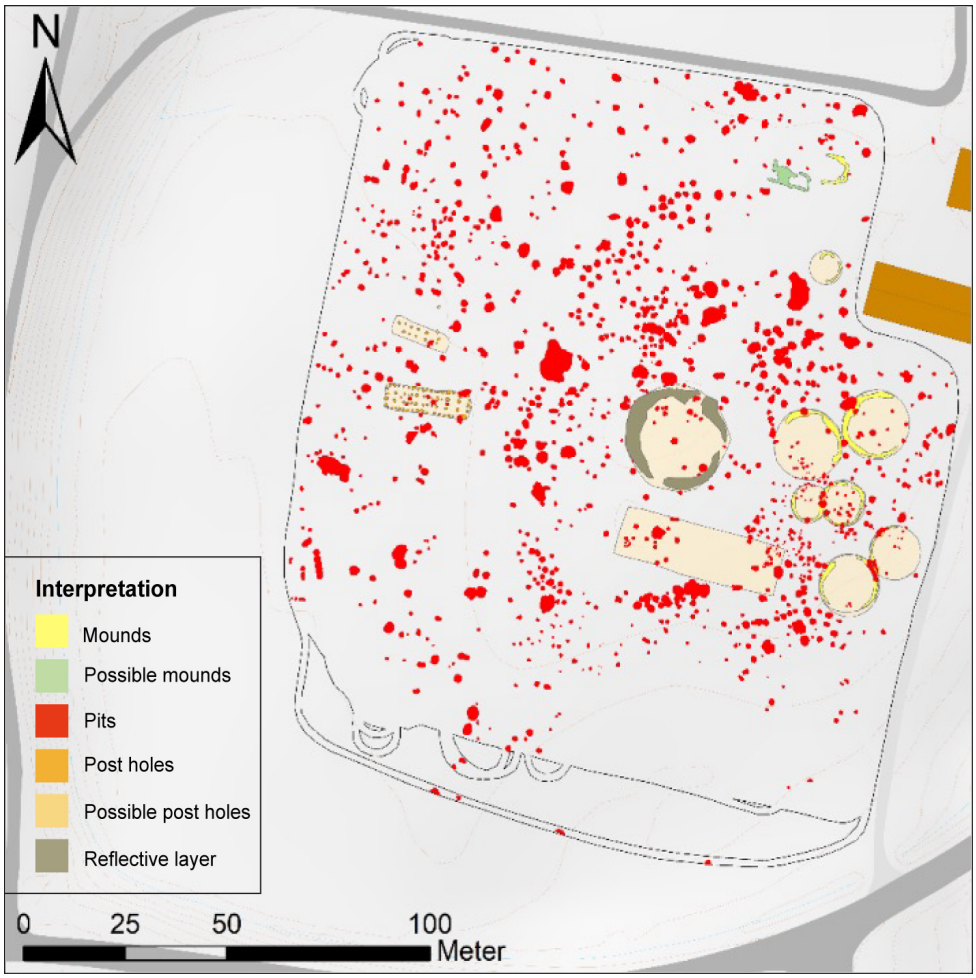

Figure 4.2: *Interpretation from the GPR data. Modified from (Fredriksen and Stamnes, 2019).*

4.2.1 Løykja - GPR Acquisition

The data collected from Løykja were obtained during a geoarchaeological survey conducted in August 2018. The GPR data was acquired using a step-frequency Kontur Geoscope Mark IV GPR with a 1.8 m wide DXG1820 antenna element. The antennas were configured in an array with a spacing of 7.5 cm, and the frequency range was set between 50 and 3000 MHz. With this configuration, the number of GPR channels is 24. To ensure accurate positioning, a GNSS receiver was integrated with the GPR system. The extensive survey covered a substantial area, totaling 24 596 square meters. The in-lines and cross-lines are oriented NE-SW and NW-SE, respectively. Additionally, the data records over a 30-ns time window (TWT). The Figure 4.3 shows how the data from Løykja was collected, by mounting the GPR to a car. The corresponding swath pattern from the survey is displayed to the right (see Section 2.3). In total, the survey covered an area of approximately 24600 m^2.

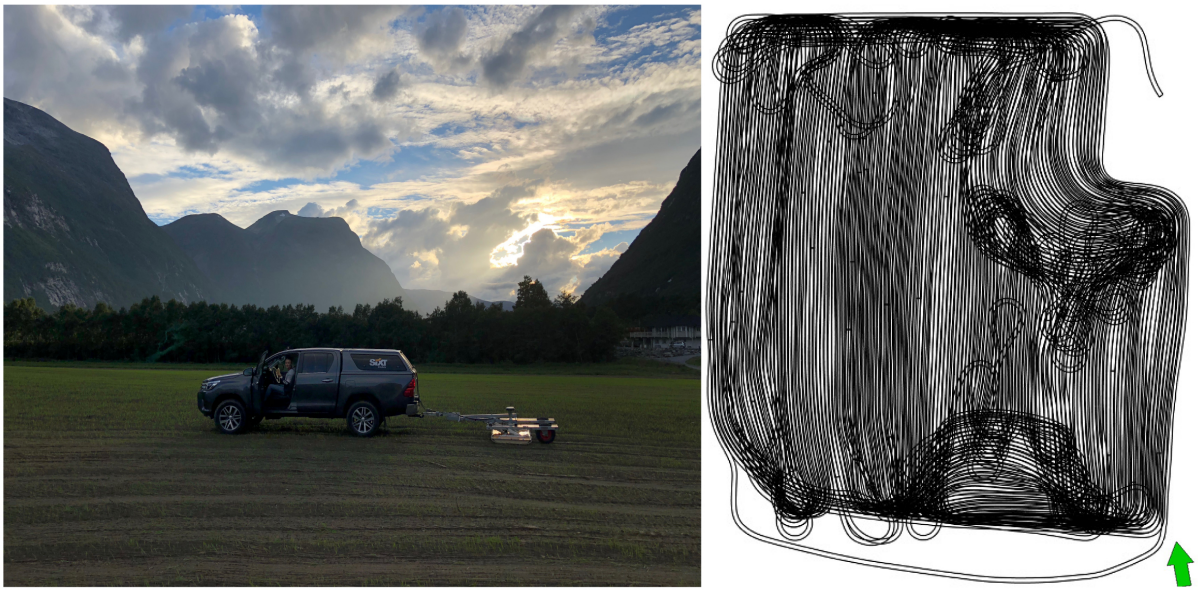

Figure 4.3: *Løykja GPR setup, where the GPR is mounted to the car (to the left) with corresponding swath pattern (to the right).*

4.2.2 Løykja - GPR Processing

GPR data processing is crucial to enhance data quality, employing various processing techniques to obtain the highest-quality image possible. This step is of paramount importance before the data can be interpreted and analyzed for attributes.

The data collected at Løykja underwent processing using Kontur's Examiner software, specifically developed for GPR data processing (Kontur, 2022). Initially, interference suppression was applied to eliminate external interference sources, such as waves from mobile phones. Step-frequency, record amplitude and phase, therefore we need to do a Fourier transform. In Examiner, this processing step is referred to as the Inverse Selective Discrete Fourier Transform (ISDFT), resulting in a time-domain image characterized by high resolution (Sala et al., 2012).

Subsequently, a Background removal (BGR) filter is applied as part of the processing. This filter is essential for eliminating unwanted signals and enhancing the clarity of the GPR data. It helps in isolating the features of interest from the background noise, further improving the quality of the data (Sala et al., 2012).

Finally, after these processing steps, migration is performed. Migration is a technique that refines the data by correcting for the effect of the propagation of EM waves in the subsurface. It ensures that the subsurface features are accurately positioned in the resulting image, allowing for more precise interpretation and attribute analysis.

The following Table 4.1 display the processing methods, with corresponding parameters, used for the Løykja dataset.

Table 4.1: *GPR processing parameters in Examiner, where ϵ_r is the relative permittivity, and time ground refers to zero-time (see Section 2.3.1).*

Process	**Value**
ϵ_r	8
Time ground (ns)	0.309
Interference Suppression	Power limit (dB): 10 Output percentage: Disabled
ISDFT	Attenuation: 0.04 Kaiser Kaiser beta: 3 Full BW: Enabled Max frequency (MHz): 1900 Cut off limit (MHz): 500
Autoscale	Percentage below max: 100 Multiplier: 10 Time to remove (ps): 10
BGR (high pass)	Filter length (m): 20 BGR removal (%): 100 Start depth (ns): 6 Transition zone sixe (ns): 1
Migration (time-domain)	Maximum radius (m): 0.55 Half angle (degrees): 45
Thick Slices	Slice thickness (ns): 1.83 Calculate: Average value
Autoscale	Percentage below max: 95 Multiplier: 1 Time to remove (ps): 0

After processing, the data can be interpreted. In Examiner the data is displayed with an inline and a crossline section, accompanied by corresponding trace lines that depict the real trace and magnitude (envelope), illustrated in Figure 4.4. In this particular section, a post hole is marked, and hence, the signal depicted in this figure corresponds to the presence of the post hole.

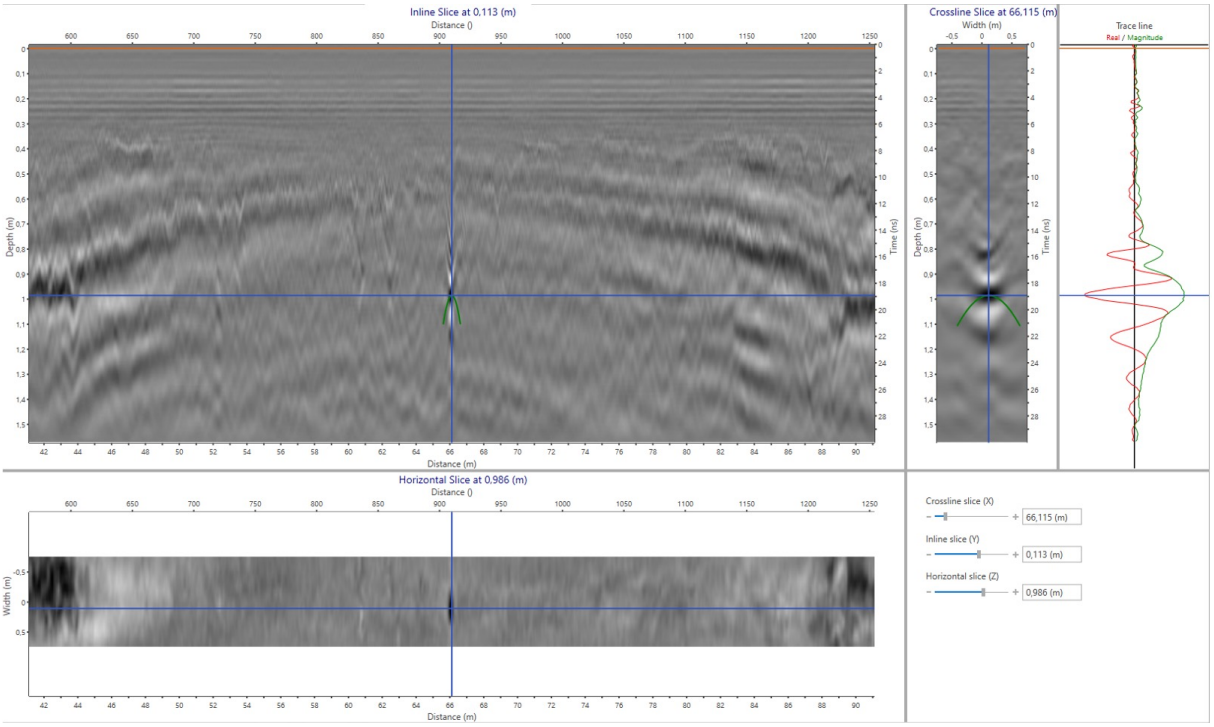

Figure 4.4: *Shows how the view of the data is set up in Examiner with inline and cross line section and time slice. Additionally, the trace is shown as real trace (red) and magnitude (green).*

4.2.3 Frequency analysis

The frequency spectrum, illustrated in Figure 4.5, is derived from Petrel using the processed data. The spectrum ranges from 0 Hz to 4100 MHz, with a bandwidth extending from 50 MHz to 490 MHz, with a central frequency at 260 MHz. Notably, the shape of the spectrum appears somewhat distorted, as the bandwidth ideally should be wider and flatter. This distortion was also observed in the frequency spectrum in Malå Vision (GPR software program). To address this, applying a De-wow filter could potentially attenuate lower frequencies and rectify the observed effect.

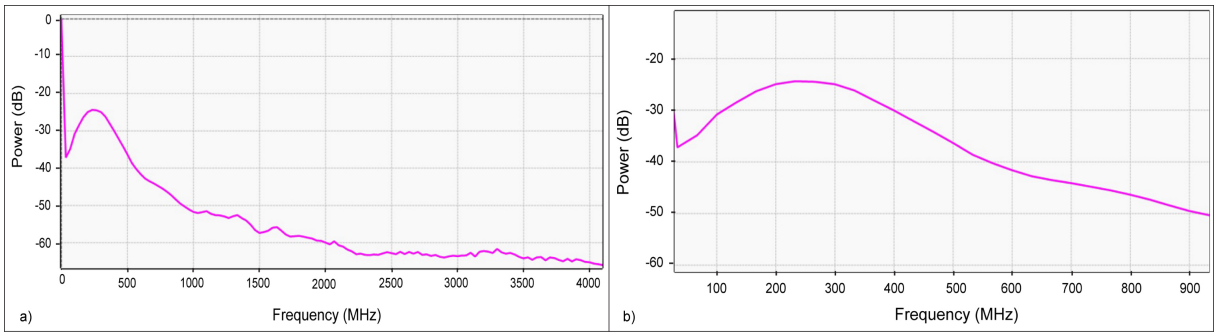

Figure 4.5: *a) Frequency spectrum, taken form Petrel, from the processed data. b) Bandwidth.*

4.2.4 Data quality

When conducting analyses and presenting results, the quality of processed data plays a pivotal role. Unlike seismic data, the inlines and crosslines generated by GPR exhibit distinct characteristics. In GPR data, the primary focus often centers on diffractions, such as those caused by buried stones, pipes, or other objects where strong EM-impedance occurs. Figure 4.7 illustrates strong GPR signals in both the inline and crossline profiles, which correspond to buried stones likely associated with previous cooking pits. The effectiveness of detecting these features hinges on data quality, with a particular emphasis on resolution, and strong EM-impedance contrast.

The primary objectives in this dataset are the identification of post holes, cooking pits, and burial mounds. These targets are distinguishable from the surrounding soil by their significantly higher amplitude. However, in regions where the soil is predominantly composed of glaciofluvial deposits, detecting these targets has proven to be more challenging.

From the processed data, the average wave velocity in the GPR data is 0.11 m/ns, which corresponds to a relative permittivity ϵ of 8 (Table 4.1). The vertical resolution of the GPR data, determined using the $\lambda/2$ criterion, is approximately 0.229 m. The dominant frequency of the data is 240 MHz, and the bandwidth ranges from 30 to 490 MHz.

Figure 4.6 provides an overview of the entire surveyed area at Løykja. While the burial mound area focuses on one specific burial mound, it is worth noting that several other burial mounds in proximity to this area have also been interpreted, as depicted in Figure 4.2. However, the decision to study the specific burial mound in greater detail was influenced by the strong amplitudes in the foot ditch area of this particular mound.

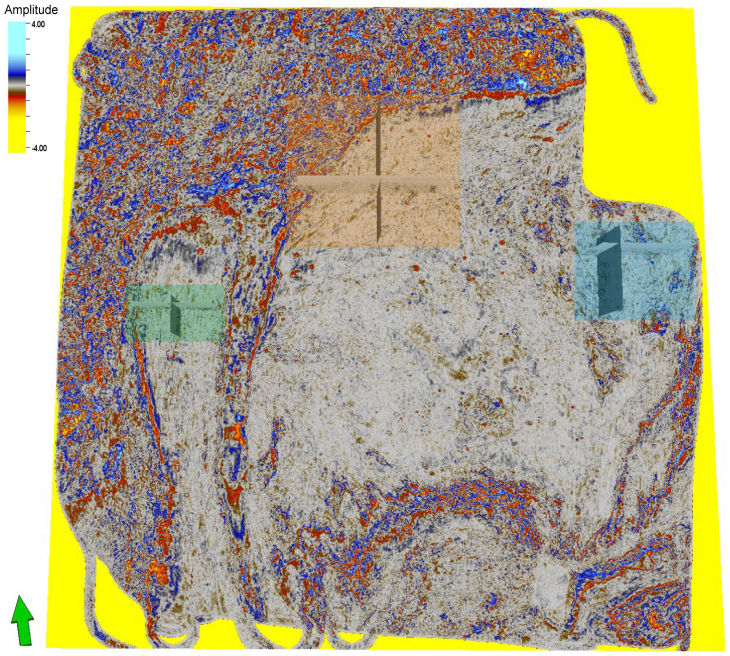

Figure 4.6: *Løykja with areas of the archaeological targets location. Faded red: cooking pits area. Faded green: post holes area. Faded blue: burial mound area.*

The Figures 4.7, 4.8 and 4.9 show how the different archaeological features behave in the GPR data. The cooking pits appear as high-amplitude features with a shallow dip in the inline and Xline. In the time-slice, these features are visible as circular objects with strong amplitudes (Figure 4.7). This distinctiveness is primarily due to the presence of organic matter, resulting in higher water content compared to arid substrates like dry sand. The Figures 4.8, 4.7, and 4.9, each showcasing distinct archaeological features, illustrate the quality of the data, with each feature visible.

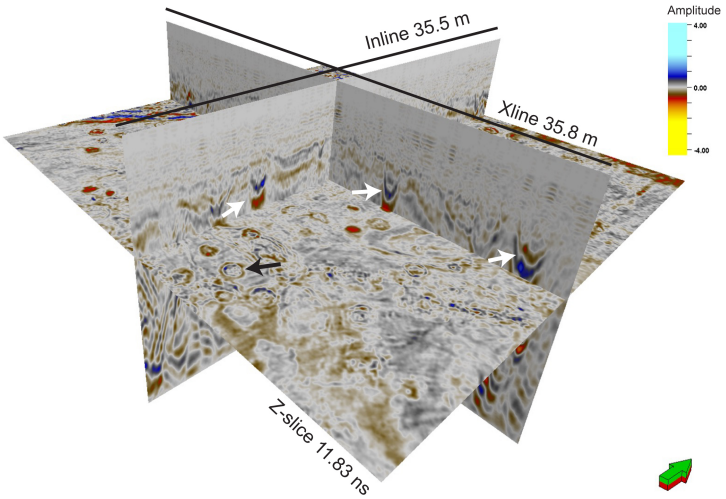

Figure 4.7: *GPR cube of cooking pits showing their behavior with the surrounding soil, shown as faded red square in figure 4.6. White arrows: cooking pits on the inline and Xline. Black arrow: cooking pit on time-slice, denoted as Z-slice in the figure.*

The post holes are discernible as small structures with strong GPR signal in the inline and Xline. In the time-slice, these features appear as small circular events with strong amplitudes (Figure 4.8).

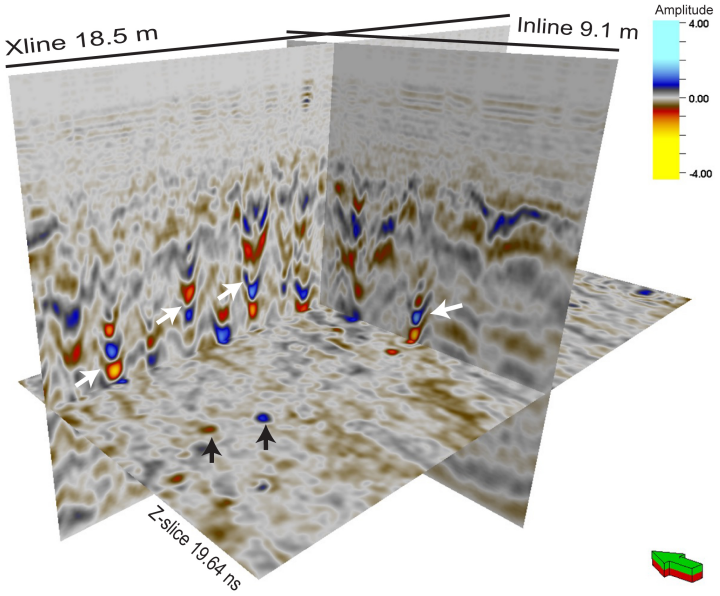

Figure 4.8: *GPR cube of post holes showing their behavior with the surrounding soil, shown as faded green square in figure 4.6. White arrows: post holes on the inline and Xline. Black arrows: post holes on time-slice, denoted as Z-slice in the figure.*

In the GPR time-slices, the burial mounds appear as substantial circular formations, often as ring ditches surrounding the removed mound, or as collected stone filling still left in the subsurface, as shown in Figure 4.9. On the inline and Xline it is visible as a steep dip.

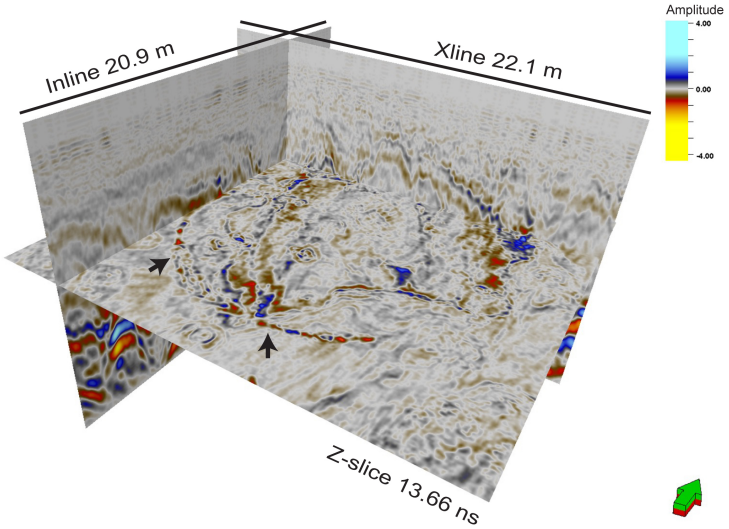

Figure 4.9: *GPR cube of burial mound showing its behavior with the surrounding soil, shown as faded blue square in figure 4.6. Black arrows: burial mound on time-slice, denoted as Z-slice in the figure.*

4.3 Methodology

The processed time migrated data was imported into SLB's Petrel software to perform attribute analysis. In this study, I focused on analyzing attributes for archaeological targets such as post holes, cooking pits, and burial mounds. Since each of these targets exhibits distinct characteristics, a wide range of attributes has been extracted to capture their unique behaviors. Additionally, some processing methods, including migration, were executed using Kontur's Examiner software.

4.3.1 Volume attributes

Volume attributes are derived from GPR data and serve to improve or quantify features of interest. Attributes such as amplitude and instantaneous attributes capture the energy within the data, making them valuable for enhancing the imaging of high-amplitude features (Li and Zhao, 2014). Additionally, the variance attribute is well-suited for improving imaging due to the inherent variations in GPR data.

In this study, I have applied 15 attributes to the time-migrated data. Each attribute has been carefully selected based on the existing literature on volume attributes and insights from previous studies. The intention behind incorporating these attributes is to enhance the value of the original data. A description of the attributes can be found in Chapter 3.

In the case of the cooking pits, the similarity between these features and pockmarks studied in seismic analysis has led to the assumption that attributes commonly applied to pockmarks could yield favorable results for cooking pits. Pockmarks, for reference, are circular structures found on the seafloor, resulting from the accumulation of subsurface gas. This gas carries fine-grained sand, which is subsequently deposited in the sea. The coarser-grained sediments, in contrast, settle on the seabed, leading to the formation of depressions (Chopra and Marfurt, 2023). In seismic analysis, Chopra and Marfurt (2007) recommend the use of the coherence attribute for visualizing pockmarks, to exhibit their characteristics often present as circular features in seismic data (see Figure 4.10). However, it is important to note that the material composition between these two structures differ significantly.

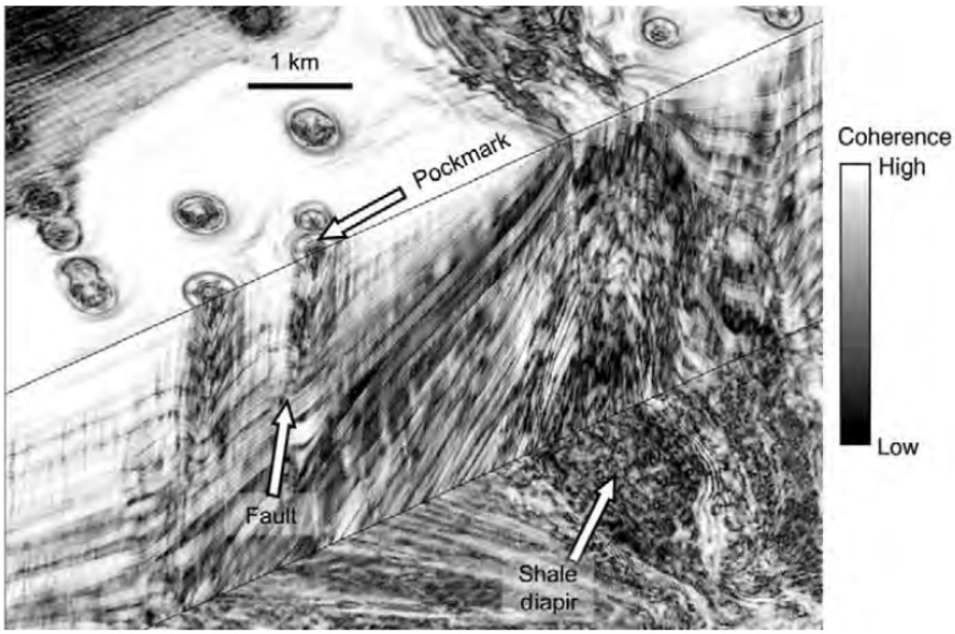

Figure 4.10: *Coherence cube showing the structure of the pockmarks, both viewed in time slice and cross section. Modified from (Chopra and Marfurt, 2007)*

Concerning the burial mounds, there is an analogy with reef structures studied in seismic data. Some reef structures exhibit mound-like features, which leads to the consideration of attributes that enhance the imaging of such structures should yield good results for for burial mounds. The coherence attribute, as recommended by Chopra and Marfurt (2007), is one such option. Another study by Wang et al. (2016) suggests employing spectral decomposition with RGB blending, GLCM energy, as well as coherence, for this purpose.

When considering post holes, it is important to note that these structures differ significantly from other geological features. Therefore, the choice of attributes for post holes is primarily based on attribute calculation methods and their resulting outputs. Given the strong GPR signal associated with post holes, attributes related to amplitudes, such as RMS amplitude and envelope, are expected to yield effective results.

Some of the attributes used have been chosen based on previous studies regarding attribute analysis of GPR data in archaeology, such as envelope (Trinks et al., 2010) and GLCM (Zhao et al., 2016). While other have been chosen based on studies regarding attributes for seismic analysis, such as RMS amplitude, variance and edge enhancement (Chopra and Marfurt, 2007).

The attributes generated in this study are associated with distinct color-bars. Petrel

provides predefined color-bars for different attribute types, including instantaneous frequency, instantaneous phase, chaos, and dip illumination. Additionally, specific color-bars developed by Equinor in Petrel have been employed for particular attribute types. For instance, Equinor has designed color-bars for attributes like RMS amplitude and variance, which have been utilized accordingly.

4.3.2 Surface attributes

Surface attributes involve extracting values from interpreted horizons, and are often referred to as event based attributes (Zhao et al., 2013). In Petrel, there are several surface attributes available, with amplitude attributes being the most commonly used, as explored in this study. A notable characteristic of surface attributes is their ability to extract values both above and below the horizon, where the users can define a specific window for attribute extraction. The surface attributes utilized in this study, along with their characteristics, are listed in Table 4.2.

Table 4.2: *Surface attributes used in this study with respective description*

Attribute	**Description**
RMS amplitude	A statistical amplitude. Simply the root-mean-square (RMS) amplitude of a single-trace within a user-specified window. See Section 3.1.2 for more information.
Max, mean and min	Calculates the max, mean and min amplitude value.

4.3.3 Geobody

The box probe tool allows users to extract a specific region from a volume and subsequently create 3D models. By adjusting opacity and selecting desired values for extraction, it becomes possible to generate a geobody of the area of interest. For this method, the attribute volume that best visualizes the desired features should be used as input parameters to achieve the optimal end result. In the case of the Løykja data, the RMS amplitude map proved most effective for generating geobodies of the post holes, while the variance map worked best for the cooking pits.

4.3.4 Multi-attribute analysis - Neural Network

The neural network, a type of machine learning model, is increasingly being applied in seismic facies classification, as demonstrated in studies like those by (Alaudah et al., 2019; Araya-Polo et al., 2017; Zhao, 2018). The method relies on a predefined model, where each seismic facie is classified by their character and seismic trace. This model, often referred to as a training model, guides the neural network in classifying each facie. When this trained model is applied to the original seismic data, the neural network uses the information it has learned to classify seismic facies within the seismic dataset. Neural networks are being employed in various fields, and in the context of seismic analysis, they offer an effective means of seismic facies classification. Due to previous studies, this method has also been tried in this study.

1. Make a model from generated attributes which have improved interpretation.
2. Used model for further extraction.

4.4 Seismic attributes - GPR

In the context of GPR, the sources and measured physical properties differ from those in seismic exploration, but both are based on the same wave theory. This resemblance has led to the adoption of similar processing and interpretation techniques for GPR data, employing methods originally developed for seismic data (Grasmueck, 1996; Baker et al., 2001).

4.4.1 Geology

In the field of exploration geology, seismic attributes serve as valuable tools for imaging various geological features, including faults, stratigraphy, and the detection of hydrocarbon reservoirs (Randen and Sønneland, 2005). Many of these attributes are specifically developed to enhance the visualization of particular geological structures. For instance, edge-detecting attributes have been devised for fault detection. GPR has emerged as a valuable method for studying geological formations analogous to hydrocarbon reservoirs found at significant depths. In a study conducted by Yue et al. (2019), GPR was employed to investigate a point bar - an important reservoir feature in meandering depositional systems, often studied in seismic exploration. The research encompassed a wide range of

attributes, including average energy, RMS amplitude, and dominant frequency.

4.4.2 Archaeology

Over the past decade, the utilization of attributes in 2D and 2.5D GPR datasets has, to some extent, become a standard practice. Among the most commonly used attributes are instantaneous amplitude, energy, and coherence (Zhao et al., 2015; Forte et al., 2021; Zhao et al., 2013). However, the application of attributes in full 3D GPR data has only recently gained traction (Forte et al., 2021). Despite numerous studies exploring the use of attributes in GPR data, their adoption in archaeological studies has yet to become a standard practice (Manataki et al., 2021). It is important to note that seismic attributes are originally developed for seismic events and geological structures. When applying attributes to archaeological GPR data, it is crucial to consider this distinction.

4.5 Workflow

Below is a list with a suggested workflow. It is important to note that this workflow does not need to be followed in a strict order, but it serves as a guide for extracting information from the processed data.

1. Import processed data in Petrel.
2. Quality check the data and adjust settings in Petrel for a better view of the data.
3. Before exploring attributes, start with variance, RMS amplitude and structural smoothing.
4. Use parameter control to test different settings, and realize the cube when you are happy with the result.
5. Further extract other volume attributes. Use parameter control.
6. Horizon interpretation on structural smooth cube.
7. Extract surface attributes.
8. Geobody extraction.

Chapter 5

Results

The next chapter will present the results from seismic attribute extraction on GPR data. Given the extensive survey area, the results have been divided into three main sections, each focusing on a specific target: post holes (Section 5.1), cooking pits (Section 5.2), and the burial mound (Section 5.3). These sections will display the outcomes of various attributes tested for these targets. Although several attributes have been examined, some of them listed in Table 3.1, only the attributes that yielded the best results are showcased. The results illustrate that certain attributes are effective for specific structures but not as suitable for others.

A common way to present GPR data is through time slices, and this approach will be employed here (Zhao et al., 2013). Cross sections will also be shown for attributes that offer valuable information from a profile perspective. An extensive overview of the entire survey area, including different seismic attribute extractions, presented in Appendix A.1.

5.1 Post holes

The post holes are detected at depths ranging from 15 ns to 21 ns. The variation in depth is expected, given that archaeological features like post holes can have different depths based on their construction. Although post holes are typically challenging to identify in GPR datasets, the data from Løykja reveals a discernible pattern of reflections. These reflections are arranged in a manner that outlines the structure of a longhouse, complete with roof-bearing posts and remnants of smaller post holes from the outer walls.

5.1.1 Volume attributes

Figures 5.1, 5.2, and 5.3 display the results of the tested attributes for the area where the post holes have been located. Some of the results, when compared with the original amplitude data (Figure 5.1a), show clearer structures. The RMS amplitude attribute (Figure 5.1b) manages to extract the strong signal from most of the post holes. This map was calculated using a time window of 5 ns (see Equation 3.3). The variance attribute (Figure 5.1c) was calculated with a filter length of 3x3 traces, with vertical smoothing of 200 (see Section 3.1.1). The contours of the post holes are more visible with this attribute, and in comparison with the RMS amplitude map, the number of post holes is more apparent. The white areas, corresponding to low values, on the variance map indicate little variance, signifying semblance between the traces. The black area,corresponding to high values, signifies variance between the traces. In Figure 5.1d, a blending of RMS amplitude and variance is presented. The influence of the variance attribute is more evident here, illustrating that the RMS amplitude map does not effectively depict the numerous post holes in this specific area, as previously mentioned.

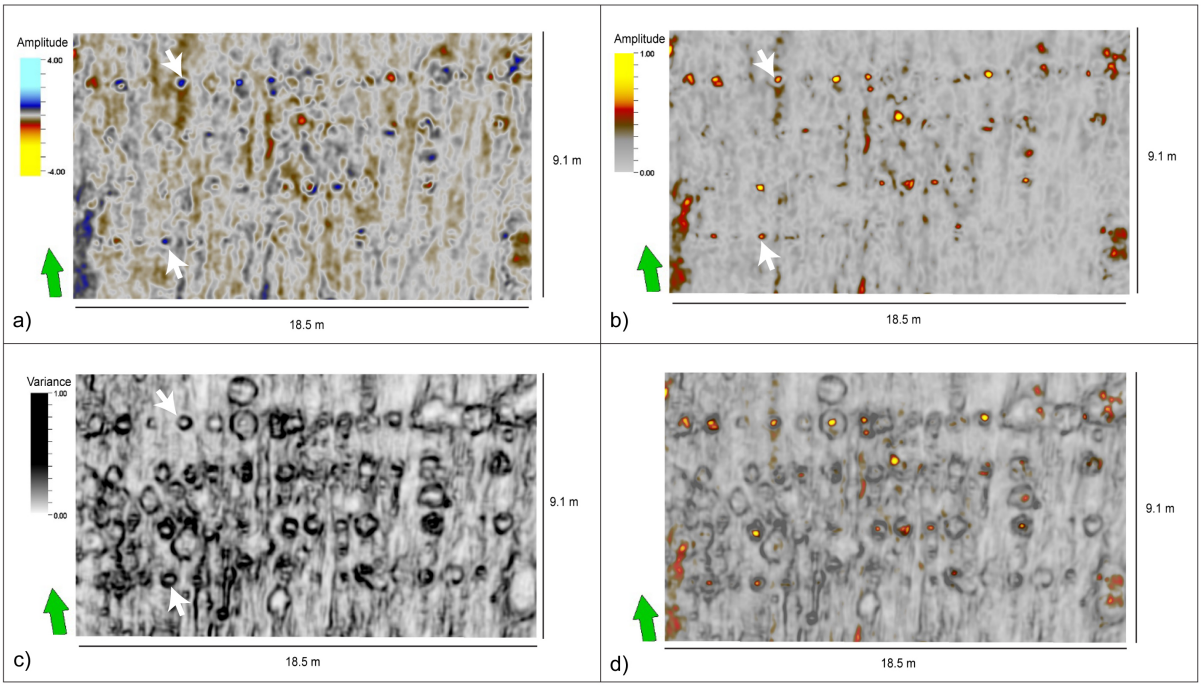

Figure 5.1: *Time slice at twt = -17 ns, where white arrows point at some of the post holes. a) original data, b) RMS amplitude, c) variance, d) Blending of variance and RMS amplitude.*

Figure 5.2 present the results from dip illumination, 3D edge enhancement, and chaos. The dip illumination map was (Figure 5.2a) generated using an illumination angle of $\theta = 130°$.

Although other angles were tested, this specific angle yielded the most promising results. However, it is important to note that this attribute did not enhance the image of the post holes, and making it challenging to interpret meaningful information from the image. The 3D edge enhancement (Figure 5.2b) captures some of the post holes, but due to increased smoothing (see Table 3.1), certain details are lost. The GLCM energy and entropy attributes (Figure 5.2c and 5.2d), visualized with a black-grey-white color-bar, succeed in imaging the post holes to some extent, enhancing their visibility compared to the original data.

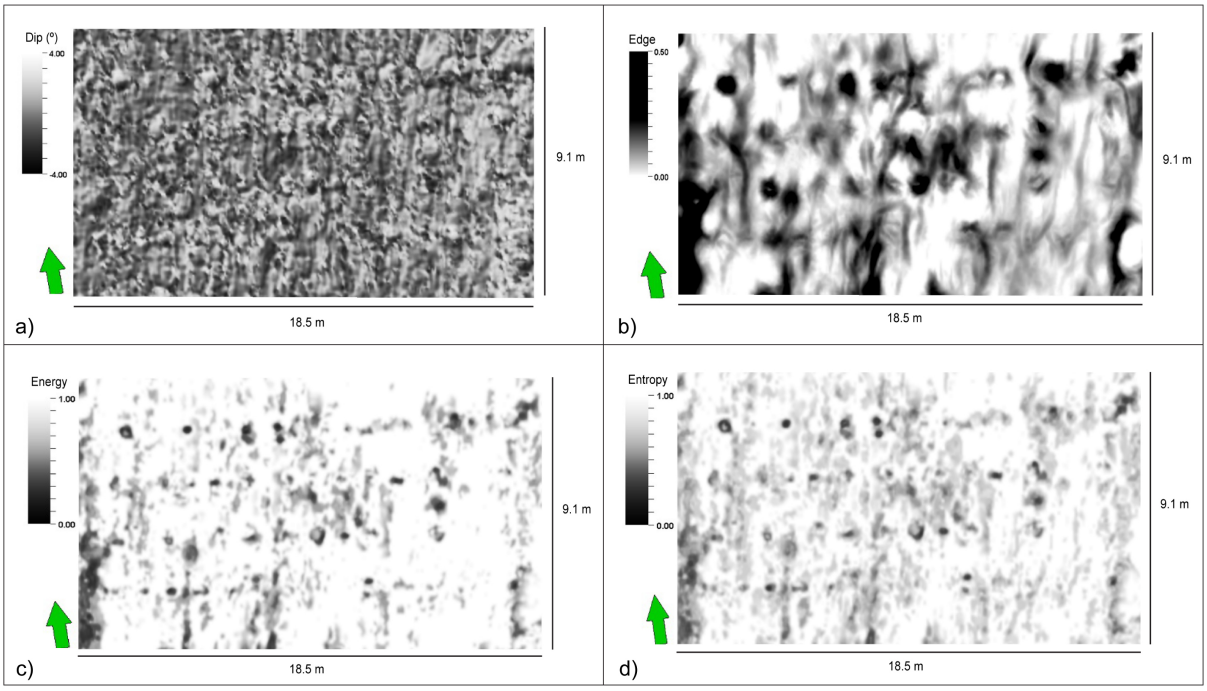

Figure 5.2: *Time slice at twt = -17 ns of post holes. a) dip illumination with* $\theta = 130°$*, b) 3D edge enhancement, c) GLCM energy d) GLCM entropy.*

Regarding the instantaneous attributes, these were calculated over a window of 83, and as shown in the figure, the envelope attribute (Figure 5.3a) produces the most promising results. Given the similarity between RMS amplitude and envelope attributes, the same color-bar has been applied to both. This attribute highlights the reflection strength of the post holes, making them more visible in the time slices. In contrast, the instantaneous phase (Figure 5.3b) does not significantly improve the visibility of the post holes and reveals limited information in this area. The color-bar used for this attribute is a built-in color-bar in Petrel, designed for instantaneous phase, which ranges from -180 to +180 (see Section 3.1.4). The cosine of phase attribute, shown in Figure 5.3c, is similar to instantaneous phase, but the black-white color-bar makes the visualization of the post

holes more appealing. The chaos attribute (Figure 5.3d) image the degree of chaos in the data. High values indicate areas with complex GPR pattern. In this case, it does not reveal any distinct structure, making it difficult to extract meaningful information from this attribute.

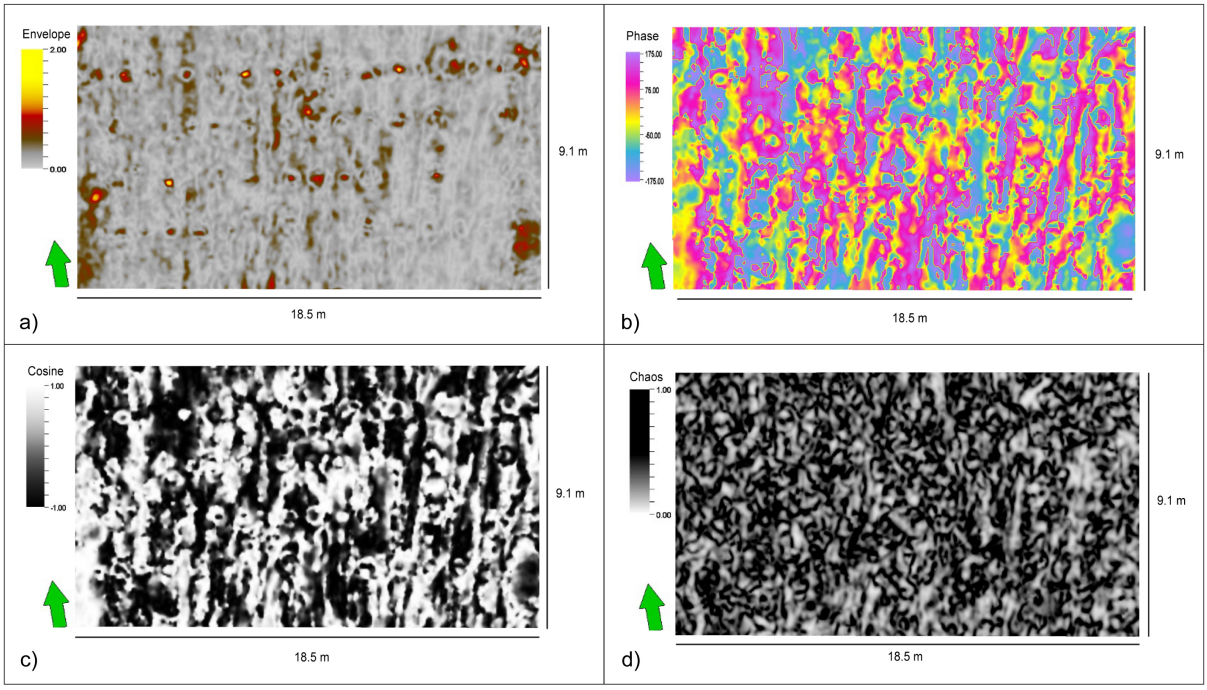

Figure 5.3: *Time slice at twt = -17 ns of post holes. a) envelope, b) instantaneous phase, c) Cosine of phase, d) Chaos.*

GPR profiles

In Figure 5.4, the attributes are displayed in profile view. The selected profile is the same X-line as shown in Figure 4.8. Some of the attributes are not displayed in cross sections as these attributes, such as chaos, dip illumination, and variance, do not give any significant results or information. Both the envelope (Figure 5.3b) and RMS amplitude (Figure 5.3c) show strong amplitudes around the post holes, and they can image the structure quite well. The Cosine of phase (Figure 5.3d) do enhance the imaging of the post holes to some extent, as also observed on the time slice. It shows more sharp edges. The 3D edge enhancement (Figure 5.3e) is able to image some of the post holes, but due to the smoothing, the image is somewhat blurred, resulting in less detail for small features. The GLCM energy (Figure 5.3f) manages to extract some information of the post holes, but is not as clear as the original data.

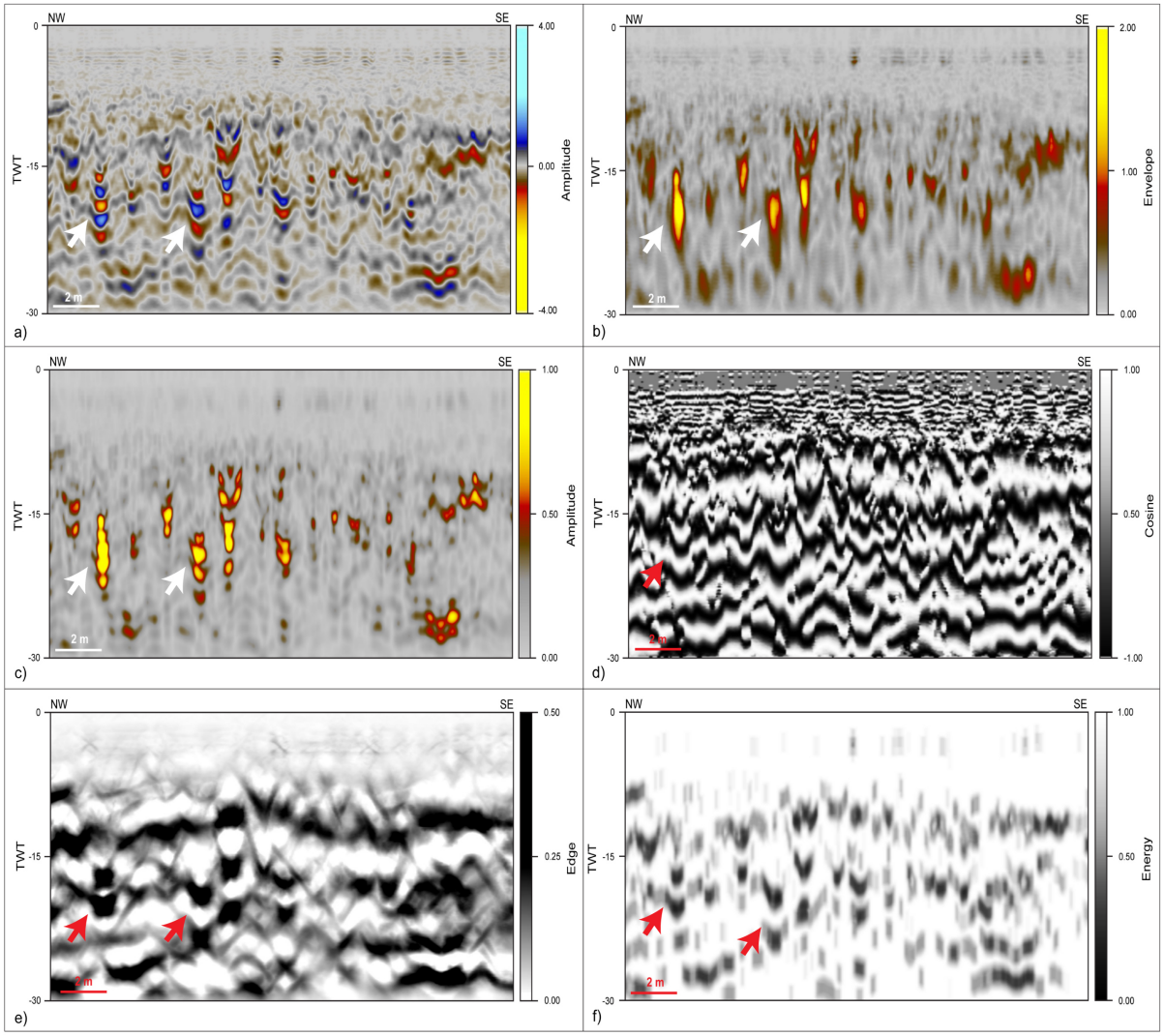

Figure 5.4: *Profile view of attributes for post holes, where TWT is represented in ns. a) Original data, b) envelope, c) RMS amplitude, d) Cosine of phase, e) 3D edge enhancement, f) GLCM energy. White and red arrows show the signal response from the post holes.*

5.1.2 Box probe and geobody extraction

The geobody extraction of the post holes was conducted using the RMS amplitude box prob as it displayed stronger signals. When performing geobody extraction, it is important to use an attribute that clearly displays the features to use as the box probe. Decreasing opacity, made the strong signal stand out, as shown in Figure 5.5b. The geobody extraction was then performed with 50 voxels and a maximum number of 255 geoblobs.

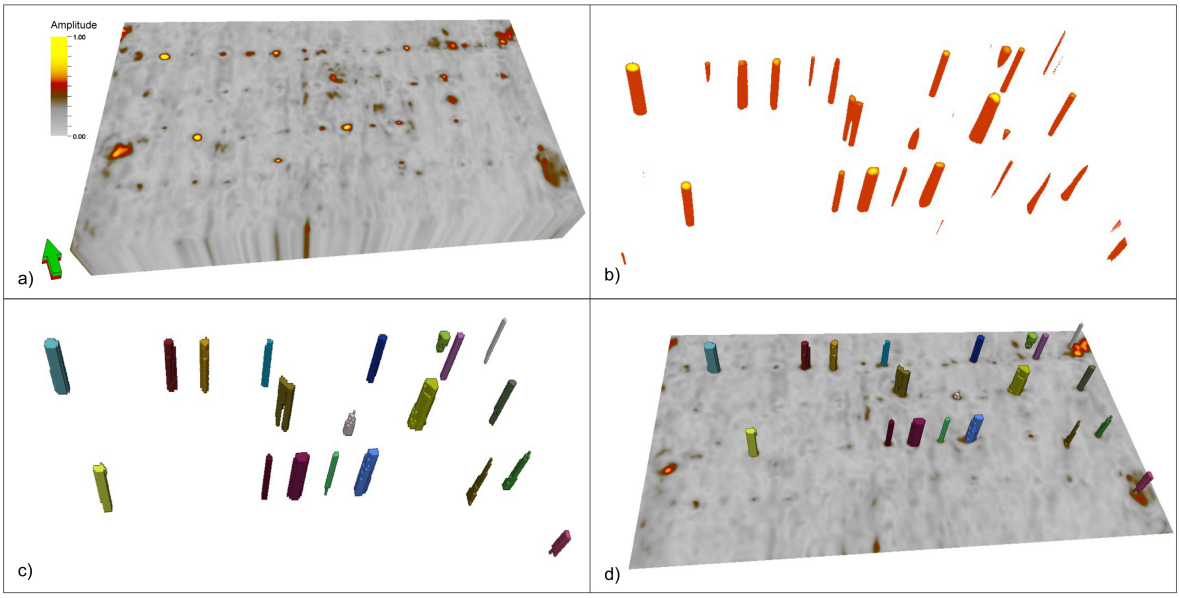

Figure 5.5: *Geobody extraction of the post holes. a) Boxprobe generated from the RMS amplitude map. b) By decreasing the opacity, only the strong reflections remain visible. c) Geobody extraction can then be performed, and only the strong reflections from b) will be assigned a geobody. d) The geobodies shown on an RMS amplitude time slice.*

5.2 Cooking pit

The cooking pits are visible at depths ranging from 7 ns to 18 ns. An important observation is the difference in soil properties in the area where the cooking pits have been studied. In Figure 5.6a and Figure 5.6b, one can see the difference in the response. In the northwest area, the soil is more heterogeneous, due to glacifluvial deposits, which results to strong and continuous amplitudes, whereas the southeastern part is more transparent. This affects the images of the cooking pits. In the heterogeneous soil, the signal from the cooking pits shows a low-amplitude response, whereas in the homogeneous soil, the signal from the cooking pits shows a high-amplitude response.

5.2.1 Volume attributes

The attributes that have been tested for the cooking pits are shown in Figure 5.6, 5.7, and 5.8. Just from the original data, it is possible to identify some cooking pits, but the strong signal from the stone-bearing cooking pits in the homogeneous soil makes the RMS amplitude map show the cooking pits more visibly. Here the RMS amplitude has been extracted with a time window of 5 ns. In the northwest corner, one can see that the soil is heterogeneous, making it harder to identify cooking pits (Figure 5.6a and 5.6b). The

variance map reveals the contours of the cooking pits within the homogeneous soil, making them easily distinguishable. However, in the heterogeneous soil, the identification of cooking pits becomes more challenging, as it is not as clear which features correspond to cooking pits and which do not. The variance map was generated with a 6x6 filter length (traces) and a vertical smoothing of 130. The blending of RMS amplitude and variance, shown in Figure 5.6d, enhance visualization of the cooking pits, and map different amplitude response.

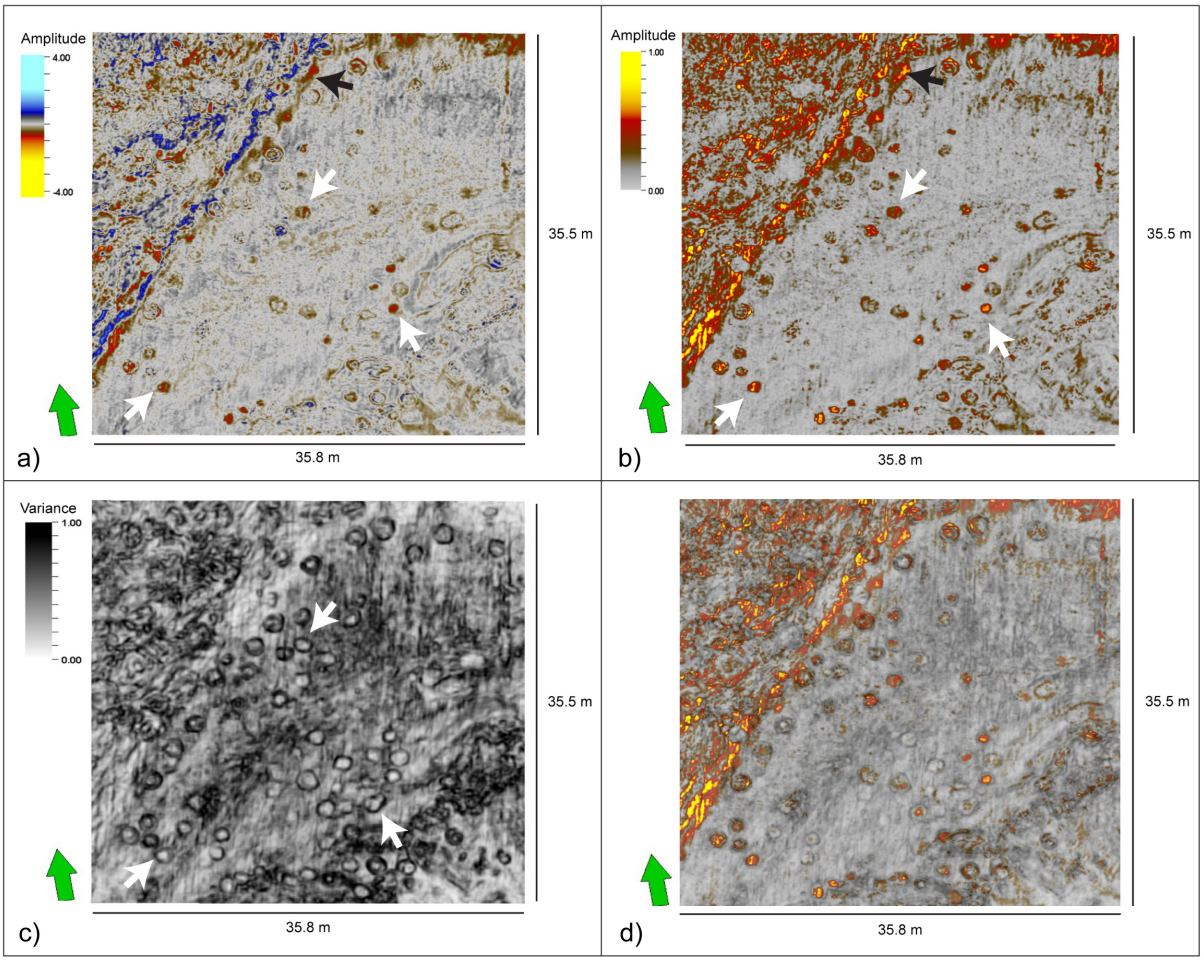

Figure 5.6: *Time slice at twt = -12 ns, where white arrows point at some of the cooking pits. a) original data, b) RMS amplitude, c) variance, d) Blending of RMS amplitude and variance. Black arrows mark the heterogeneous soil.*

The dip illumination attribute (Figure 5.7a) effectively illuminates the cooking pits more in the heterogeneous soil, as the structure is more visible near the northwest corner, which is not as evident for the other attributes. The illumination angle (θ) was set to 60°, as this provided the best results for imaging the cooking pits. The 3D edge enhancement, shown in Figure 5.7b, reveals a clearly defined boundary between the heterogeneous and homogeneous soil, but the cooking pits are less visible. The GLCM energy and entropy

attributes (Figure 5.8c and 5.8d) provide some visibility of the cooking pits, although not as effectively as other attributes.

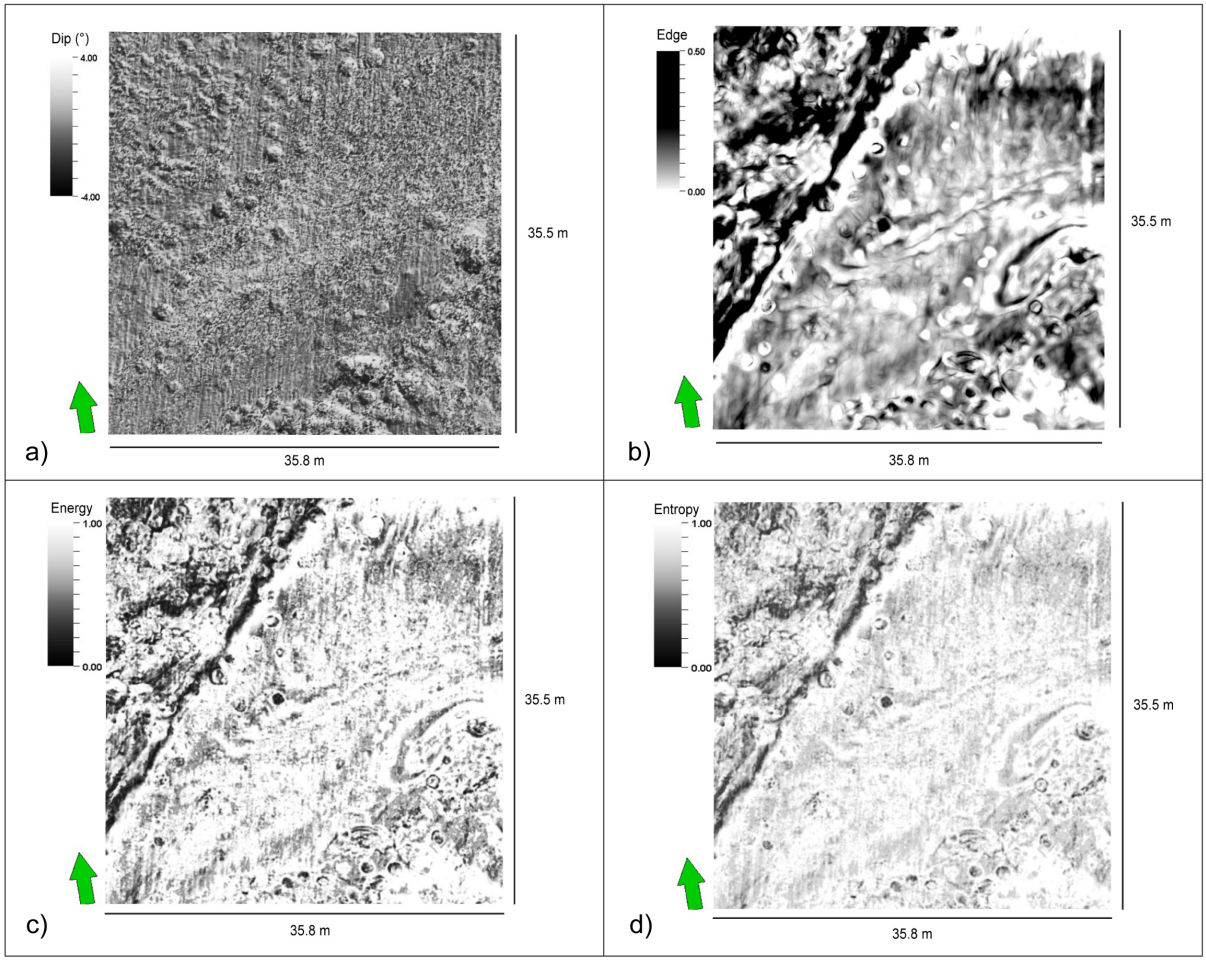

Figure 5.7: *Time slice at twt = -12 ns of cooking pits. a) dip illumination with* $\theta = 60°$*, b) 3D edge enhancement, c) GLCM energy, and d) GLCM entropy.*

The results from the tested instantaneous attributes for the cooking pits are consistent with the observations for post holes. The envelope attribute (Figure 5.8a) enhances the visibility of the cooking pits by highlighting them as strong signals, comparable to the RMS amplitude map. In contrast, the instantaneous phase attribute and cosine of phase (Figure 5.8b and 5.8c respectively) reveals some of the cooking pits, but not as clearly as other attributes. The same as for the post holes, the color-bar on the cosine of phase has an impact of the image. The chaos attribute (Figure 5.7d) does not enhance the imaging, and only a few cooking pits are visible with this attribute.

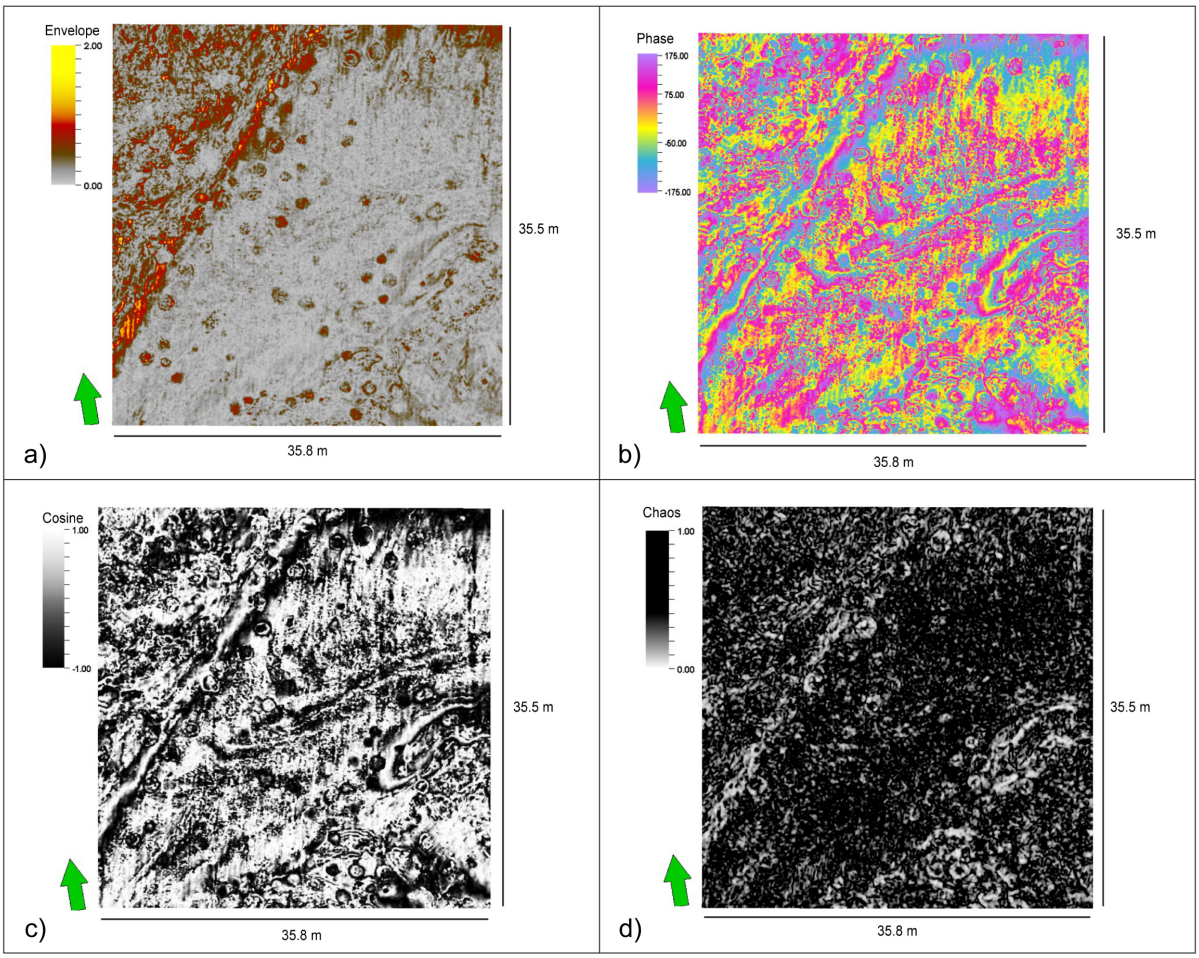

Figure 5.8: *Time slice at twt = -12 ns of cooking pits. a) envelope, b) instantaneous phase, c) Cosine of phase, and d) Chaos.*

GPR profiles

The GPR profile of the cooking pits computed with different attributes are shown in Figure 5.9. In this cross section, the surrounding soil is mostly transparent, and therefore response from the cooking pits are clearly visible. The the envelope and RMS amplitude (Figure 5.9b and 5.9c respectively) produce similar results, and is able to detect the cooking pits shown in the profile. The cosine of phase, shown in Figure 5.9d is quite sharp, and images the shape of the cooking pits to some degree. Also the 3D edge enhancement (Figure 5.9e) is able to image quite good results of the cooking pits, but the attribute is quite blurred. The GLCM energy (Figure 5.9f) manages to distinctly image the cooking pits.

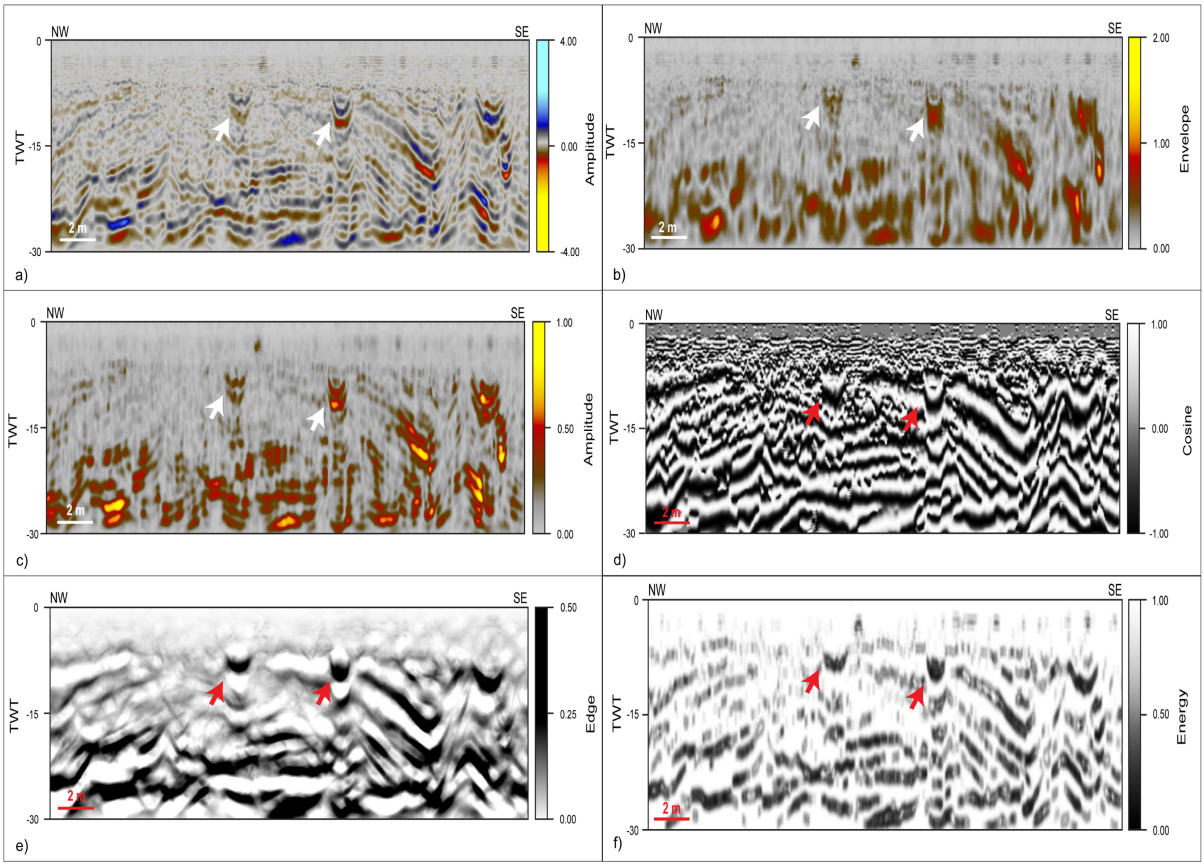

Figure 5.9: *Profile view of attributes for cooking pits, where TWT is represented in ns. a) Original data, b) Envelope, c) RMS amplitude, d) Cosine of phase, e) 3D edge enhancement, f) GLCM energy. White and red arrows show the signal response from the cooking pits.*

5.2.2 Multi-attribute

The multi-attribute neural network approach applied to the cooking pit cube involved generating a multi-attribute cube using the original data, the variance attribute, and the RMS amplitude attribute as input cubes. These cubes were chosen based on the results from the respective attributes. The output of this approach was a training model, as shown in Figure 5.10. Five classes were used, and the results indicate that the method was able to classify the cooking pits to some extent. It is worth noting that testing this training model on the entire Løykja dataset would be an interesting approach, although it was not possible due to limitations in Petrel.

Additionally, an attempt was made to generate a training model with only three classes, but it did not effectively classify the cooking pits; instead, it primarily classified different soil types. This method has shown promise in various studies related to multi-attribute techniques for seismic facies and fault detection, and it has demonstrated good results

in well log interpretation. Thus, it holds the potential to enhance the efficiency of interpretation in archaeological GPR studies, ultimately saving time. However, due to the time-consuming calculations and poor results in the other areas, the method is only demonstrated for the cooking pits in this study. It was tested over the entire survey area, but the computational demands in Petrel posed a limitation.

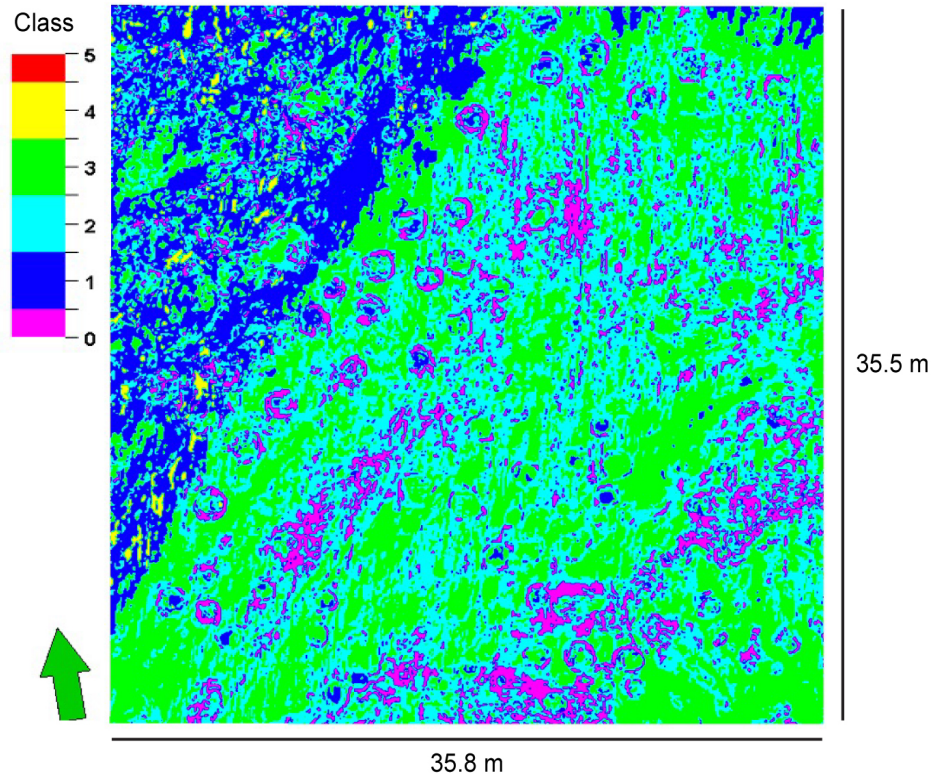

Figure 5.10: *Computed training model from Neural Network method from the cooking pit cube. Time slice at twt = -12 ns.*

5.3 Burial mound

The burial mound is visible at depths ranging from 9 ns to 17 ns. I focused on studying one burial mound up close because of the distinct ring ditch around it. However, visualizations of all three burial mounds located at Løykja is illustrated in Appendix B.1. The ring ditch is visible on the time sections (Figure 5.11a) but only appears as a small discontinuity on the cross sections (5.14a). This circular feature is challenging to compare with other geological features, so the assumption that seismic attributes would enhance the imaging of this feature was relatively modest.

5.3.1 Volume attributes

The results from the attributes generated for the burial mound are shown in Figure 5.11. The RMS amplitude map (Figure 5.11b) was generated with a time window of 5 ns, and it is, to some degree, able to image the strong amplitude of the ring ditch. The variance map (Figure 5.11c) visualizes the contours of the ring ditch. Her the variance was computed with a filter length (traces) of 3x3 and vertical smoothing of 130. Regarding the blending of RMS amplitude and variance (Figure 5.11d), the impact of the variance map is prominently displayed, while the influence of the RMS amplitude is barely discernible.

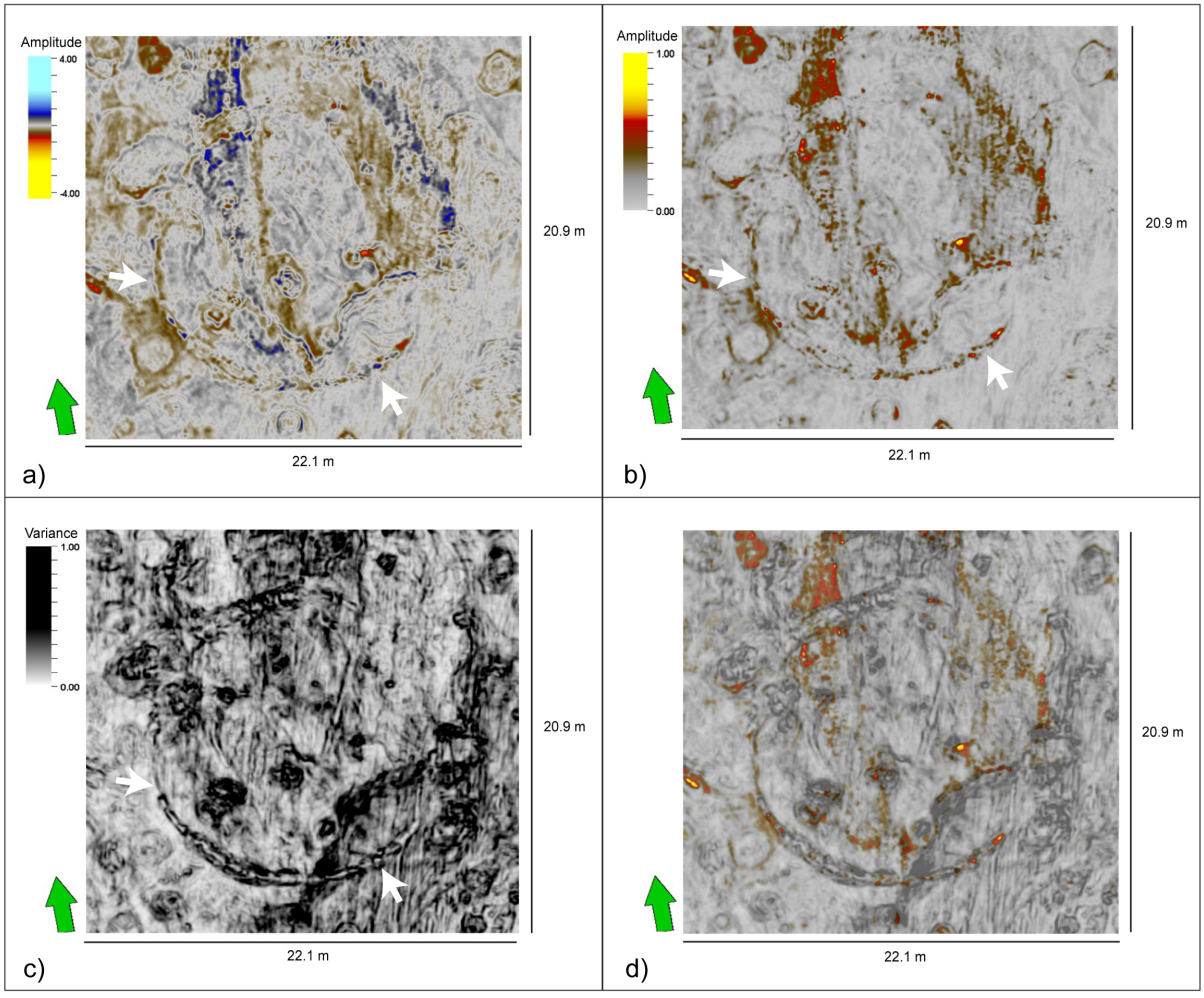

Figure 5.11: *Time slice at twt = -12 ns, where white arrows point at the burial mound. a) original data, b) RMS amplitude, c) variance, and d) Blending of RMS amplitude and variance.*

The dip illumination attribute (Figure 5.12a) effectively highlights the ring ditch around the burial mound, providing a clear visualization of this feature. The 3D edge enhancement (Figure 5.12b) manages to image the ring ditch to some extent, although the attribute's smoothing effect leads to a loss of detail. The GLCM energy and entropy (Figure

5.12c and 5.12d) display more or less the same result as the envelope, but the GLCM energy show a more distinct ring ditch.

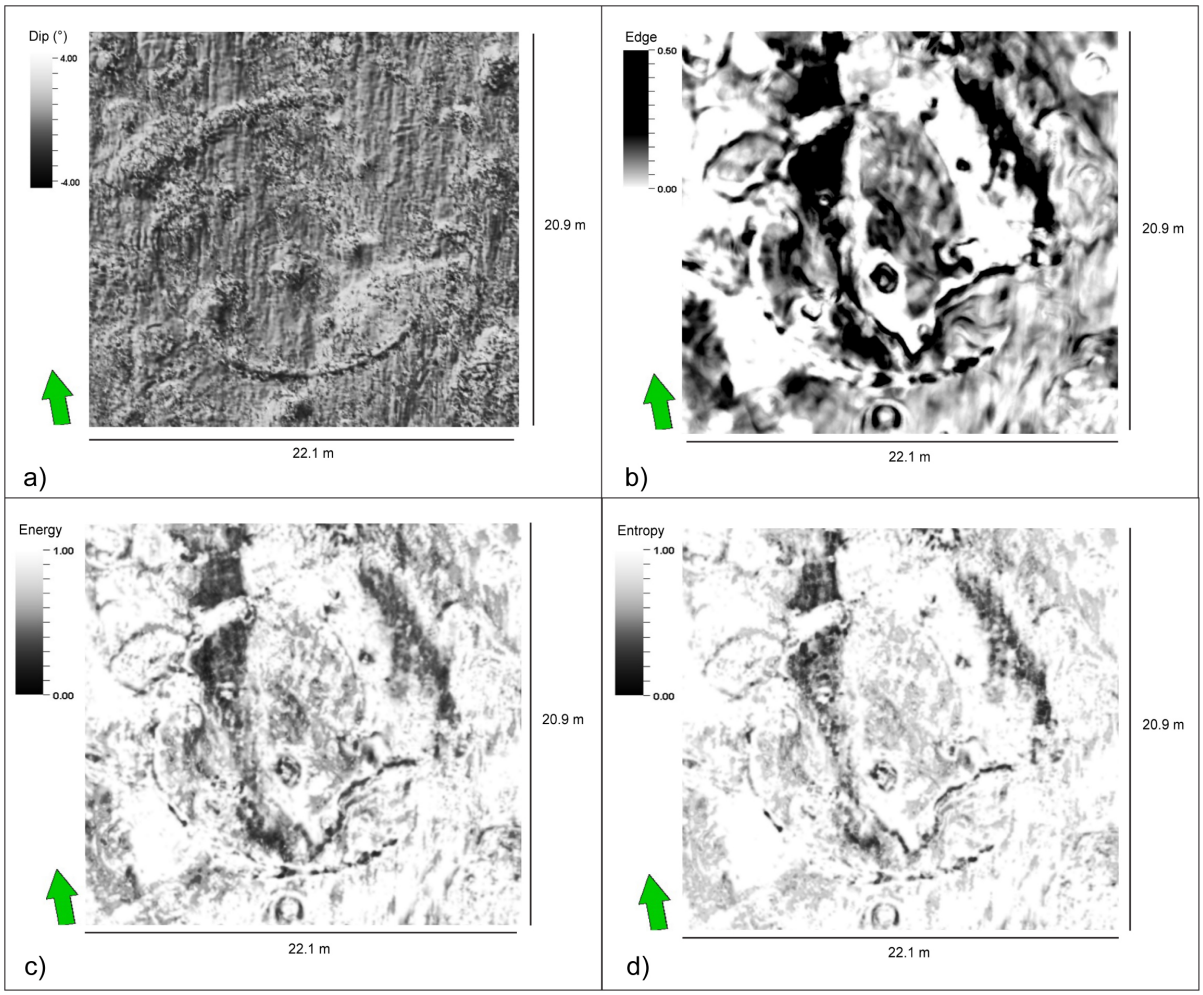

Figure 5.12: *Time slice at twt = -12 ns of burial mound. a) dip illumination with* $\theta = 130°$*, b) 3D edge enhancement, c) GLCM energy, and d) GLCM entropy.*

The instantaneous attributes were generated as for the other archaeological targets with a window of 83. The envelope (Figure 5.13a) shows some strong reflections from the ring ditch, but also displays strong reflections in the middle of the burial mound. The instantaneous phase and cosine of phase, shown in Figure 5.13b and 5.13c respectively, manages to image the ring ditch. On the other hand, the chaos attribute (Figure 5.13d) does not reveal any significant structure, similar to the results obtained for the other archaeological targets.

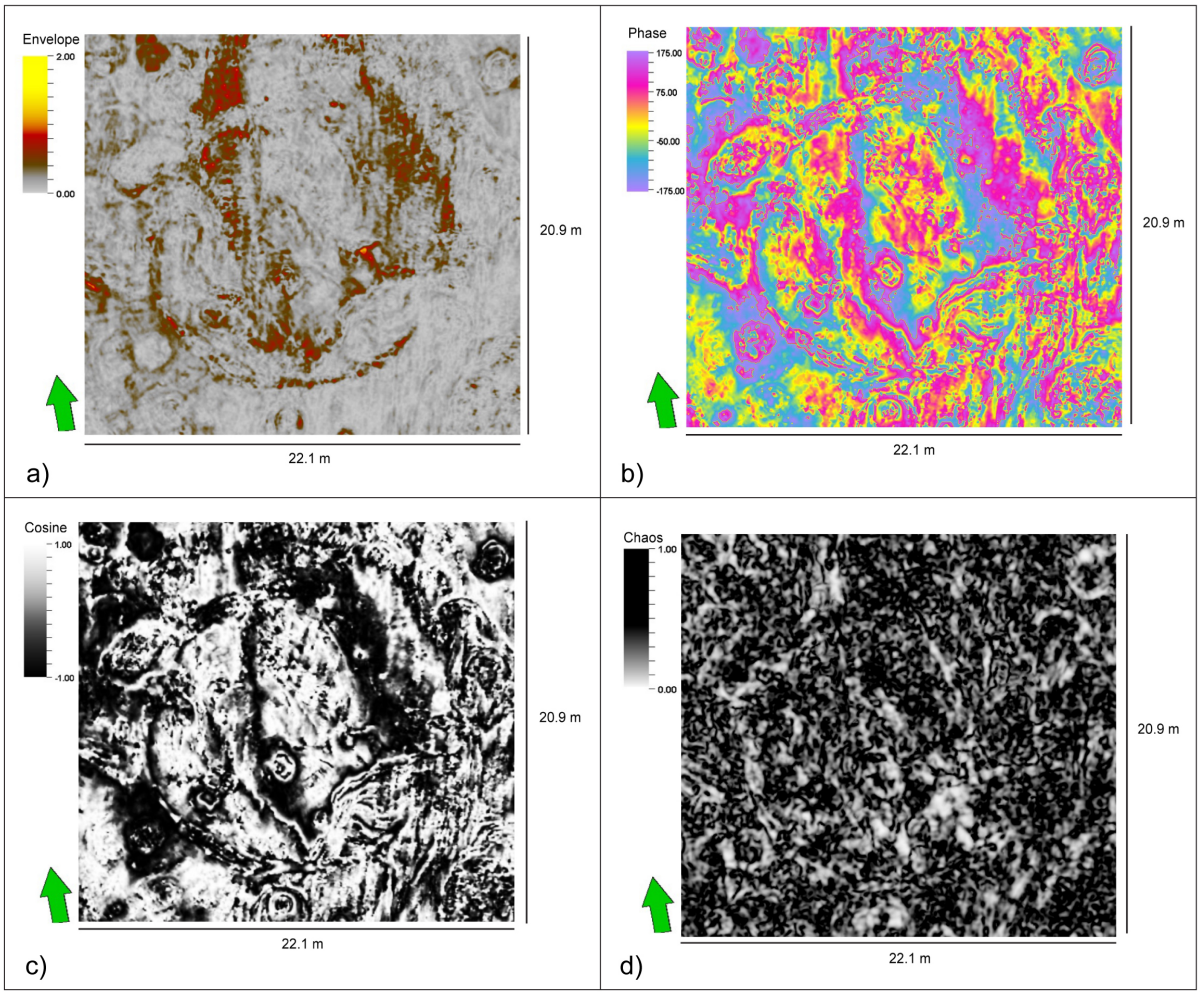

Figure 5.13: *Time slice at twt = -12 of burial mound. a) Envelope, b) Instantaneous phase, c) Cosine of phase, and d) Chaos.*

GPR profiles

In Figure 5.14, different attributes are shown on an inline section for the burial mound. The original reflection data in Figure 5.14a) clearly displays the ring ditch, but in the profile view, this feature is not as clearly defined as on the time slices. In comparison to the post holes and the cooking pits, neither the envelope (Figure 5.14b) nor the RMS amplitude (Figure 5.14c) yield the best results for the ring ditch. Due to the sharp visualizing of the cosine of phase (Figure 5.14d), in profile view, it works well. In contrast, the 3D edge enhancement (Figure 5.14e) and GLCM energy (Figure 5.14f) attributes are more smooth, and more similar to the original amplitude data, and both visualize the edge-like ring ditch.

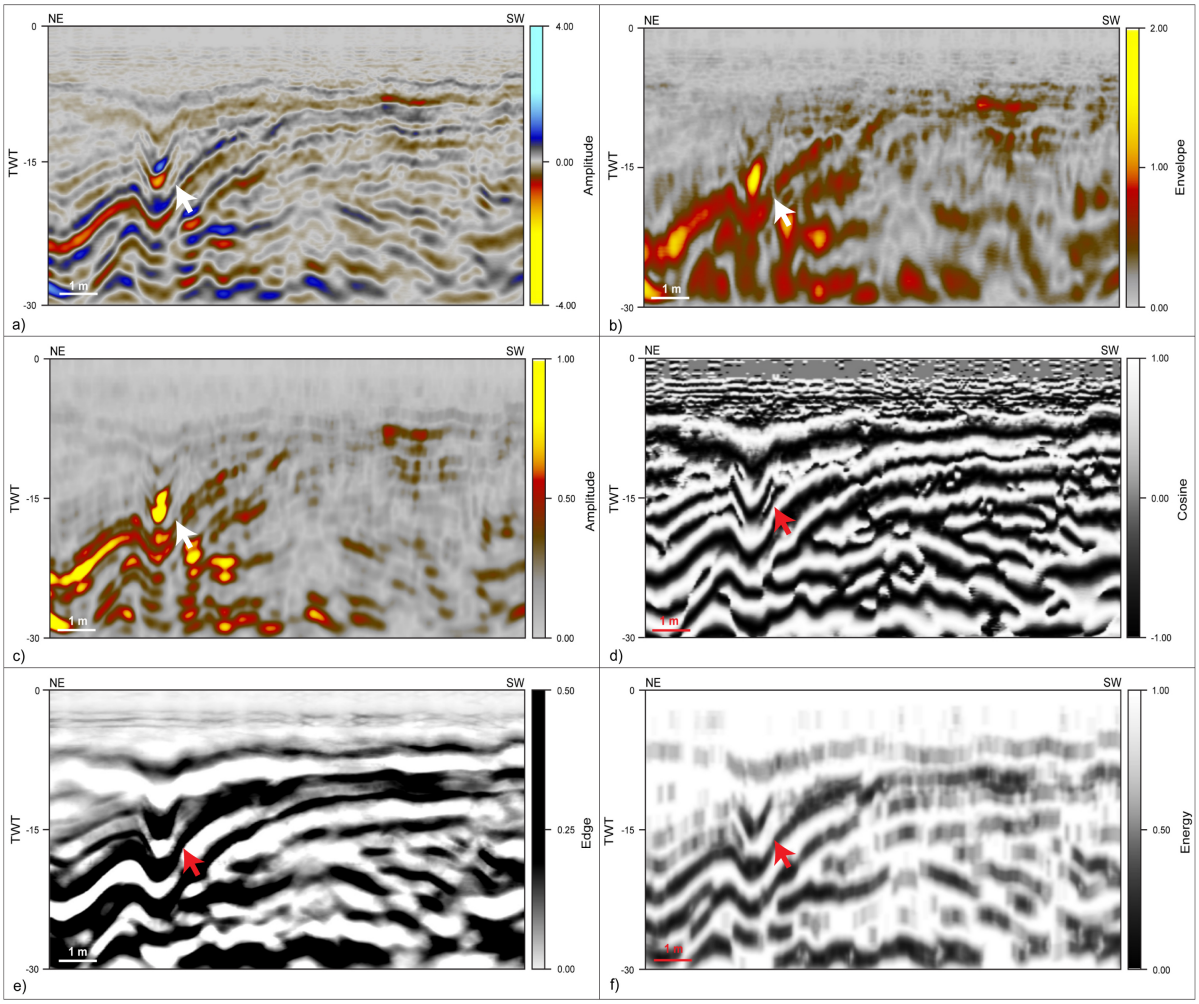

Figure 5.14: *Profile view of attributes for burial mound, where TWT is represented in ns. a) Original data, b) Envelope, c) RMS amplitude, d) Cosine of phase, e) 3D edge enhancement, and f) GLCM energy. White and red arrows show the signal response from the burial mound.*

5.4 RGB blending

Figure 5.15a show the results from RGB blending of the original data, RMS amplitude cube and the variance cube. The RGB blending enhances the image of the post holes by better separating the post holes from the surrounding soil. Similarly to the post holes, the original data, RMS amplitude cube, and the variance cube were employed as input for generating an RGB blending image of the cooking pits. The result is depicted in Figure 5.15c, and it significantly enhances the visibility of the cooking pits due to the strong signal of the cooking pit contours, as also demonstrated in the variance map, and effectively mapping different amplitude responses from the pits. The RGB blending of the burial mound, shown in Figure 5.15e, was generated with the same attributes as for the post holes and cooking pits. The RGB blending enhance the image of the burial mound by emphasizing the ring ditch around it.

The RGB blending images were generated using Generalized Spectral Decomposition (GSD) with a correlation algorithm. The correlation algorithm measures the similarity between the constructed wavelet and each trace in the data. This wavelet is constructed by specifying a frequency value, the number of cycles, and phase. The GSD was computed three times with different frequencies, selected based on the bandwidth, before applying RGB blending. This process was carried out for all three target areas, as depicted in Figure 5.15. The method produced good results for the cooking pits and the burial mound (Figure 5.15d and 5.15f respectively), and to some extent for the post holes (Figure 5.15b), although the post holes are not as clearly visible as the cooking pits and the burial mound. In the figure, white areas represent regions with strong amplitudes for all the frequencies, while areas with color correspond to weaker amplitude.

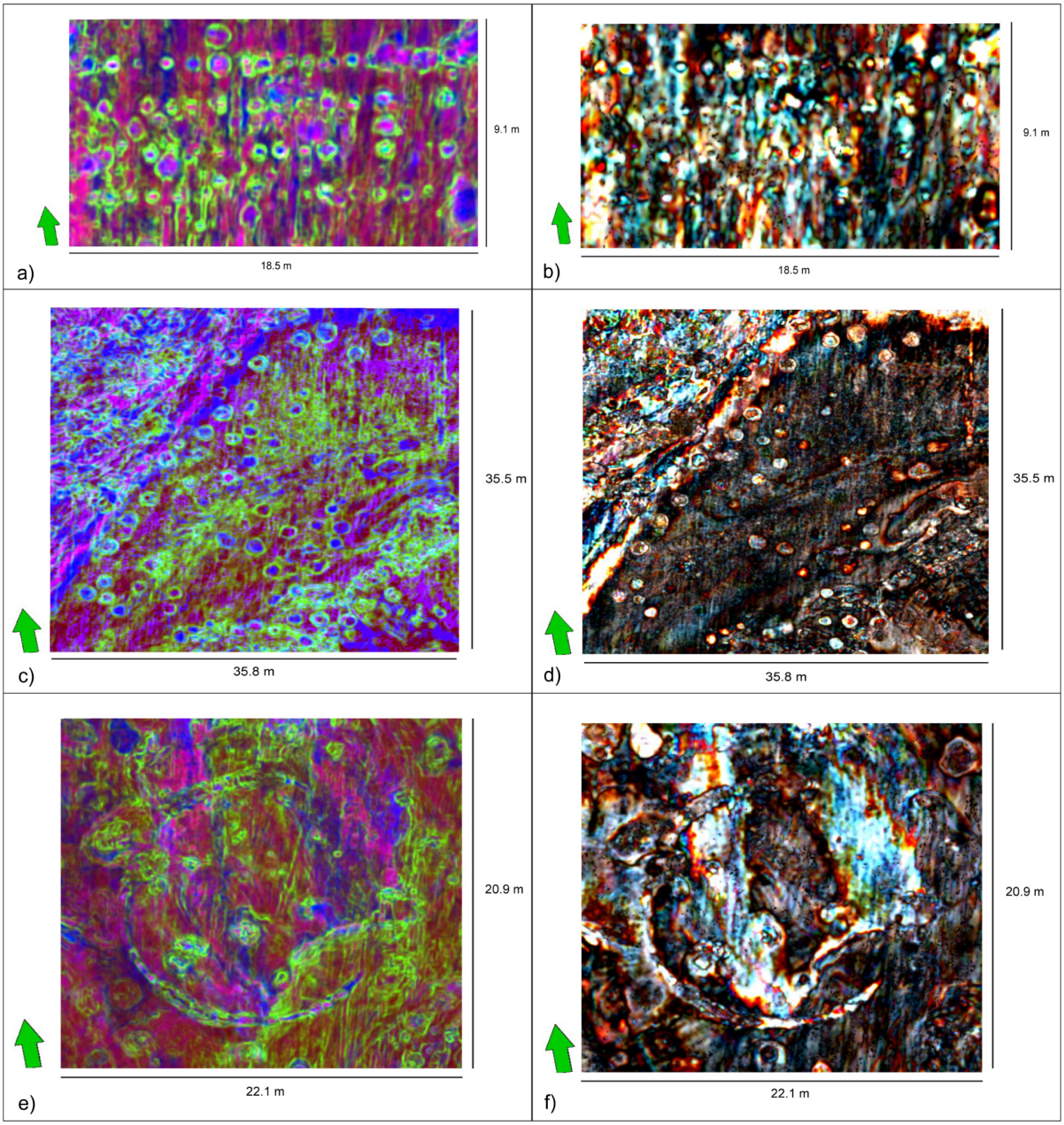

Figure 5.15: *The figures to the left display RGB blending with a mix of attributes, a) post holes, c) cooking pits, and e) burial mound. The figures to the right display RGB blending with generalized spectral decomposition with red corresponding to a 200-MHz frequency, green 300-MHz frequency, and blue 400-MHz frequency. b) post holes, d) cooking pits, and e) burial mound*

5.5 Horizon interpretation

Due to the nature of GPR data, which often lacks strong and continuous reflections, only one horizon have been interpreted over a small area (1900 m^2) around the previous longhouse. This horizon was interpreted on the structurally smoothed cube with decreased seed confidence, and was selected over the post holes to see if this could extract more

information from the data. The horizon was interpreted using 2D auto tracking, which use, seed points as guidance. The surface horizon is shown in Figure 5.16.

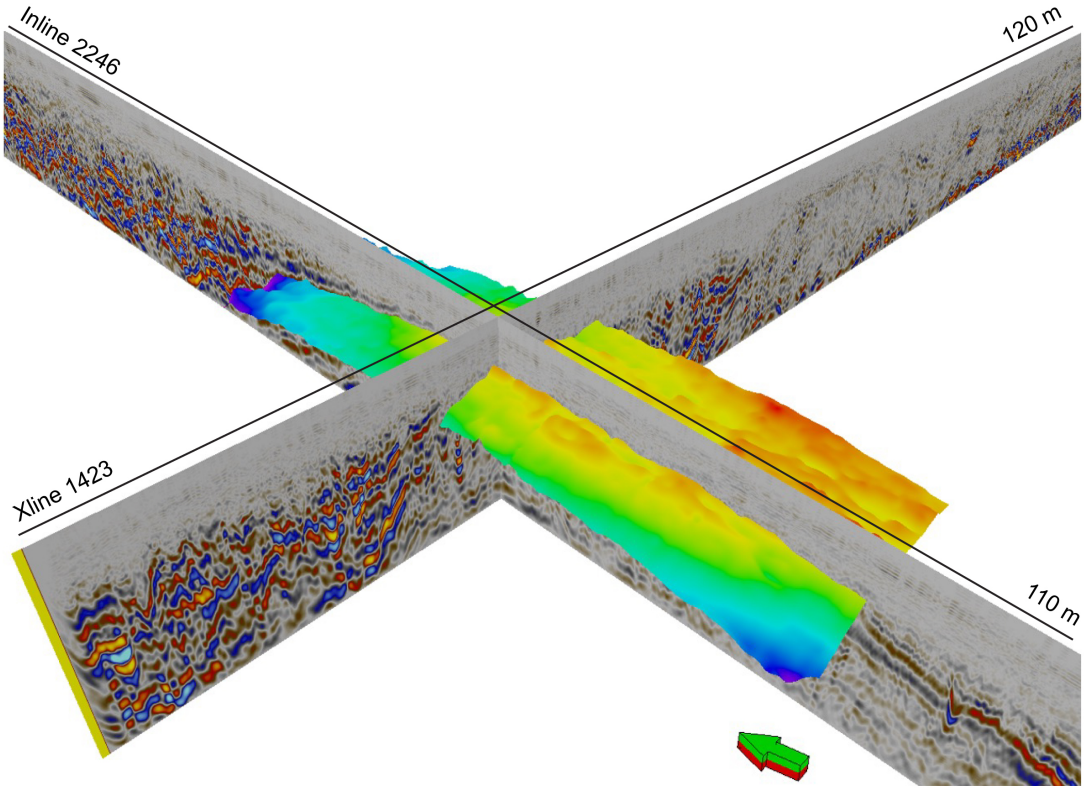

Figure 5.16: *TWT surface over post holes displayed with inline and xline.*

Three surface attributes were computed with a time window of 10-ns below the horizon, as shown in Figure 5.17. The TWT surface displays the elevation of the interpreted horizon, with the longhouse located in the middle of the horizon. The RMS amplitude surface effectively highlights the strong response from the post holes, which differs from the surrounding transparent soil displayed as gray in Figure 5.17b). The maximum amplitude surface, on the other hand, does not significantly improve the visualization of the post holes, but it does manage to some extent to display some of them. The maximum amplitudes are displayed as blue/green, while the purple area represents low amplitude. The average envelope surface, like the maximum amplitude, does not enhance the imaging of the post holes.

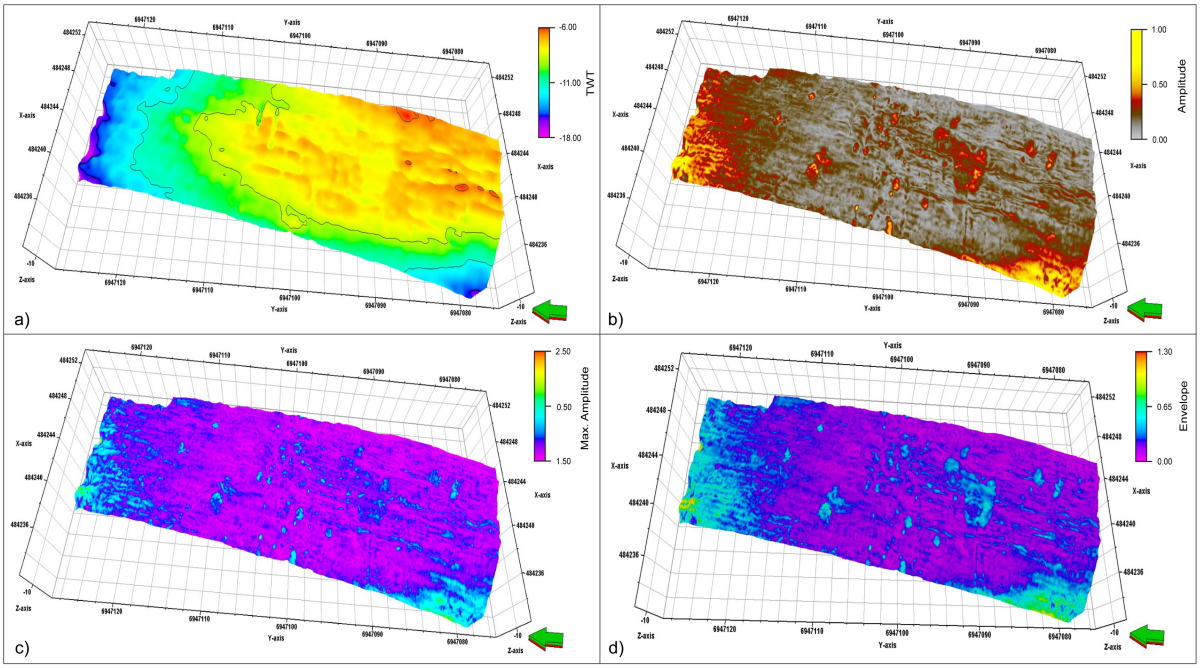

Figure 5.17: *Surface horizon interpreted over the previous longhouse. a) Time-depth surface, b) RMS amplitude computed over a 10 ns window, c) Maximum amplitude, d) Average envelope.*

In this chapter, I have presented the results obtained from this study. The outcomes of the various attributes are generally consistent with the different archaeological structures, with some variations, as will be discussed further. Certain results have been showcased based on their distinct characterization and visualization, while others were selected with the expectation of producing favorable outcomes but ultimately did not meet those expectations.

Chapter 6

Discussion

The primary objective of this thesis has been to enhance the visualization of archaeological features for easier interpretation, through the application of seismic attributes to GPR data. In this chapter, I will delve into the results of the attributes that have been tested and explore whether some of these attributes can be applicable to archaeological structures beyond the scope of this thesis. This study has revealed that certain attributes, which are not typically employed in archaeological GPR analysis, have the potential to improve the visualization of specific archaeological features.

6.1 Tested attributes

To the best of my knowledge, there have been only a limited number of research papers published on GPR attribute analysis for archaeological prospecting, with notable examples including Zhao et al. (2013), Zhao et al. (2015), and Zhao et al. (2016). These studies primarily focused on archaeological sites with prehistoric villages, examining the foundations of buildings. However, when it comes to circular structures like those found at Løykja, there has been relatively less studies regarding these structures. While the use of attributes for GPR analysis in archaeology has yet to become a standard practice, there is ongoing progress within this field.

A recent article by Trinks and Hinterleitner (2020) suggests that the coherence attribute offers valuable insights into archaeological features. Furthermore, the article indicates that other attributes commonly employed in seismic analysis hold the potential to enhance GPR data imaging, paving the way for more advanced and effective archaeological

investigations.

6.1.1 Variance

As exemplified by Trinks and Hinterleitner (2020), the coherence attribute has shown promising results in the context of GPR for archaeological prospective. In the field of seismic exploration, the coherence attribute has achieved state-of-the-art status, and it is consistently generated in nearly all cases, almost regardless of the type of geological structure being studied (Chopra and Marfurt, 2007, 2023; Pigott et al., 2013). Consequently, the coherence attribute was one of the first attributes computed from the Løykja data. In this study, a variance-coherence-based attribute has been employed. The results derived from the variance attribute, as illustrated in Figures 5.1c, 5.6c, and 5.11c, demonstrate an enhanced visualization of the archaeological structures. However, in the case of the post holes and burial mound, the influence of the acquisition footprint and surrounding geology is noticeable.

It is worth noting that the number of traces, referred to as the filter length, differ among the various archaeological structures, as does the vertical smoothing applied. Using a larger number of traces will increase the variance between traces, potentially resulting in a less informative image. A suggestion for optimal performance is to use a relatively small filter length, around 3, for both inline and xline directions. Smoothing played a crucial role, and large values were found to be necessary for all three structures. This indicates that the variance attribute detects noise, which must be smoothed out. In the seismic field, commonly used vertical smoothing values are around 15 (Aqrawi and Boe, 2011), but for GPR data, significantly larger values are required to effectively extract meaningful information. Especially in regards of the post holes, a large vertical smoothing was necessary.

6.1.2 Amplitude attributes

The envelope attribute is a widely used attribute in GPR for archaeological prospecting (Trinks et al., 2018; Manataki et al., 2021). In seismic exploration, this attribute has a long history of use but has gradually been replaced by RMS amplitude over the past decades. As illustrated in Figure 6.1a, 6.1c, and 6.1e, RMS amplitude works well for detecting post holes and cooking pits, which are characterized by strong amplitudes. However, in the context of the burial mound, RMS amplitude does not effectively enhance the visualization

of the ring ditch when compared to the variance map. Similarly, the envelope attribute produces results similar to RMS amplitude, as evident in Figure 6.1b, 6.1d, and 6.1f, where only high amplitudes are displayed, leaving the background transparent. In cases, where archaeological structures might appear as small structures, such as post holes, the use of RMS amplitude may be more fitting, due to a more resolved result, where as the envelope produce a smoother result.

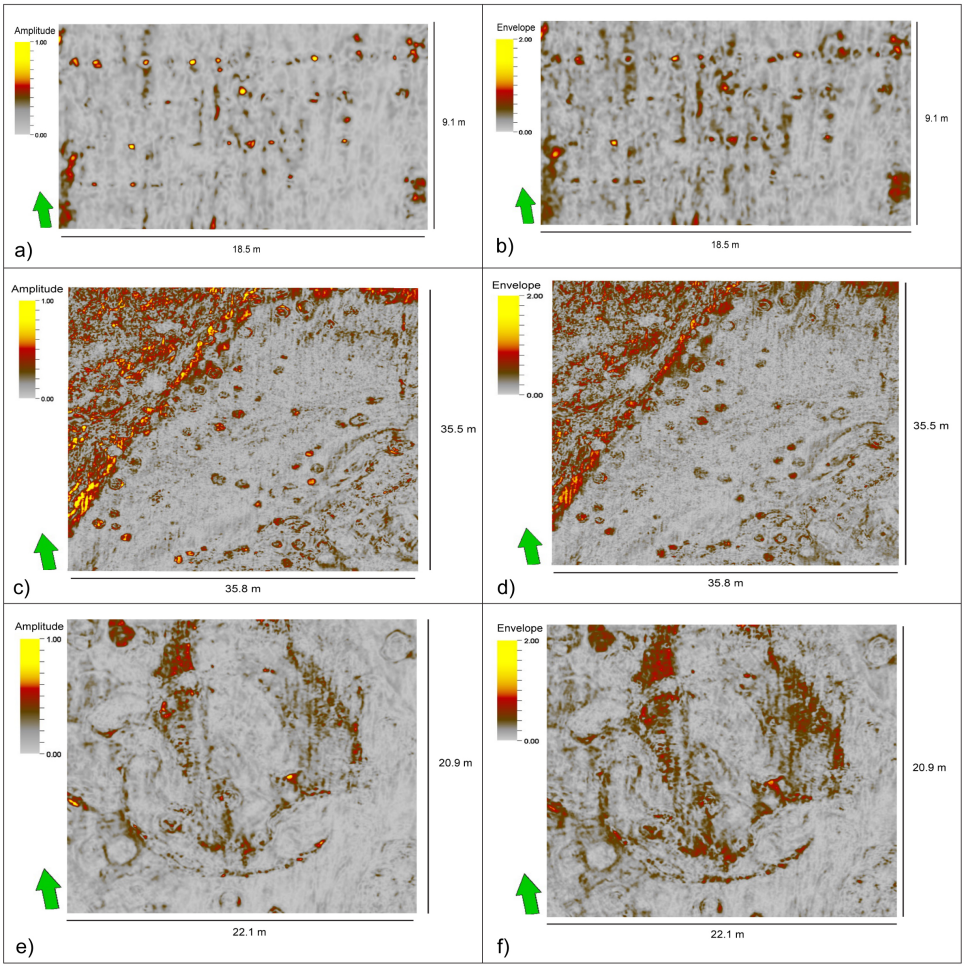

Figure 6.1: *The figures to the right are RMS amplitude on the three structures. The figures to the left are Envelope on the three structures.*

Despite the differences between RMS amplitude and envelope attributes, their primary purpose is to highlight strong amplitudes. Based on the results from this study, I would recommend using RMS amplitude for its advantages. However, considering that these two attributes yield more or less the same results, choosing just one of them should be sufficient. As discussed by Barnes (2006), there is a multitude of attributes to choose from, and many of them produce similar outcomes, so selecting one based on amplitude strength should be suitable.

6.1.3 Dip illumination

The dip illumination attribute was specifically tested in this study due to the structural characteristics studied in this thesis, primarily focusing on enhancing the visualization of cooking pits, where Figure 5.7a displays the results obtained from this attribute. Regarding the cooking pits, the dip illumination effectively outlines their curvature, but is dependent of the illumination angle used. As shown in Figure 6.2, an illumination angle of 60° provides a better visualization of the cooking pits structure, and the quantity of cooking pits is more visible. However, an illumination angle of 90° mitigates the influence of the acquisition footprint. Notably, illumination angles below 60° or above 90° tend to obscure the distinctiveness of the cooking pits structure.

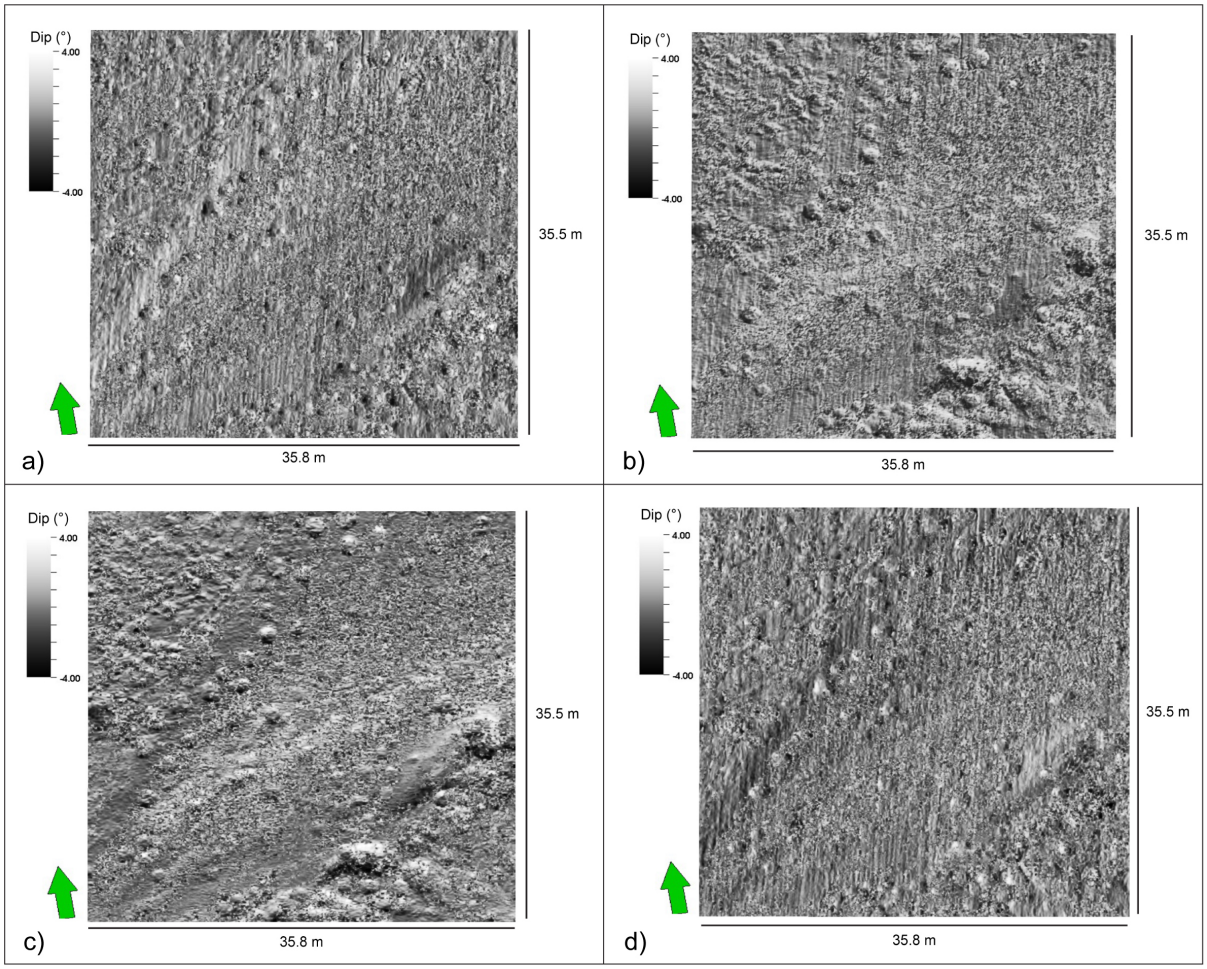

Figure 6.2: *Dip illumination with various illumination angles of the cooking pits. Time-slice at twt = -12 ns. a) $\theta = 0°$, b) $\theta = 60°$, c) $\theta = 90°$, and d) $\theta = 180°$*

The dip illumination attribute did not significantly enhance the image of the post holes, possibly due to their small size, which makes them more challenging to image using this attribute. However, it yielded notable results for the ring ditch around the burial mound.

The choice of illumination angle is crucial, as demonstrated in Figure 6.3. In Figure 5.12a, I presented the dip illumination attribute with an illumination angle of $\theta = 130°$, which effectively enhanced the structure of the foot ditch.

It is essential to note that the illumination angle not only affects the structure but also has an impact on the acquisition footprint, as illustrated in Figure 6.3. When using an illumination angle of $\theta = 0°$ (Figure 6.3a) or $\theta = 180°$ (Figure 6.3f) , the illumination is perpendicular to the acquisition footprint, leading to the illumination of the footprint itself. This is typically not of interest. However, with an illumination angle of $\theta = 90°$ (Figure 6.3d), the illumination is parallel to the footprint, resulting in a muting or dimming of the footprint effect, also present for the cooking pits. This, in turn, enhances the visibility of the ring ditch structure by reducing the noise effect of the footprint.

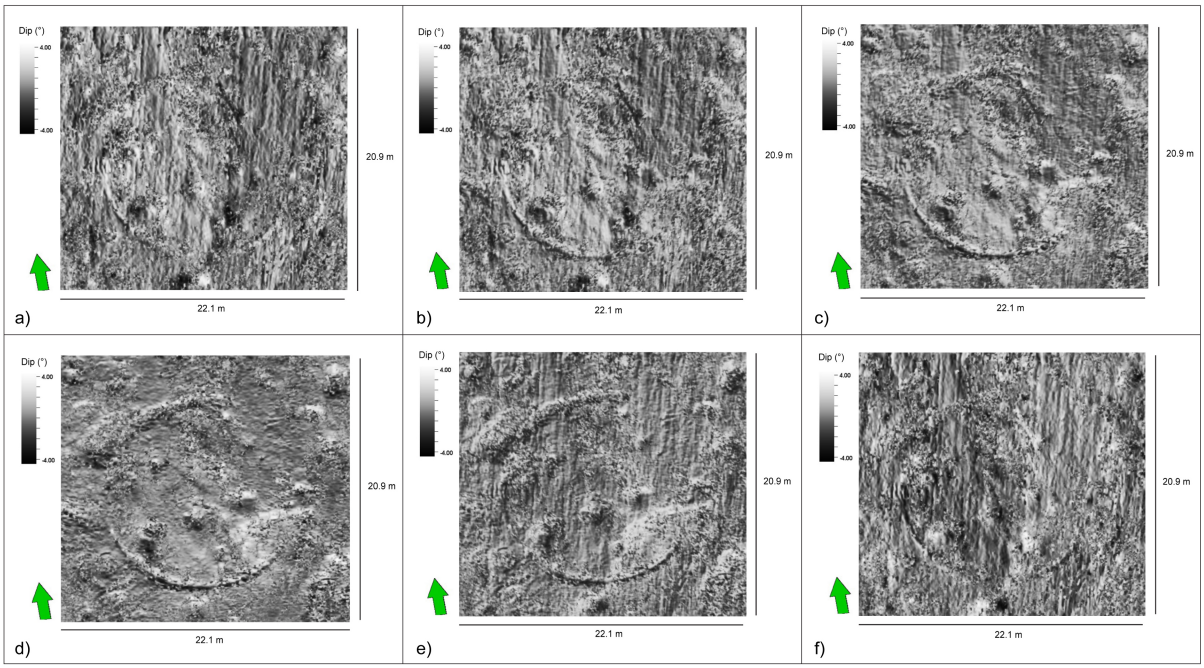

Figure 6.3: *Dip illumination with various illumination angles of the burial mound. Time slice at twt = -12 ns. a) $\theta = 0°$, b) $\theta = 30°$, c) $\theta = 60°$, d) $\theta = 90°$, e) $\theta = 130°$, f) $\theta = 180°$*

6.1.4 Chaos and edge enhancement

A study by Forte et al. (2021) suggested using the chaos attribute for better visualization of archaeological structures. Despite achieving good results in their study, the application of the chaos attribute in this research (see Figures 5.3d, 5.8d, and 5.13d) did not yield as significant outcomes as anticipated. The chaos attribute reflects the degree of chaos or randomness in the data. Although typically not a focal point in GPR applications, it

was worth exploring based on the findings of Forte et al. (2021) to assess its potential in enhancing certain structures or providing new information.

As for the 3D edge enhancement, this attribute is designed for larger structures, such as extensive fault zones, where smaller features may be smoothed away. This effect is evident in Figure 5.2b, where some of the post holes are not clearly visible. This could lead to imprecise interpretation. Regarding the cooking pits (see Figure 5.7b), the edge enhancement manages to visualize the pits, but the dimensions of the cooking pits appear smaller compared to the images produced by the variance and RMS amplitude attributes. Furthermore, in the case of the burial mound (see Figure 5.12b), the attribute effectively visualizes the ring ditch. One possible explanation for this success may be the resemblance between the structure of the ring ditch and fault structures in seismic data. Comparing edge enhancement to the variance attribute, it is evident that the variance attribute produces a sharper and more informative image of the structures. This enhanced clarity facilitates easier interpretation of the archaeological feature.

6.1.5 Instantaneous attributes and GLCM

The instantaneous attributes are often used for geological interpretation in seismic. In the case for archaeological structures, the instantaneous phase and cosine of phase display sharp images. This is proven beneficial for burial mounds, and to some extent the cooking pits (see Figures 5.8b and 5.8c, and Figure 5.14d). In regards of the post holes, the images displayed noisy results, which was hard to interpret any structures (see Figures 5.3b and c). It is worth noting, that both instantaneous phase and cosine of phase do image more or less the same result, so, as discussed by Barnes (2006), choosing one of these two should be efficient. In regards of the GLMCs attributes, energy and entropy, these attributes manages to distinguish the archaeological features by their shape and structure.

6.1.6 Mixing attributes

As previously mentioned (refer to Section 3.1.6), a common technique for visualising attributes involves combining a grey-scale attribute with a color-scaled attribute, typically blending variance with RMS amplitude. This approach has been applied in this thesis, as shown in Figures 5.1d, 5.6d, and 5.11d. The blending of variance and RMS amplitude renders both structure and amplitude response more discernible, aiding in the interpretation of various features. In seismic, this method is commonly employed in reservoir

characterization, where amplitudes relate to fluids and variance map describe the structural setting of the reservoir. While blending RMS amplitude with variance suits such purposes, for archaeological features, the variance map alone might be sufficient, even though the combined attributes provide clear images of the structures.

The combined use of RGB blending and spectral decomposition has gained popularity in seismic data analysis, particularly for the detection and delineation of faults cahnnels (Chopra and Marfurt, 2007; Henderson et al., 2008; Othman et al., 2016). This study follows this trend, generating RGB blending images with different attributes and employing spectral decomposition.

The RGB blending using the original data, with RMS amplitude and variance as inputs, is depicted in Figures 5.15. These images showcase promising outcomes, enhancing the visualization of all three structures. This method demonstrates efficacy by combining attributes, particularly utilizing RMS amplitude and variance as inputs due to their distinct characteristics. As previously discussed, RMS amplitude exhibits reflection strength, while variance enhances the visualization of structural contours. By blending these two attributes, the resulting visualization presents both strong amplitudes and structural contours. In this thesis, the original data was incorporated into the RGB blending due to its simplicity and contained information. Alternatively, attributes like dip illumination for the burial mound or GLCM energy for the post holes could have been employed, potentially resulting in promising outcomes.

In the case of RGB blending with spectral decomposition, the selected frequencies are derived from the frequency spectrum, by employing the generalized spectral decomposition attribute in Petrel. More advanced methods in regards of spectral decomposition could potentially yield more accurate results, such as Discrete Fourier Transform or Continuous Wavelet Transform (Othman et al., 2016). Despite its simplicity, the generalized spectral decomposition proved effective. The results, depicted in Figure 5.15, exhibited optimal outcomes for the cooking pits. However, for both the post holes and burial mound, the structures are visible but accompanied by noise, affecting image quality. The transparent background is represented as a blackish hue, indicating the absence of response at those frequencies. The application of switching frequencies could enhance the RGB blending with spectral decomposition, and these techniques are readily implementable in various interpretation software (Giroldi and Alegria, 2005).

6.1.7 Multi-attribute

The multi-attribute method was tested to see if it was possible for machine learning to detect predefined features, such as cooking pits (Figure 5.10). The chosen attributes for this training model were selected based on amplitude and structure, so the model was generated with the original data, RMS amplitude, and variance. It is worth mentioning that due to computation time, there was only computed one training model for the cooking pits for the aim of using this model to detect cooking pits located at the survey site. Using the original data, RMS amplitude, and variance, the neural network managed to detect and classify the cooking pits.

Despite the limited success in this study, machine learning has the potential to be a powerful tool in GPR for archaeological prospective. It can automate the extraction of valuable information from GPR data, particularly for tasks like cooking pit detection and counting, and potentially saving time that would otherwise be spent on manual analysis. However, for machine learning to be effective in archaeological applications of GPR, the availability of sufficient training data is crucial.

6.2 Summary of tested attributes

Selecting the most suitable seismic attributes from the multitude available for data analysis can be a challenging task. The Table 6.1 provides a qualitative summary of the attributes generated in this study and their respective outcomes for each archaeological structure. The classifications provided are specific to the dataset obtained from Løykja. It is essential to acknowledge that these classifications may not universally apply to all GPR datasets. Instead, they serve as an objective guideline for potentially applicable attributes on other GPR datasets, rather than finite result.

Table 6.1: *Summary table of attributes used in this study, with a guide to which attributes can enhance interpretation of archaeological structures. Instant. frequency refers to instantaneous frequency.*

Attribute	**Post holes**	**Cooking pits**	**Burial mounds**
3D edge enhancement	Fair	Good	Good
Chaos	Poor	Poor	Poor
Cosine of phase	Poor	Good	Good
Dip illumination	Poor	Good	Excellent
Envelope	Excellent	Excellent	Good
GLCM energy	Good	Fair	Good
GLCM entropy	Good	Fair	Good
Instant. frequency	Poor	Poor	Poor
Instantaneous phase	Poor	Good	Good
RMS amplitude	Excellent	Excellent	Good
Variance	Excellent	Excellent	Excellent

The summary provided in Table 6.1 underscores that attributes delivering positive outcomes for all three structures include envelope, RMS amplitude, and variance. Particularly, amplitude-based attributes, such as RMS amplitude and envelope, showcased promising results for the cooking pits and post holes. Conversely, structure attributes like variance and dip illumination exhibited more favorable outcomes for the burial mound.

In the context of the various attributes explored in this thesis, it is crucial to recognize that these attributes represent specific measurements derived from the data. Their effectiveness is contingent upon different parameters, such as smoothing, filter length, and window size. As highlighted by Forte et al. (2021), identifying the most suitable attributes for a particular survey can be challenging. However, the critical aspect often lies in the proper selection and adjustment of parameters during calculations, as demonstrated in Figure 6.4.

The significance of parameter selection is further illustrated by the dip illumination attribute (Figure 6.3). Initially, it exhibited sub-optimal performance, failing to detect any of the three structures. Nevertheless, a notable change occurred with the adjustment of a single parameter, leading to meaningful and significant results. This underscores the sensitivity of attribute performance to parameter settings.

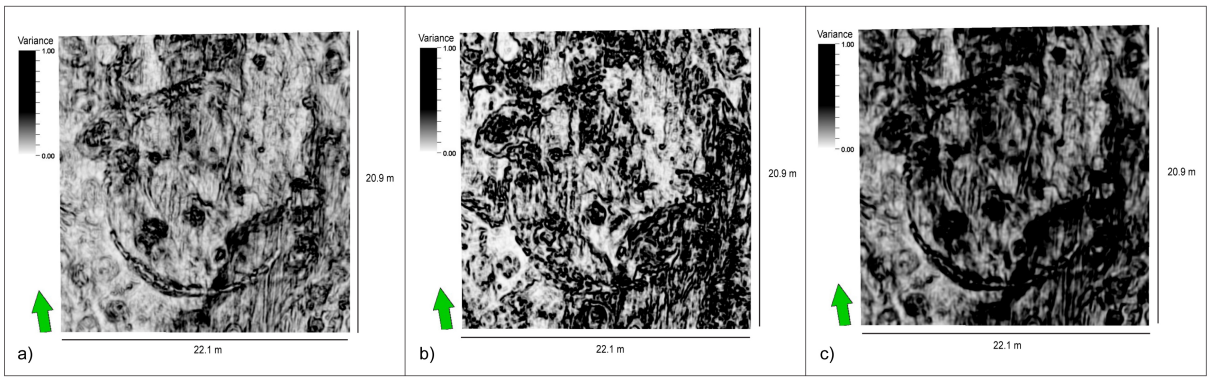

Figure 6.4: *Time slice at twt= -12 ns of burial mound. a) Filter length: 3x3 with vertical smoothing: 130. b) Filter length: 3x3 with vertical smoothing: 15. c) Filter length: 5x5 with vertical smoothing: 130.*

Additionally, the choice of a suitable color-bar can significantly impact the visualization of various attributes. For instance, opting for a black-grey-white color bar proves effective for depicting variance. When utilizing attributes that demonstrate reflection strength, like RMS amplitude and envelope, employing a color bar with a spectrum of colors aids in enhancing the visualization of reflection strength.

6.2.1 Horizon interpretation

Horizon interpretation can be challenging, especially when dealing with weak and discontinuous reflectors. However, it is a valuable process for extracting important information from the data. In the context of the Løykja data, the varying horizon depths, as shown in Figure 5.16, can provide insights into potential erosion processes that might have occurred. Such erosion could have had an impact on cultural targets buried beneath the ground. It is also important to note that the Løykja data was collected on cultivated land, and this agricultural activity could have affected the soil and the preservation of archaeological targets.

6.3 Data

While this study did not explicitly include data processing, it is crucial to acknowledge its significance for subsequent analysis. The chosen data processing methods can significantly influence the final results and, consequently, the attribute extraction outcomes. Migration, as a key processing step, plays a vital role in obtaining the most accurate subsurface structure images. Improper migration, either over-migrated or under-migrated, can lead

to misinterpretations. As illustrated in Figure 6.5, migration has a substantial impact on the imaging of post holes. Additionally, the resolution of the data is a critical factor, especially for detecting small structures like post holes.

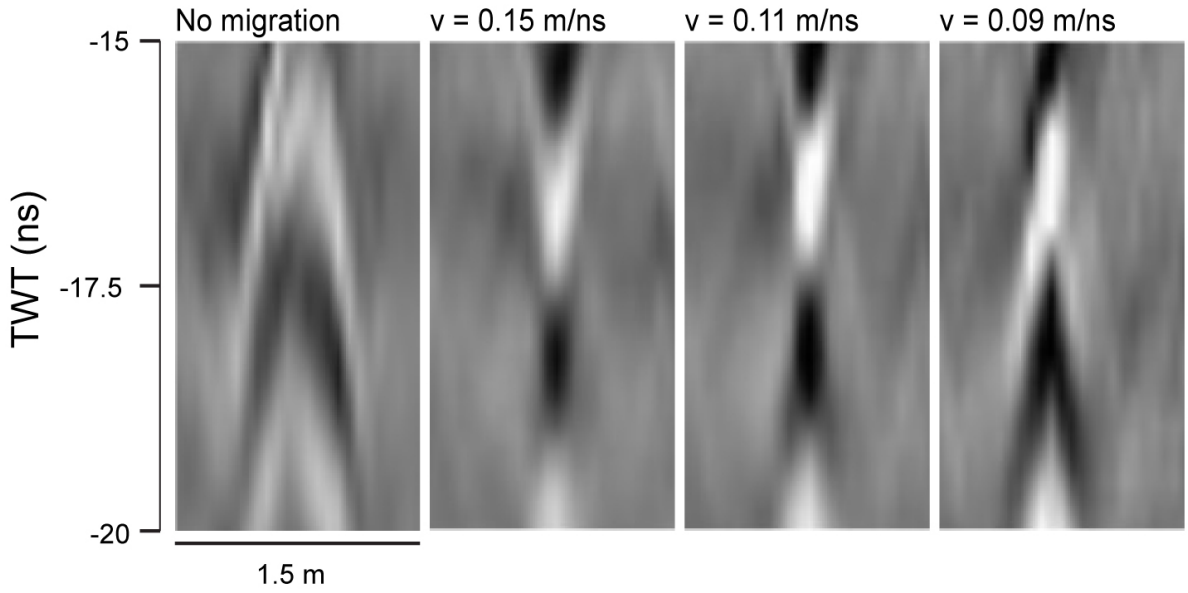

Figure 6.5: *Shows the effect of migration on a post hole, taken from Examiner.*

6.4 Geology

As mentioned previously (see Section 5.2), the response of archaeological structures is dependent on the surrounding soil properties. The three structures studied in this thesis are situated in homogeneous soil, resulting in a robust response from the structures. Locating and interpreting archaeological structures in more chaotic subsurface conditions may pose additional challenges. This was investigated in the study area with glacifluvial deposits, where the GPR pattern is more chaotic. The attributes discussed in this thesis were applied to this area, yielding less pronounced results. Among the attributes tested, RMS amplitude and, to some extent, the variance attribute provided the most informative outcomes, as depicted in figures 6.6b and 6.6c. The variance attribute also reveals geological features, which in this case, makes the image more noisy. It is also essential to acknowledge that while the variance map might reveal certain pits, distinguishing features as pits solely based on this map could lead to potential misinterpretation. Regarding the RMS amplitude map, the pits are displayed as low-amplitude structures due to the strong amplitudes from the surrounding soil.

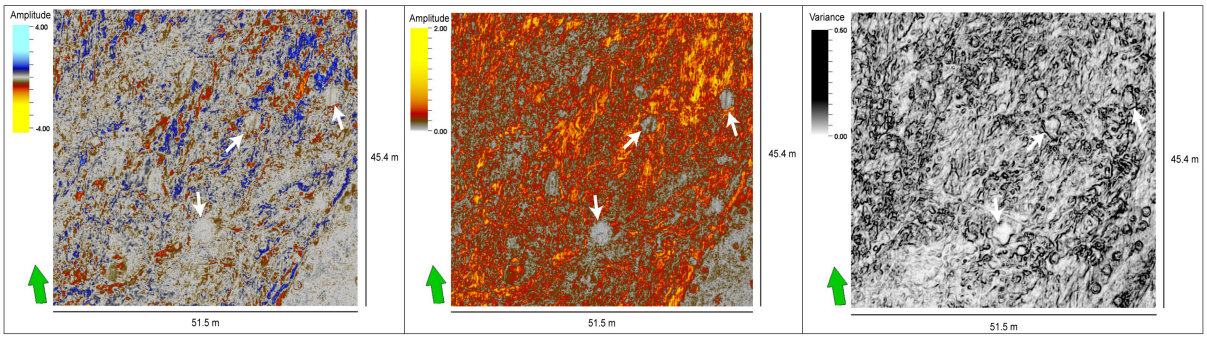

Figure 6.6: *Time-slice at t = 12 ns where the white arrows are interpreted as pits. a) Original data, b) RMS amplitude, c) Variance.*

6.5 Limitations and uncertainties

In this thesis, the extraction of attributes was carried out using a commercial software program. However, due to competition and confidentiality among companies, access to attribute algorithms has been restricted. In Petrel, the software used for the study, certain parameters for various attributes lack clear definitions, posing limitations in the selection and understanding of these parameters. While literature provides equations and calculations for different attributes, detailed information about the algorithms employed for some attributes in Petrel remain limited.

The ease of attribute generation in Petrel can be both advantageous and overwhelming. The extensive range of available attributes may pose challenges, particularly in selecting the appropriate ones and determining the right parameters, as discussed earlier. Additionally, it is important to note that the attributes used in this study were originally developed for seismic data. While these attributes have shown enhanced results for GPR data, there may still be differences in their performance and applicability between the two types of data.

6.6 Attributes for other archaeological features

This thesis demonstrates that commonly used attributes in archaeological studies, such as RMS amplitude and variance, effectively highlight the three archaeological structures investigated here (see Figures 5.1, 5.6 and 5.11). While these attributes provide favorable results, other attributes, including dip illumination and, to some extent, 3D edge enhancement, also show promising outcomes. In terms of noise reduction, dip illumina-

tion and smoothing have shown promising results. Additionally, combining attributes and techniques like RGB blending can further enhance the imaging of archaeological structures. For structures like remains of wall segments, attributes commonly employed for fault detection, such as variance, edge enhancement, and cosine of phase, could prove beneficial.

Chapter 7

Conclusion

The aim of this thesis has been to explore seismic attributes, and their potential use in GPR analysis for archaeological prospective. The main archaeological structures in this thesis have been post holes from longhouses, cooking pits, and burial mounds. Several attributes, commonly used in seismic exploration, and reservoir characterisation, have been tested on the GPR data. The results and discussion presented have led to following conclusions:

- The workflow outlined in this thesis offers a method for extracting attributes and other information from GPR data.
- Attributes originally developed for seismic analysis can be directly applied to GPR analysis, effectively enhancing the imaging of archaeological structures.
- The study reveals that attributes such as RMS, envelope, and variance yield favorable results for all three archaeological structures. However, it is stated that by applying either RMS amplitude or envelope should be efficient.
- RGB blending with spectral decomposition shows promising results.
- The dip illumination attribute proves significant in visualizing the burial mound. The attribute's effectiveness is dependent on the choice of illumination angle, and selecting an angle parallel to the acquisition footprint aids in noise reduction.
- Multi-attribute has potential for automating detection of distinct structures, such as cooking pits.

7.1 Future Work

This thesis contributes to advancing GPR interpretation for archaeological prospects through the application of attributes originally designed for seismic analysis. While the study has yielded interesting results, there are opportunities for further enhancements in imaging archaeological structures. The attributes and algorithms employed in this thesis were initially designed for seismic analysis. Despite their seismic origin, these attributes demonstrated improved results when applied to GPR data, but it is crucial to recognize that material properties differ between seismic and GPR interpretations. Thus, developing and exploring seismic attributes adjusted for GPR properties may further enhance the interpretative capabilities. For instance, the development of an attribute considering EM impedance could be beneficial for GPR interpretation. In addition to this, exploring neural network methods could potentially reduce time-consuming work, such as counting the amount of cooking pits found in a large area.

Bibliography

Alaudah, Y., Michałowicz, P., Alfarraj, M., and AlRegib, G. (2019). A machine-learning benchmark for facies classification. *Interpretation*, 7(3):SE175–SE187.

Annan, A. (2003). *Ground Penetrating Radar: Principles, Procedures & Applications*. Sensors & Software Incorporated.

Aqrawi, A. A. and Boe, T. H. (2011). Improved fault segmentation using a dip guided and modified 3d sobel filter. In *SEG Technical Program Expanded Abstracts 2011*, pages 999–1003. Society of Exploration Geophysicists.

Araya-Polo, M., Dahlke, T., Frogner, C., Zhang, C., Poggio, T., and Hohl, D. (2017). Automated fault detection without seismic processing. *The Leading Edge*, 36(3):208–214.

Baker, G. S., Steeples, D. W., Schmeissner, C., Pavlovic, M., and Plumb, R. (2001). Near-surface imaging using coincident seismic and gpr data. *Geophysical Research Letters*, 28(4):627–630.

Barnes, A. (2006). Too many seismic attributes. *CSEG Recorder*, 31(3):40–45.

Barnes, A. E. (2003). Shaded relief seismic attribute. *Geophysics*, 68(4):1281–1285.

Barnes, A. E. (2007). A tutorial on complex seismic trace analysis. *Geophysics*, 72(6):W33–W43.

Boddice, D. (2015). *Changing geophysical contrast between archaeological features and surrounding soil*. PhD thesis, University of Birmingham.

Chopra, S. and Marfurt, K. J. (2005). Seismic attributes—a historical perspective. *Geophysics*, 70(5):3SO–28SO.

Chopra, S. and Marfurt, K. J. (2007). *Seismic attributes for prospect identification and reservoir characterization*. Society of Exploration Geophysicists and European Association of Geoscientists and Engineers.

Chopra, S. and Marfurt, K. J. (2008). Emerging and future trends in seismic attributes.

The Leading Edge, 27(3):298–318.

Chopra, S. and Marfurt, K. J. (2023). Pockmarks and their seismic attribute signatures. *AAPG Explorer*.

Conyers, L. B. (2007). Ground-penetrating radar for archaeological mapping. *Remote sensing in archaeology*, pages 329–344.

Conyers, L. B. (2016). *Interpreting ground-penetrating radar for archaeology*. Routledge.

Davis, J. L. and ANNAN, A. P. (1989). Ground-penetrating radar for high-resolution mapping of soil and rock stratigraphy 1. *Geophysical prospecting*, 37(5):531–551.

Dewett, D. T., Pigott, J. D., and Marfurt, K. J. (2021). A review of seismic attribute taxonomies, discussion of their historical use, and presentation of a seismic attribute communication framework using data analysis concepts. *Interpretation*, 9(3):B39–B64.

Eide, E., Linford, N., Persico, R., and Sala, J. (2019). Advanced sfcw gpr systems. In *Innovation in Near-Surface Geophysics*, pages 253–285. Elsevier.

Engevik, A. (2018). Gravhaug. `https://snl.no/gravhaug`. Accessed: 2023-05-26.

Fisher, E., McMechan, G. A., Annan, A. P., and Cosway, S. W. (1992). Examples of reverse-time migration of single-channel, ground-penetrating radar profiles. *Geophysics*, 57(4):577–586.

Forte, E., Mocnik, A., Basso, P., Casagrande, G., Martinucci, D., Pillon, S., Possamai, M., and Zambrini, R. (2021). Optimised extraction of archaeological features from full 3-d gpr data. *Applied Sciences*, 11(18):8517.

Forte, E., Pipan, M., Casabianca, D., Di Cuia, R., and Riva, A. (2012). Imaging and characterization of a carbonate hydrocarbon reservoir analogue using gpr attributes. *Journal of Applied Geophysics*, 81:76–87.

Fredriksen, C. and Stamnes, A. (2019). Geofysiske undersøkelser og sosialt metallsøk på løykja, gnr. 41/6, sunndal kommune, møre og romsdal. *Arkeologisk rapport, NTNU Vitenskapsmuseet, Trondheim*.

Gabler, M., Trinks, I., Nau, E., Hinterleitner, A., Paasche, K., Gustavsen, L., Kristiansen, M., Tonning, C., Schneidhofer, P., Kucera, M., et al. (2019). Archaeological prospection with motorised multichannel ground-penetrating radar arrays on snow-covered areas in norway. *Remote Sensing*, 11(21):2485.

Giroldi, L. and Alegria, F. (2005). Using spectral decomposition to identify and characterize glacial valleys and fluvial channels within the carboniferous section in bolivia. *The Leading Edge*, 24(11):1152–1159.

Grasmueck, M. (1996). 3-d ground-penetrating radar applied to fracture imaging in gneiss. *Geophysics*, 61(4):1050–1064.

Guéguen, Y. and Palciauskas, V. (1994). *Introduction to the Physics of Rocks*. Princeton University Press.

Gustavsen, L., Cannell, R. J., Nau, E., Tonning, C., Trinks, I., Kristiansen, M., Gabler, M., Paasche, K., Gansum, T., Hinterleitner, A., et al. (2018). Archaeological prospection of a specialized cooking-pit site at lunde in vestfold, norway. *Archaeological Prospection*, 25(1):17–31.

Gustavsen, L., Stamnes, A. A., Fretheim, S. E., Gjerpe, L. E., and Nau, E. (2020). The effectiveness of large-scale, high-resolution ground-penetrating radar surveys and trial trenching for archaeological site evaluations—a comparative study from two sites in norway. *Remote Sensing*, 12(9):1408.

Henderson, J., Purves, S. J., Fisher, G., and Leppard, C. (2008). Delineation of geological elements from rgb color blending of seismic attribute volumes. *The Leading Edge*, 27(3):342–350.

Hossain, S. (2020). Application of seismic attribute analysis in fluvial seismic geomorphology. *Journal of Petroleum Exploration and Production Technology*, 10:1009–1019.

Høgskolen i Østfold, Institutt for Energiteknikk, N. M. L. V. f. (2020). Gjellestad story. `https://www.gjellestadstory.no/`. Accessed: 2023-10-05.

Jol, H. M. (2008). *Ground penetrating radar theory and applications*. Elsevier.

Kontur (2022). Technology. `https://kontur.tech/technology`. Accessed: 2023-05-29.

Leckebusch, J. (2011). Comparison of a stepped-frequency continuous wave and a pulsed gpr system. *Archaeological Prospection*, 18(1):15–25.

Li, M. and Zhao, Y. (2014). Chapter 5 - seismic attribute analysis. In *Geophysical Exploration Technology*, pages 103–131. Elsevier, Oxford.

Manataki, M., Vafidis, A., and Sarris, A. (2021). Gpr data interpretation approaches in archaeological prospection. *Applied Sciences*, 11(16):7531.

Myhre, B. (2002). Landbruk, landskap og samfunn 4000 f. kr.-800 e. kr. *Jorda blir levevei*, 4000:11–213.

Neal, A. (2004). Ground-penetrating radar and its use in sedimentology: principles, problems and progress. *Earth-science reviews*, 66(3-4):261–330.

NGU (2023). Nasjonal løsmassedatabase. `https://geo.ngu.no/kart/losmasse_mobil/`. Accessed: 2023-08-30.

NIBIO (2023). Norsk institutt for bioøkonomi. https://kilden.nibio.no/?topic=jordsmonn&zoom=10.8&x=6962832.74&y=177348.24&bgLayer=graatone&layers=jm_dekning,jm_harm_klassifikasjon&layers_opacity=0.75,0.75&layers_visibility=true,true. Accessed: 2023-11-01.

Othman, A. A., Fathy, M., and Maher, A. (2016). Use of spectral decomposition technique for delineation of channels at solar gas discovery, offshore west nile delta, egypt. *Egyptian Journal of Petroleum*, 25(1):45–51.

Pigott, J. D., Kang, M.-H., and Han, H.-C. (2013). First order seismic attributes for clastic seismic facies interpretation: Examples from the east china sea. *Journal of Asian Earth Sciences*, 66:34–54.

Randen, T. and Sønneland, L. (2005). Atlas of 3d seismic attributes. In *Mathematical methods and modelling in hydrocarbon exploration and production*, pages 23–46. Springer.

Rial, F. I., Pereira, M., Lorenzo, H., Arias, P., and Novo, A. (2009). Resolution of gpr bowtie antennas: An experimental approach. *Journal of Applied geophysics*, 67(4):367–373.

Sala, J., Penne, H., and Eide, E. (2012). Time-frequency dependent filtering of step-frequency ground penetrating radar data. In *2012 14th International Conference on Ground Penetrating Radar (GPR)*, pages 430–435. IEEE.

Schneidhofer, P., Tonning, C., Cannell, R. J., Nau, E., Hinterleitner, A., Verhoeven, G. J., Gustavsen, L., Paasche, K., Neubauer, W., and Gansum, T. (2022). The influence of environmental factors on the quality of gpr data: The borre monitoring project. *Remote Sensing*, 14(14):3289.

Simm, R., Bacon, M., and Bacon, M. (2014). Seismic wavelets and resolution. *Seismic Amplitude: An Interpreter's Handbook. Cambridge University Press, Cambridge*, pages 23–37.

Stamnes, A. A. (2016). The application of geophysical methods in norwegian archaeology.

Trinks, I. and Hinterleitner, A. (2020). Beyond amplitudes: Multi-trace coherence analysis for ground-penetrating radar data imaging. *Remote Sensing*, 12(10):1583.

Trinks, I., Hinterleitner, A., Neubauer, W., Nau, E., Löcker, K., Wallner, M., Gabler, M., Filzwieser, R., Wilding, J., Schiel, H., et al. (2018). Large-area high-resolution ground-penetrating radar measurements for archaeological prospection. *Archaeological Prospection*, 25(3):171–195.

Trinks, I., Johansson, B., Gustafsson, J., Emilsson, J., Friborg, J., Gustafsson, C., Nissen, J., and Hinterleitner, A. (2010). Efficient, large-scale archaeological prospection using a true three-dimensional ground-penetrating radar array system. *Archaeological Prospection*, 17(3):175–186.

Våland, P. (2014). Penetration with step frequency ground penetrating radar.

Wang, Y., Eichkitz, C. G., Schreilechner, M. G., Heinemann, G., Davis, J. C., and Gharsalla, M. (2016). Seismic attributes for description of reef growth and channel system evolution—case study of intisar e, libya. *Interpretation*, 4(1):SB1–SB11.

Weinstein, L. (1988). Electromagnetic waves. *Radio i svyaz', Moscow*.

Widess, M. (1973). How thin is a thin bed? *Geophysics*, 38(6):1176–1180.

Yue, D., Li, W., Wang, W., Hu, G., Shen, B., Wang, W., Zhang, M., and Hu, J. (2019). Analyzing the architecture of point bar of meandering fluvial river using ground penetration radar: A case study from hulun lake depression, china. *Interpretation*, 7(2):T437–T454.

Zhao, T. (2018). Seismic facies classification using different deep convolutional neural networks. In *SEG International Exposition and Annual Meeting*, pages SEG–2018. SEG.

Zhao, W., Forte, E., Levi, S. T., Pipan, M., and Tian, G. (2015). Improved high-resolution gpr imaging and characterization of prehistoric archaeological features by means of attribute analysis. *Journal of Archaeological Science*, 54:77–85.

Zhao, W., Forte, E., and Pipan, M. (2016). Texture attribute analysis of gpr data for archaeological prospection. *Pure and Applied Geophysics*, 173:2737–2751.

Zhao, W., Forte, E., Pipan, M., and Tian, G. (2013). Ground penetrating radar (gpr) attribute analysis for archaeological prospection. *Journal of Applied Geophysics*, 97:107–117.

Appendices

Appendix A

A.1 Seismic attributes of the whole survey area

The provided link directs to a PowerPoint presentation showcasing the attributes generated in this study, encompassing the entire survey area of Løykja. This presentation enables the viewer to navigate through various time slices of the variance and RMS amplitude attributes, facilitating easier visualization.

`https://figshare.com/s/470f503fbace5051061b`

Appendix B

B.1 Burial mounds

Figure B.1 illustrates the impact of seismic attributes on the three burial mounds interpreted from the Løykja dataset, demonstrating how each attribute characterizes the burial mounds differently.

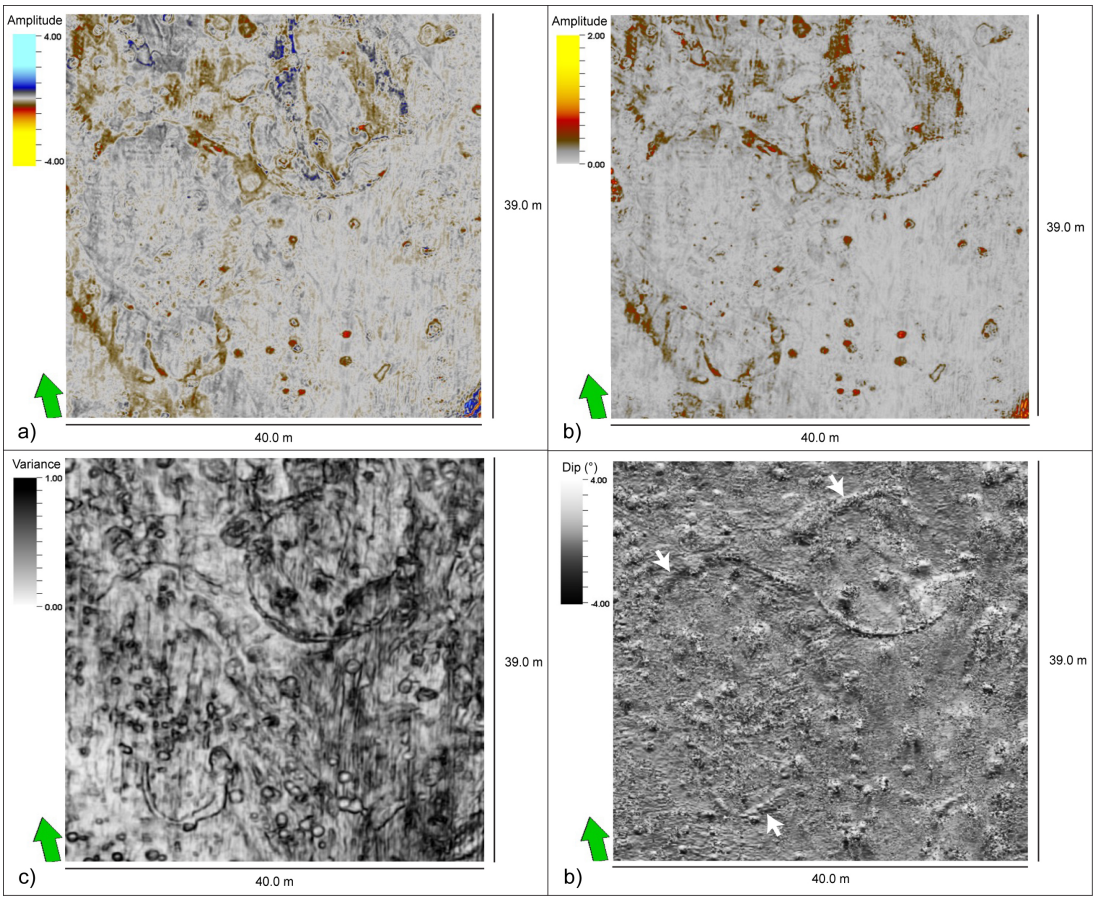

Figure B.1: *Time slice at twt = -12 ns of the burial mounds. a) Original data, b) RMS amplitude, c) variance, and d) dip illumination with* $\theta = 90°$ *where the white arrows point at the three mounds.*

Appendix C

C.1 Interpretation

The following figures display the interpreted horizon on an inline and xline section. The inline section presents the original data (Figure C.1), while the xline section showcases the structural smoothed cube (Figure C.2).

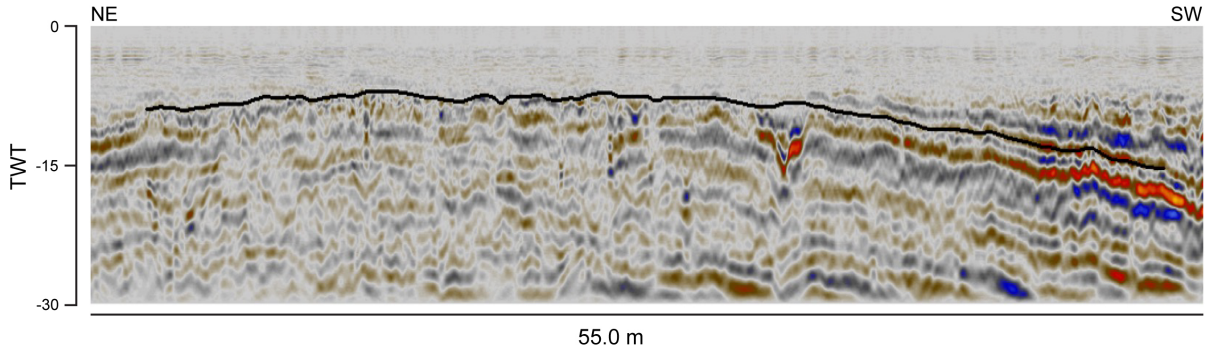

Figure C.1: *Interpretation of horizon on original data - inline*

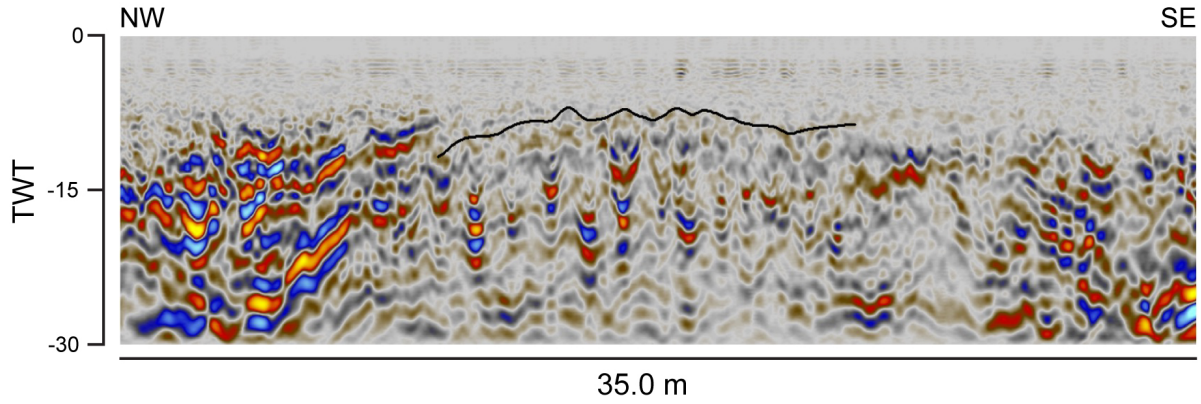

Figure C.2: *Interpretation of horizon on structural smooth cube - xline*

Appendix D

D.1 Taxonomy chart

This taxonomy chart illustrate useful attributes for different geological setting.

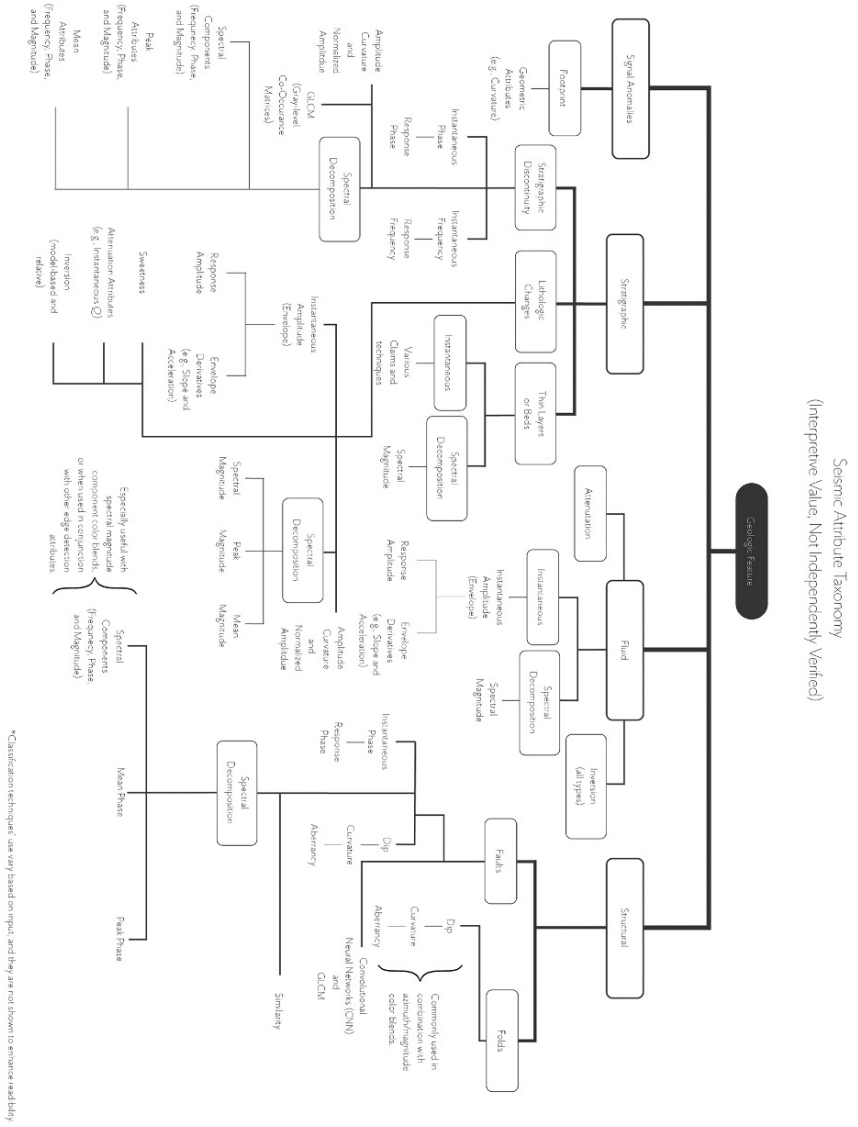

Figure D.1: *Seismic taxonomy chart for the interpretive value illustrating seismic attributes used for different geological features. Modified from (Dewett et al., 2021)*